Meandering rivers: interpreting dynamics from planform geometry and the secret lives of migrating meanders

A DISSERTATION
SUBMITTED TO THE FACULTY OF THE GRADUATE SCHOOL
OF THE UNIVERSITY OF MINNESOTA
BY

Jonathan Schwenk

IN PARTIAL FULFILLMENT OF THE REQUIREMENTS
FOR THE DEGREE OF
Doctor of Philosophy

Efi Foufoula-Georgiou, Adviser

August, 2016

Acknowledgements

I am extremely grateful to have worked under the guidance of Efi Foufoula-Georgiou, who allowed me the freedom to pursue research that interested me. Her generosity and support were second only to her relentless pursuit for excellent research, which I hope is adequately reflected in this thesis.

This dissertation may have never been completed without the unending assistance provided by the Saint Anthony Falls Laboratory (SAFL) IT staff, who saved me months of computing time by providing access to in-house supercomputing resources and other technical support. Special thanks to Charles "Chucky" Nguyen in particular for often going out of his way to ensure I had abundant resources. I am also indebted to a number of undergraduates and graduate students who assisted with acquiring, processing, and interpreting Landsat data. Mulu Fratkin, Ankush Khandelwal, Eric McCaleb, Anuj Kapartne, and Mace Blank were vital in the development of the Landsat "pipeline" that ultimately allowed me to distill insights from massive amounts of Landsat imagery.

I am grateful to my committee members, Stefano Lanzoni, Chris Paola, and Vaugh Voller for providing constructive and critical feedback and helping shape the course of my work. Although we have yet to meet in person, I am especially thankful to Stefano for his detailed (Skype) involvment in my first paper.

The National Science Foundation provided most of the funding for the work in this dissertation through a Water, Sustainability, and Climate grant, a Linked Institutions for Future Earth grant, and a Graduate Research Fellowship, and I am thus indebted to the citizens of the United States of America for their commitment to pursuing scientific inquiry in a complex world.

Finally, I have met too many wonderful people and researchers at SAFL to list them

all here, but I must express my deepest gratitude to all of those who shared their lives and experiences with me and ultimately led to my own intellectual, social, emotional, and philosophical growth. Finally finally, thanks to my parents and my Minnesota parents.

Abstract

Meandering rivers are dynamic agents of geomorphic change that rework landscapes through migration while maintaining beautiful looping planforms. This work investigates the relationships between the alluring planform geometries of meandering rivers, the dynamics of individual meander bend migration, and the dynamic processes driving meander evolution. A simple yet physically-based model of long-time meander migration is employed to understand the dynamic trajectories of individual meander bends and establish relationships between historic dynamics and cutoff bend geometry. At the reach scale, concepts from nonlinear dynamic theory are applied to river centerlines to determine if the dynamic nonlinearities driving meander evolution are preserved in the reachwide planform structure. Understanding how rivers move across their floodplains requires snapshots of planforms over long time periods from aerial photography or historic maps and surveys which are often taken at irregular and long intervals. Migration occurring between snapshots has thus largely remained a mystery. More recently, worldwide satellite imagery collected at least every 18 days by the NASA Landsat family of satellites offers the potential to reveal the secret lives of migrating, meandering rivers. This research mines the vault of Landsat imagery to resolve over 30 years of planform migration along more than 1,300 km of one of the Earth's most active meandering rivers: the Ucayali River in Peru. Analysis of the resulting annual binary channel masks suggests that migration rates are controlled by processes acting across bend-to-reach scales. An exciting new geomorphic discovery emerges from the analysis revealing the role of cutoffs as drivers of nonlocal morphodynamic change.

Contents

List of Tables

List of Figures

Chapter 1

Introduction

Meandering rivers have intrigued researchers for decades with their beautiful aesthetics, complex dynamics, and extraordinary cutoffs. The first physically based theory answering the question of why rivers meander was not introduced until the early 1980s [2] despite decades of study on the problem (see [3] for a thorough review). Meandering channels seem to be somewhat universal; besides the ubiquitous terrestrial meandering rivers, they are also found in submarine [4, 5] and other planetary [6, 7, 8, 9] environments. Understanding meandering river dynamics is important for a host of engineering and geologic applications including stream restoration [10], bridge design [11], agriculture management [12], stratigraphic interpretation [13], oil discovery [14, 15], border disputes [16], and even predator-prey population dynamics [17].

1.1 Process from Form

Migrating meandering rivers are particularly intriguing because they exhibit strikingly similar planform shapes despite the multitude of processes known to drive their evolution. Even meandering rivers flowing through extremely disparate environments often resemble each other, suggesting that their sinuous planforms may be the result of some formative process(es) that prevails for a wide range of hydraulic, hydrologic, or sedimentary conditions. This mystery has driven decades of research focused on understanding which physical mechanisms interact to create, sustain, and evolve the meandering form, and serves as the

broader inspiration behind this research. The geomorphologic concept of 'process from form' was central to the investigations described in Chapters 2 and 3.

In particular, Chapter 2 asks the question 'How much dynamic information is preserved in the shape of meander bends?' using a simplified, physically-based numerical model of long-time meander evolution. The model accounts for only the most basic hydrodynamic processes required to sustain meander migration including cutoffs. The meander bends simulated by the model represent only the simplest autogenic processes inherent in any migrating meandering river. An algorithm is developed to track individual meander bends, and a suite of geometric variables describing cut off meander bends is tested for their ability to predict bend dynamics. Finally, the dynamics and geometries of individual bends are linked and show that, at a fundamental level and in the absence of natural heterogeneities, unsteadinesses, and perturbations, the shapes of meander bends do indeed encode their formative dynamics.

The focus in Chapter 3 shifts from individual bends to entire meander trains. This work was inspired by the incompatibility of two previous bodies of research: the in-channel hydro- and sediment dynamics that govern meander planform evolution are known to be nonlinear, and in fact the basic equation governing the evolution of a curve (i.e. river centerline) contains an inherent geometric nonlinearity. Despite these known nonlinear dynamics, attempts to quantify nonlinearity from static (not dynamic) meander planform structure have been unsuccessful. In other words, the meandering river form did not apparently reflect a known feature (nonlinearity) of its underlying dynamics, suggesting a limit to the degree which process may be interpreted from form. These conflicting findings demanded a resolution that is addressed in Chapter 3 through the use of a robust metric of nonlinearity combined with nonlocal frequency (wavelet) analysis to identify which features of the meander planform best represent the nonlinearity of the underlying dynamics. The investigation includes the simulated river from Chapter 2, which provides a sterile environment for understanding how the nonlinearity metric responds to planform evolution, and cutoffs in particular. The planform structure of three natural rivers (two in Minnesota and one in Peru) are also examined and show that, counter to previous studies, driving nonlinear dynamics are indeed reflected in reachwide geometry.

1.2 The Secret Lives of Migrating Rivers

The lives of migrating rivers have largely been enshrouded in secrecy due to the difficulty in acquiring high-frequency observations of channel positions over long times and across large spatial domains. A concerted effort in the 1960s emerged from within the geomorphology community to map and measure meander planform changes [18] and relate migration rates to local channel properties [19, 20]. Similar work had been performed by [21] and others mapping the historical planform changes along the Mississippi River. Historically, initial, final, and a few intermediate channel positions could be obtained from historic maps, occasional aerial photography, or dating techniques using scroll bars, tree rings, etc. Despite these studies' significant contributions toward deciphering meandering river dynamics, the difficulty of acquiring long-time, high temporal and spatial resolution channel migration data has hampered efforts to fully quantify dynamics from observations alone [22, 23]. Migration rates were obtained from these realizations of river planforms, but a lingering question remained: what was the river doing in-between these snapshots? Did migration occur gradually and incrementally, or did rivers move discretely in large bursts during, for example, flood events? Which processes and over what scales were driving river migration?

Worldwide satellite imagery collected by the Landsat family of satellites provided for the first time aerial views of large rivers at 30 meter spatial resolution and at least every 18 days. While many of the views of Earth are obscured by clouds, the frequent snapshots from the Landsat database reveal the entire dynamic lives of many of the planet's most active rivers. Chapter 4 describes an effort to leverage Landsat data for mapping and quantifying river migration over large spatial domains (over 1,300 km of river are mapped) and with adequate precision to quantify local-scale dynamics (i.e. point-bar scale) with annual frequency. A method for classifying and compositing annual channel mask images from Landsat data was developed, and the analysis of these channel masks required a new set of tools capable of handling an extraordinarily dynamic river undergoing many modes of migration and over 50 cutoffs in 30 years. Chapter 4 describes this toolbox, called RivMAP: River Morphodynamics from Analysis of Planforms, and presents results from its application to the Ucayali River in Peru. The results highlight the necessity of high-frequency analysis in order to identify the multiple scales of controlling processes on river migration.

The annual analyses of Ucayali planform evolution revealed a previously-undocumented geomorphic insight: cutoffs effect nonlocal morphodynamic change. Chapter 5 describes this new discovery and presents evidence of cutoffs as perturbations that accelerate migration and induce channel widening as far as 115 channel widths downstream (approximately 8 bends away) and 30 channel widths upstream. Results suggest cutoffs may play an underestimated role in channel and floodplain evolution and provide a new perspective on channel stability.

Chapter 2

The life of a meander bend: connecting shape and dynamics via numerical modeling

Analysis of bend scale meandering river dynamics is a problem of theoretical and practical interest. This work introduces a method for extracting and analyzing the history of individual meander bends from inception until cutoff (called "atoms") by tracking backwards through time the set of two cutoff nodes in numerical meander migration models. Application of this method to a simplified yet physically-based model provides access to previously unavailable bend-scale meander dynamics over long times and at high temporal resolutions. We find that before cutoffs, the intrinsic model dynamics invariably simulate a prototypical cutoff atom shape we dub *simple*. Once perturbations from cutoffs occur, two other archetypal cutoff planform shapes emerge called *long* and *round* that are distinguished by a stretching along their long and perpendicular axes, respectively. Three measures of meander migration—growth rate, average migration rate, and centroid migration rate—are introduced to capture the dynamic lives of individual bends and reveal that similar cutoff atom geometries share similar dynamic histories. Specifically, through the lens of the three shape types, *simples* are seen to have the highest growth and average migration rates, followed by *rounds* and finally *longs*. Using the maximum average migration rate as a metric describing an atom's dynamic past, we show a strong connection between it and

two metrics of cutoff geometry. This result suggests both that early formative dynamics may be inferred from static cutoff planforms and that there exists a critical period early in a meander bend's life when its dynamic trajectory is most sensitive to cutoff perturbations. An example of how these results could be applied to Mississippi River oxbow lakes with unknown historic dynamics is shown. The results characterize the underlying model and provide a framework for comparisons against more complex models and observed dynamics.

2.1 Introduction

A concerted effort emerged in the 1960s from within the geomorphology community to measure meander planform changes [18] and to explain mechanisms driving observed planform evolution [19]. This work rested upon previous research that developed metrics of planform geometry through analysis of both real [24, 25, 26] and experimental [27, 28] meanders. Since then, significant contributions have been made via an abundance of field studies that apply these metrics to real river centerlines derived from combinations of historic maps [29], aerial photography [30, 31], and field surveys [32].

Despite these studies' significant contributions toward deciphering meandering river dynamics, the difficulty of acquiring long-time, high temporal and spatial resolution channel migration data has hampered efforts to fully quantify dynamics from observations alone [22, 23]. Numerical modeling has thus become a primary tool for understanding meandering complexity and emergent behavior. Long-term meander models simulate migrating channels over centuries to millennia, providing insight into otherwise inaccessible dynamics. These models are useful for both practical (e.g. [33, 34]) and theoretical investigations. Theoretical analyses of such simulations typically focus on either reach-scale measures such as sinuosity [35, 36], mean meander wavelength [37], or mean curvature [38]. However, to the best of our knowledge no study has considered either observed or modeled well-resolved temporal dynamics of individual meander bend evolutions. Here we present a new tool for identifying and extracting the lives of these individual meander bends, dubbed "atoms" and defined extensively in Section 2.3, from the centerline output of long-time channel migration models. Our method makes accessible the lifespan of individual meander bends from inception until cutoff by tracking the two end indices of a set of cutoff nodes backwards through time.

Our choice to focus primarily on bend scale morphodynamics is guided by its emergence as perhaps the only natural intermediate scale between the cross-section and river-valley scales. Meandering river relicts are frequently preserved at bend scales through the formation of oxbow lakes or scroll bars. Engineering designs are often concerned only with morphodynamics of a single bend (e.g. [39, 40]). Besides the pragmatism of the bend scale, physically-based meander migration theories [2, 41] predict a nonlocal memory effect on local hydrodynamics from nearby curvatures that becomes approximately negligible beyond a single meander wavelength. In addition to being a natural scale for analysis of meandering rivers, the bend scale approach promises at least three advantages toward understanding river meandering dynamics.

First, a bend-scale framework may help reinterpret previous work on meander loop classification by linking static planform shapes to historic dynamic signatures. Classification schemes for oxbow lakes [6] and river meanders [42, 43] are well-developed, but as [44] points out, the goal of such classifications is to connect form and process. Although modes of planform migration have been well-established [45, 46], linking these modes to underlying physical processes has largely remained an open research area: which dynamic behaviors are correlated with which planform shapes? Conversely, inferring dynamics from static planform shapes can be useful for paleochannel studies [47].

Second, meander bends provide a more refined basis to compare model outputs to both real rivers and other models by avoiding reachwide-averaged metrics. [37] found three contemporary models of increasing complexity to be statistically indistinguishable in their spatially-averaged meander wavelengths and curvatures. The dynamic details resulting from the different physics and assumptions of each model are smoothed over by such reachwide averaging. Bend-scale measures that dissect reachwide ones are better suited for describing and explaining differences in model outputs because they provide full distributions rather than sole averages. The problem of statistical averaging in meandering river studies has been known for awhile [45] but remains largely unaddressed because tools have not yet been developed. Meander loops are already inherently difficult to classify with single measures [48], so averaging over already-averaged quantities results in substantial information loss. An attempt to overcome these difficulties was put forward by [38] who proposed a suite of 40 morphometric variables to distinguish between modeled and natural

planforms. However, their work focused only on spatial analyses of these variables rather than their dynamics. By combining spatial and temporal analyses, our method can both effectively diagnose a model's dynamic accuracy and elucidate how accounting for different physical processes affects channel migration dynamics.

Third, a recent Special Issue on meandering [49] highlights the apparent gap between holistic and reductionist philosophies of river meandering. In the format of an entertaining philosophical dialogue, [50] discuss the incongruities of holistic analyses performed using reductionist-based migration models. For example, researchers have tested meandering rivers for nonlinear dynamics [51, 52], chaotic dynamics [53], self-similarity [19, 54], self-organized criticality[55], and fractality [56, 57], all concepts that imply the presence of energy at many space-time scales. Accessible bend-scale dynamics will help link local physical processes with reach-scale phenomena by providing a coherent intermediate scale between global and local.

The focus of this paper is primarily on the first of these three issues, i.e. connecting simulated meander geometries with their formative dynamics, but we hope the utility of our study toward refined model comparisons and bridging scales of analysis becomes clear from the work herein. This paper is structured as follows: Section 2.2 describes the numerical migration model we used, Section 2.3 explains how individual bends are extracted through time, Section 2.4 presents some results and insights of the analysis followed by discussion in Section 2.5. Section 2.6 concludes with general remarks and future work.

2.2 Model description

Long-time meander migration models usually have four distinct components: (1) a morphodynamic model relating the flow field to bank migration, (2) a hydrodynamic model relating the channel geometry (i.e. curvature and cross-sectional geometry) to the flow field, (3) an evolution equation relating bank migration to planform geometry, and (4) a model accounting for cutoff events (e.g. [36]). The third and fourth components render numerical models necessary to account for the strong nonlinearities associated with the kinematics of channel planform evolution and abrupt channel shortening due to cutoff processes [58]. By adopting simple first and second components (i.e. morpho- and hydrodynamic models) here, our resulting dynamics provide insight into the geometric nonlinear interactions that

are present in all models of long-time channel migration.

2.2.1 Morphodynamic and hydrodynamic model

Several models are currently available to treat bank erosion [59, 60, 61] and to describe the flow field in meandering channels with arbitrary distribution of the channel axis curvature [2, 41, 62] and channel width [63, 64]. In the following, however, we prefer to keep the hydrodynamic and morphodynamic models at the lowest level of refinement. In fact, our aim is to develop a new methodology for characterizing individual bend dynamics that can be used independently of the degree of approximation and physical realism embodied by the adopted morphodynamic and hydrodynamic models. We thus follow the work of [59] and [2] who first introduced a dynamic approach for bank erosion and a linearized flow field model in sinuous channels, providing a relatively simple framework for computational modeling (hereafter called HIPS after its authors). A suite of models has emerged following their pioneering work that share the following morphoydynamic model:

$$\zeta = E_o U_b \tag{2.1}$$

in which the lateral migration rate, ζ, at a point along a channel centerline is the product of a bank erodibility coefficient E_o and an excess bank velocity U_b resulting from perturbations in channel curvature and bar formation. This linear relationship for migration has been validated by the field campaigns of [59], [65], and [66]. The erodibility coefficient E_o is generally considered representative of the geotechnical bank properties [67] whose functional dependencies remain unknown but include near-bank vegetation, failure mechanism, and local channel geometry effects among others [68]. In predictive models E_o is typically calibrated using past channel configurations (e.g. [69, 70, 71]), although studies have also investigated its effects on migration dynamics [72, 68, 73, 74].

The hydrodynamic model for U_b is developed by casting the St. Venant shallow water equations in an intrinsic coordinate system, where the $s = S/B$ coordinate refers to the dimensionless streamwise direction, $n = N/B$ coordinate to the transverse direction, and B is the channel half-width (Figure 2.1). Lowercase variables are dimensionless and variables subscripted with $_o$ denote channel-averaged values. Scaling the channel axis curvature as $c = CR_o$, where R_o is the minimum value of the radius of curvature within the investigated

reach, reveals the existence of the usually small parameter $\nu_o = B/R_o$. The relevant variables can then be expanded in terms of ν_o, and a linear perturbation analysis gives the following linear solution for excess flow velocity at the bank under assumptions of constant channel width and spatially constant friction factor:

$$u_b(s) = [u_b(s=0) + \nu_o c(s=0)]\, e^{\lambda_o s} - \nu_o \left[c(s) + \frac{\lambda_o}{2}(F_o^2 + A) \int_0^s c(\xi) e^{\lambda_o (s-\xi)} d\xi \right] \quad (2.2)$$

where the dimensionless excess bank velocity $u_b = U_b/U_o$ and channel axis curvature $c = CR_o$ are $\mathcal{O}(1)$ quantities, $\lambda_o = -2\beta C_{fo}$ is a characteristic exponent where $\beta = B/D_o$, C_{fo} is the spatially-constant friction factor, $F_o^2 = U_o^2/gD_o$, and A is a constant slope factor expressed as $\alpha + 1$ after [75] where α is a dimensionless parameter related to the across-stream bed slope. Our simulation parameters, based on bankfull flow conditions of the Beatton River in Canada originally reported by [76], are as follows: $B = 35$ m, Q_o =325.6 cms, $C_{f,o}$ =0.0036, E_o =1.85x10^{-8}, α =10, and s_v =0.0067. The upstream boundary condition on u_b was set to zero, prohibiting migration of the first node, and boundary conditions on curvature are discussed in Section 2.2.2. The convolution integral in Equation (2.2) implies that the excess bank velocity at a given section is affected not only by the local value of the axis curvature but also by the hydro- and morphodynamics of the upstream reaches. In particular, influence is exerted only in the downstream direction. This is a direct consequence of the decoupled treatment of sediment-flow dynamics (i.e. prescribed transverse bed slope) that precludes the model's accounting for overdeepening [77], resonance [78], and upstream influence [79]. The hydrodynamic model does not explicitly account for secondary flow momentum convection and instead uses the surrogate parameter A [80].

We should note that many of the assumptions and simplifications of the work of [2] have since been relaxed, including small-curvature restrictions [81], constant width [82, 63, 64], prescribed width [64], constant discharge [83, 84], deformable bed [80, 41], two-dimensionality [85], linearity [62], and single-threadedness [86]. [87] reviews two decades' progress in meander migration modeling, while [60] offers a recent critical assessment of the HIPS formulation. Despite their significant simplifications, HIPS models can produce reach-scale planforms and dynamics that under sub-resonant conditions are statistically similar to real planforms with regards to fractal dimension of river lengths [55],

size-frequency distributions of oxbow lakes [54], and planimetric form [36]. Additionally, [37] compared a HIPS model with two more sophisticated models [80, 41] and found that the average river wavelength and curvature approached a statistically steady state independent of model complexity. Under sub-resonant conditions the HIPS model we employ here sufficiently captures the first-order, curvature-forced processes driving river meandering over long times and hence is suitable for developing new tools that characterize the individual bend dynamics.

2.2.2 Numerical environment

The basic steps of our meander migration model proceed as follows: 1) input a centerline and reachwide hydraulic variables, 2) solve hydrodynamics throughout the reach, 3) migrate the channel, 4) check node spacing criteria, 5) locate and perform cutoffs, and 6) update reach-averaged variables. The model was implemented in MATLAB and takes advantage of parallel processing for solving the hydrodynamics and locating and performing cutoffs. Source code for the model and extraction algorithm is provided as a Supplementary file.

Gridding and numerical migration

Our numerical model uses both Cartesian and intrinsic coordinates, as shown in Figure 2.1. The channel centerline is first discretized into a series of initially evenly-spaced nodes every $B/2$. Constant channel width and prescribed bed topography permit reconstruction of the channel geometry from its centerline so no other planform variables are saved. Following [72], the initial planform configuration is a straight line parallel to the valley axis with small random Gaussian perturbations $\sim \mathcal{N}(0, 0.01B)$ in the streamwise-perpendicular direction. At every time step, each centerline node migrates according to Equation (2.1) and

$$\frac{dX_i}{dt} = -\zeta_i \sin\theta_i \tag{2.3}$$

$$\frac{dY_i}{dt} = \zeta_i \cos\theta_i \tag{2.4}$$

for node i, where θ_i is the i^{th} angle between the downstream channel direction and the x-axis. As the nodes of the channel centerline migrate, spacing between nodes may become

either too large or too small. If the distance between nodes becomes too large, numerical accuracy suffers and the model tends toward instability. Conversely, very small node spacings can introduce errors associated with the computation of curvature. [88] suggests based on empirical analysis that optimal node spacing is on the order of $2B$; we adopted a maximum node spacing threshold value of $\frac{4}{3}B$. Where this threshold was exceeded, a parametric cubic spline [89, 90] fit to the preceding and following three points (six nodes total) determined the coordinates of the interpolated node. In rare cases, especially after cutoff, node spacing could become too small so a lower threshold of $\frac{B}{5}$ was maintained. The time step $\triangle t = 0.2$ years was chosen small enough to ensure numerical accuracy and stable computations [91, 72, 79].

Computation of curvature

The hydrodynamic model is primarily driven by variations in curvature along the centerline, yet methods of digital curvature estimation from discrete nodes are often inaccurate and biased [92]. Evidence suggests that long-time meander migration models are sensitive to small perturbations (see Figure 4 of [72]), so even small inaccuracies in curvature estimation could significantly alter the simulated planform. One of three mathematically equivalent definitions of curvature κ is usually employed in meander migration models, but their accuracies are dependent on both gridding and computation method. For a planar curve in Cartesian coordinates, $\kappa_1 = \frac{|x'y'' - y'x''|}{(x'^2 + y'^2)^{3/2}}$ where the prime denotes a derivative taken with respect to the S direction. If derivatives are approximated via a first-order differencing scheme, the denominator equals unity leading to the form in [75] (their Equation 28). A second widely-used method exploits the definition $\kappa_2 = d\theta/dS$, where first-order differencing gives $\theta_i = \arctan\left(\frac{y_{i+1} - y_i}{x_{i+1} - x_i}\right)$. The third method and one we employ considers $\kappa_3 = 1/R$, where the radius of curvature

$$R = \frac{\sqrt{(\mathbf{a_x^2} + \mathbf{a_y^2})(\mathbf{b_x^2} + \mathbf{b_y^2})(\mathbf{c_x^2} + \mathbf{c_y^2})}}{2\left(\mathbf{a_y b_x} - \mathbf{a_x b_y}\right)} \tag{2.5}$$

for $\mathbf{a_x} = x_i - x_{i-1}$, $\mathbf{b_x} = x_{i+1} - x_{i-1}$, $\mathbf{c_x} = x_{i+1} - x_i$. This formula for R arises from geometric considerations showing that the radius of a circle defined by three points is the area of their triangle divided by the product of the lengths of their sides; it provided the

stablest and smoothest curvature signal among the three methods (Figure 2.2), preventing the need for a smoothing filter as often required by numerical meander migration models [88]. Our selected method for curvature computation may not produce similar results in other numerical environments because the computation of curvature depends also on grid resolution and configuration, derivative estimation method, and computational precision.

An upstream boundary condition on curvature must be applied at each time step; we used a periodic boundary condition of $c(s = 0)_t = c(s = end - 1)_{t-1}$, where end refers to the final node along the centerline and $_t$ denotes the model's current time step. The downstream-most curvature value $c(s = end)$ requires a linearly-interpolated centerline node downstream of the reach at each time step; information only travels downstream in models that do not account for resonance [79], so errors introduced by this interpolation will not propagate upstream into the domain.

Cutoffs

Natural meandering rivers typically cut off via either chute or neck mechanisms [93]. Neck cutoffs occur when migrating river reaches intersect themselves, while chute cutoffs "short circuit" neck cutoffs with a connecting channel usually during flood flows. Chute cutoffs have been well-documented (e.g. [94, 95]), but the various mechanisms driving their occurrence remain relatively unexplored and therefore difficult to predict [3, 96]. [97] presents a meander migration model that takes a stochastic approach to chute cutoffs. Because of the poor predictability of chute cutoffs, our model accounts only for neck cutoffs.

Neck cutoffs are identified when two nodes of stream centerline are separated by a distance less than or equal to $2B$. This search begins at the upstream-most centerline node and works downstream, removing cutoffs along the way. The built-in MATLAB function *rangesearch* builds a kd-tree to reduce search time of closest nodes from $\mathcal{O}\left(m^2\right)$ time complexity to $\mathcal{O}\left(log(m)\right)$, where m is the number of centerline nodes. If intersections are detected, the portion of centerline between the intersecting segments is removed, a single node is added across the cutoff via cubic spline interpolation, and a local Savitztky-Golay filter [98] is applied to smooth the resulting discontinuity. [37] offer an algorithm for cutoff search that operates in apparently $\mathcal{O}(m)$ time.

2.3 Atom Tracking Method

In this work we seek to explore the dynamics of simulated individual meanders from their inception until cutoff, requiring a robust and accurate method for continuously identifying meander loops. A meander loop is typically defined as the reach of stream between two points of zero curvature known as inflection points. For a continuous function, curvature can be computed analytically as the second derivative and the inflection points easily obtained, but for discrete nodes inflection point detection becomes more complicated. In general, inflection points are not located exactly at grid nodes, so they must be somehow interpolated between two nodes of oppositely-signed curvature. The simplest identification method assigns the inflection point to the node with the smaller absolute curvature value. However, as discussed in Section 2.2.2, discrete curvature computations can cause complications connected with curvature calculation method which might lead to misidentifying the inflection node [92, 99]. Additionally, spurious flexes especially along nearly-straight sections of the curve will identify more than two inflection points per meander bend (e.g. Figure 9 of [100], rendering ambiguous meander endpoints. These flexes preclude robust algorithms from properly detecting inflection points smoothly through time and therefore require ad hoc rules. For example, [38] proposed identifying nodes as inflection points when

$$sign\left(C_i + C_{i-1}\right) \neq sign\left(C_{i+1} + C_{i+2}\right) \tag{2.6}$$

where C_i is the curvature of the node in question. Others such as [101] use minimum length and minimum curvature criteria.

For spatial analyses of meanders (e.g. [38, 37, 102]), simple meander loop detection methods based on inflection points are usually sufficient because small errors in the inflection point location only slightly affect average meander measures of wavelength, amplitude, or skewness. For estimating such properties dynamically (as they change through time), however, errors in detection can lead to substantial inaccuracies in the time series. Therefore dynamic investigations require a robust and continuous detection of meander endpoints for any given planform.

We found ad hoc methods to be unreliable when applied to the various evolving complex shapes produced by the model, so a new method was developed. With only a few modifications, this method can be applied to any model that tracks a set of centerline

nodes through time. Instead of defining meander bends as reaches of stream between inflection points, we take another approach and introduce *atoms*. An atom is simply a river reach that evolves in time and eventually intersects itself to become a cutoff meander loop (Figure 2.3).

Our method for identifying an atom continuously through time requires that its cutoff locations (or indices) be known *a priori*. The indices of the first and last nodes of the known cutoff may then be tracked by moving backwards through time, adjusting them as nodes were added or removed upstream. Figure 2.3b shows two atoms developing from apparent squiggles of centerline into full meander loops. A single-loop atom usually has an upstream and downstream tail defined as the length of stream between the cutoff node and the inflection node (see Figure 2.9 and discussion in Section 2.4.2), while its head corresponds to the traditional definition of a meander bend as the length of stream between inflection points containing the apex of the loop. We should note that although the definition of an atom does not preclude its application to real rivers, the condition that the cutoff location be known beforehand limits its applicability. In the following section we present an unambiguous method for identifying atoms from simulated meander migration models.

2.3.1 Numerical Implementation

An atom's endpoints are tracked backwards through time with a node accounting algorithm beginning with the positions of the first and last indices of a set of cutoff nodes, or the two *cutoff indices*. This algorithm, while conceptually simple, can be tricky to implement. It requires that the model saves at each time step i) the channel centerline and ii) the time and locations of any added or removed nodes including the time and locations of cutoffs. The algorithm then marches backwards in time, adjusting the two cutoff indices to account for nodes inserted due to spacing threshold requirements and/or removed due to cutoffs, smoothing or grid spacing.

The heart of the meander bend tracking algorithm is an accounting scheme which simply adds or subtracts to the original cutoff indices in the reverse order that nodes were added or removed, respectively. For example, a typical meander migration model implementation might progress as follows: input centerline nodes $\rightarrow$ migrate centerline nodes $\rightarrow$ remove cut off nodes $\rightarrow$ insert or remove nodes to maintain grid spacing $\rightarrow$ advance time step.

The corresponding algorithm to track atoms would then be: input cutoff indices → adjust cutoff indices for spacing insertions/removals → adjust cutoff indices for cutoffs removed upstream → "advance" to previous time step. The specifics of the accounting algorithm are dependent on the model implementation; for example, some models may smooth the centerline near a cutoff and if this process adds or removes nodes, the accounting scheme must consider it.

As the algorithm tracks cutoff nodes backward through time, the atom being tracked shrinks. At some point the tracked atom reaches a minimum length associated with its inception or birth, and at this point the algorithm should halt. If the algorithm instead continues tracking, the tracked cutoff nodes become meaningless as they represent a section of another atom whose cutoff gave birth to the originally-tracked atom. Therefore a threshold on the atom's change in length serves as a robust method to identify time of inception: i.e. abort tracking when $L_a(j) - L_a(j-1) > L_{thresh}$, where j refers to the j^{th} iteration of the tracking algorithm for a particular atom. We recommend $L_{thresh} = 10B$ based on the modeling scheme herein, but this threshold depends on the strategy implemented to enforce sufficient node spacing.

2.3.2 Limitation of the Methodology

The atom extraction scheme cannot be applied to a model which periodically regrids the centerline. Generally, node spacing can be maintained by either globally regridding the full centerline or adding or removing nodes locally. Both methods require an interpolation scheme, usually parametric cubic splines [89, 103], which invariably introduces errors into the channel centerline [88]. The atom tracking algorithm presented here cannot be used in conjunction with global regridding because regridding erases the individual node history exploited by the algorithm. While most meander migration models do regrid the channel centerline periodically (e.g. [104, 105, 106]), it is not required generally. ([37] do take advantage of equal node spacing for coordinate transformation and cutoff detection.) While some smoothing is usually required for stability, local interpolation introduces fewer errors into the centerline configuration compared with complete regridding. Moreover, regridding essentially low-pass filters the channel centerline at a frequency determined by

the interpolation scheme, removing the smallest-scale bends [88]. Modelers have successfully employed local interpolation schemes ([72, 107], model herein), avoiding the need for computationally expensive regridding schemes while maintaining spacing requirements and numerical stability.

However, even local regridding poses a problem for the algorithm: as a bend grows and nodes are added, sometimes the interpolated node becomes the cutoff node being tracked. In other words, an atom's cutoff node(s) may not have existed at the atom's inception but were interpolated during its growth. In this case, when tracking an atom's two cutoff nodes backwards through time, this node disappears at the time step it was originally introduced (Figure 2.4). Rather than halt the algorithm, the node nearest the one removed becomes the cutoff node at the next time step. The frequency of such instances depends on the average node migration rates (which depend on model parameters) and the spacing thresholds, but for the simulation herein this occurred approximately once per atom lifetime.

2.4 Results

The simulation of a slightly perturbed, initially-straight 40 km river reach for 30,000 years (Figure 2.5a) resulted in 992 cutoffs corresponding to one cutoff approximately every 30 years. Of these 992 atoms, only those occurring a downstream distance greater than 20% of the entire reach length were considered further, ensuring that atom dynamics are unaffected by the upstream periodic boundary condition on curvature (see Section 2.2.2). Our model allows only downstream propagation of perturbations so the threshold was not applied to the downstream portion of the reach. The mean tortuosity, or ratio of river length to the distance between its ends, approached a steady average value of 4.46 after 3,000 years, and atoms occurring before this time were not included in the analyses. Of the remaining atoms, only those with lifespans longer than 400 years were considered to ensure sufficiently long time series, leaving a total of 672 atoms. The following results draw only from these 672 atoms unless otherwise noted.

This section contains three parts that describe the lifetime of an atom. In Section 2.4.1, atom cutoff geometries are classified and geometric relationships established; three archetypal emergent cutoff shapes are identified and compared. In Section 2.4.2, atoms' dynamic histories are described using three measures of bend-scale meander dynamics. Finally in

Section 2.4.3, the results from the preceding two sections are combined to demonstrate that cutoff geometry contains the signature of historic formative dynamics.

2.4.1 Atom Cutoff Geometries

Atom cutoff geometries emerging from the simulation spanned a variety of planform shapes and sizes including double- and triple-compound loops and a diversity of single-lobed bends. Despite this diversity, some recurring archetypal cutoff atom shapes were identified through basic curvature and shape metrics. In general, the inability of HIPS models to reproduce the resonance phenomenon and hence failure to describe super-resonant conditions produces single lobed bends that are invariably upstream-skewed and downstream-migrating [79].

Following [108], we first separated *singles* from *multilobes* requiring that a *single* have a maximum of two inflection points and only one maximum curvature corresponding to the apex of the bend (e.g., Figure 2.3b, left). By this criterion 82% of all atoms were *singles*. *Multilobe* atoms (e.g. Figure 2.3b) showed substantial variability in their planform geometries that precluded analysis using the metrics developed here. The hydrodynamic model we employ contains no inherent dynamic mechanisms capable of forming a multi-lobed atom in the absence cutoff perturbations, contrary to models like that of [36] for example, which simulates single lobes that grow additional bends before cutoff (their Figure 7a). We therefore consider *multilobes* produced by the HIPS model as aggregations of individual *singles*, and subsequently focus our attention solely on *singles*.

Amongst the diversity of *single* planform configurations, three archetypal shapes emerged from the simulation dubbed here as *simple*, *round*, and *long* (Figure 2.6a). We note that these shape designations are presented as a conceptual model to help relate different geometries to distinct dynamic behavior and not intended as a broader classification scheme. *Simple* cutoff atoms have a teardrop shape reminiscent of the classic Kinoshita [109] loop. *Simples* are prototypical in the sense that in the absence of large perturbations (i.e. an initially straight planform with only small perturbations in curvature), they are the only shape that forms. Indeed, each of the first 30 cutoffs of the simulation fell into the *simple* category. The spectrum of *simples* ranges from a fatter planform shape (*round*), to an elongated version (*long*), both of which may be considered stretched *simples*. *Longs* are stretched parallel to the long axis of the meander loop, while *rounds* are stretched in the

perpendicular direction.

The previously qualitatively-described classifications may also be distinguished quantitatively by considering the ratio of the absolute curvature at the apex of an atom to the average absolute curvature along the cutoff atom $c_r = |C|_{max}/|C|_{avg}$ (Figure 2.6d). This dimensionless ratio, which is unity for a circle, clusters similarly-shaped cutoff atoms together such that those atoms with values near the mean tend toward the *simple* shape, while atoms with values closer to one have *round* geometry (Figure 2.6d). For larger values of the ratio, cutoff atoms become more elongated giving rise to the *long* group. To illustrate the links between geometric and dynamic relationships, we selected 25 cutoff atoms with the lowest (highest) c_r values to represent *rounds* (*longs*), and chose 25 cutoff atoms nearest the mean c_r value to represent *simples*. As Figure 2.6b shows, both the maximum and average curvature values are necessary to distinguish between the three groups; the $|C|_{max}$ value for the *round* cutoff atom is very near the *long* cutoff atom, but their $|C|_{avg}$ are dissimilar. For the *round* and *simple* cutoff atoms, the situation is reversed and the $|C|_{avg}$ values are close but the $|C|_{max}$ values differentiate the two.

Regardless of their stage of development at cutoff and despite the various centerline configurations, simulated *single* cutoff atoms' apex curvatures scale linearly with their average curvatures depending on shape (Figure 2.7). The cutoff atom groupings in Figure 2.7 reflect the use of c_r as a metric; each group maintains approximately the same ratio and therefore falls within a narrow band. *Rounds* exhibit significantly more geometric variability than other types. For example, for a given $|C|_{avg}$ the range of observed $|C|_{max}$ is greater for *rounds* than *longs*. A cutoff atom's area scales with the square of its perimeter as with non fractal 2-D polygons.

2.4.2 Atom Dynamics

The complex behavior of meandering river migration has given rise to a host of metrics designed to capture the many possible planform migration modes of a meander bend (e.g. [108, 11]). Here we take advantage of the atom extraction algorithm which delineates a meander loop through time along with known simulated migration at every point and time and investigate atom evolution via three migration measures: average migration rate (φ_{avg}), centroid migration rate (φ_{cen}), and atom growth rate ($\frac{dL_a}{dt}$).

Dynamic Measures

A single node's instantaneous migration rate is computed as the Euclidian distance between the node's location after some elapsed time divided by the elapsed time:

$$\varphi_i(t) = \frac{1}{\triangle t} \left\| \begin{array}{c} X_i(t+\triangle t) - X_i(t) \\ Y_i(t+\triangle t) - Y_i(t) \end{array} \right\|_2 \tag{2.7}$$

for some node i, where $\|\mathbf{x}\|_2$ is the Euclidian norm of $\mathbf{x}$.

Average migration rate φ_{avg} is simply the average of all an atom's nodes' migration rates (weighted by node spacing) at a given time, or

$$\varphi_{avg}(t) = \frac{1}{L_a} \sum_{i=1}^{m} \triangle S_i \varphi_i \tag{2.8}$$

where $L_a = \sum_{i=1}^{m} \triangle S_i$ is the atom length, m is the number of nodes comprising the atom, and $\triangle S$ was found by first-order differencing. Average migration condenses the local migration activity along a meander loop into a single measure.

Centroid migration rate, φ_{cen}, considers the movement of the centroid of the polygon formed by joining an atom's cutoff nodes with a line segment. Equation (2.9) specifies the centroid coordinates of a polygon composed of m nodes computed from its moments of inertia.

$$\begin{array}{c} X_C = \frac{1}{6} \sum_{i=1}^{m} \frac{6x_i y_i \Delta x_i - 3x_i^2 \Delta y_i + 3y_i \Delta x_i^2 + \Delta x_i^2 \Delta y_i}{y_i \Delta x_i - x_i \Delta y_i} \\ Y_C = \frac{1}{6} \sum_{i=1}^{m} \frac{-6x_i y_i \Delta y_i + 3y_i^2 \Delta x_i - 3x_i \Delta y_i^2 - \Delta y_i^2 \Delta x_i}{y_i \Delta x_i - x_i \Delta y_i} \end{array} \tag{2.9}$$

where $\Delta x_i = x_{i+1} - x_i$, $x_m = x_0$, and $\Delta y_i = y_{i+1} - y_i$, $y_m = y_0$. The centroid migration rate φ_{cen} is then computed by Equation (2.7) with $(X_i, Y_i) = (X_C, Y_C)$. Computed as such, the centroid migration rate is an integrated measure of all modes of atom migration, i.e. translation, rotation, extension, and expansion [110]. For example, downstream translation of an atom and streamwise-perpendicular growth of the atom may have similar centroid migration rates yet result in significantly different atom planform shapes.

Atom growth rate ($\frac{dL_a}{dt}$) simply measures the rate of change of length:

$$\frac{dL_a}{dt}(t) = \frac{L_a(t+\triangle t) - L_a(t)}{\triangle t} \tag{2.10}$$

for some atom a.

Migration rates are normalized by the space scale ($\mathcal{L}_o$) and time scale (τ_o) characterizing the length growth rate that emerges naturally from the structure of the solution for excess bank velocity given by Equation (2.2) and from the differential equations controlling migration of the channel axis given by Equations (2.3) and (2.4). They read $\mathcal{L}_o = B/|\lambda_o| = D_o/2C_{fo}$ and $\tau_o = \mathcal{L}_o/E_oU_o$. The former essentially controls the exponential decay of spatial disturbances of the flow field [37] and in the sub-resonant regime has been found to attain values similar to the morphodynamic length scale emerging from more refined models [36]. The latter is simply dictated by the equation describing how the centerline evolves in time and the bank erosion law.

Dynamic Trajectories

As an atom evolves in time, its dynamic trajectory is recorded by the set of dynamic measures describing its evolution. Here we show how average migration rate, centroid migration rate, and length growth rate change in time for individual atoms of each type of cutoff shape (i.e. *round*, *simple*, or *long*) and characterize the variability of dynamic trajectories simulated by our HIPS model. Despite a substantial variability in dynamic signals, a significant connection is demonstrated between cutoff geometry and dynamics.

Near inception, atom length growth rates $\left(\frac{dL_a}{dt}\right)$ remain slow but increase until eventually reaching a maximum growth rate and then monotonically decreasing (Figure 2.8a). The trends in the modeled growth rate trajectories agree with both field observations [111] and theoretical analyses [112]. Empirically, the amplitude growth rate of real single bends typically rises to a peak before decreasing, while its migration speed decreases monotonically [111]. Theoretically, the nonlinear solution of the integro-differential equation governing the planimetric evolution of a periodic sequence of meanders indicates that early in a meander's life, the fundamental harmonic (that is, the sine-generated curve of [113]) grows linearly. After this phase, the third harmonic (represented in the Kinoshita curve) is also excited leading to a nonlinear meander growth that progressively retards. As a result, the meander growth rate increases slowly during the linear phase, attains a maximum and then decreases as the third harmonic is activated. Additionally, the downstream-migration rate is found to decrease to very small values before cutoff while the rate of bend amplification

grows to a peak and then decays slowly. As this evolution takes place, the meander progressively fattens and becomes skewed upstream due to the growth of the third harmonic.

An atom's average migration rate is greatest near its inception, but similarly to growth rate, it monotonically decreases after attaining a maximum (Figure 2.8b). The peaks in average migration rate trajectories occur well before those in growth rate trajectories, rendering them useful metrics of historic dynamics. Note that the time axes in Figure 2.8 are not identical; because inception and cutoff are not standard across all atoms, the dynamic trajectories were aligned such that their peaks occur at $t = 0$ to establish a benchmark for meaningful comparisons between trajectories. Average migration rate trajectories for *simple* and *long* atoms occupy distinct regions, with *simples* exhibiting higher rates. As with geometric variability, *rounds* also display more dynamic variability than other atom shapes.

The irregularity of centroid migration trajectories prohibits meaningful presentation of their dynamic trajectories as shown for average migration and length growth rates in Figure 2.8, but the centroid migration rate nevertheless provides a different perspective on the connection between dynamics and geometry. This rate (φ_{cen}, Figure 2.9a) is evidently connected with the anatomy of an atom which is divisible into two distinct parts: a head and tail(s). An atom's head is the reach of atom containing the apex of the bend between two inflection points. Heads roughly correspond to the classic notion of a meander bend as the reach of a river between inflection points. Tails are simply the portions of the atom that are not its head. As shown in Figures 2.9b-d, an atom may have zero, one, or two tails. The tails of an atom can contain the apex of a less-developed (hence faster-migrating, see Figure 2.8b) adjacent loop; the high curvatures of such nearby loops induce faster migration of tails compared to their corresponding heads. The presence of tails dramatically affects the centroid migration rate (Figure 2.9a) and generally acts to diminish φ_{cen} magnitudes. For example, the tail-less atom in Figure 2.9b has the fastest φ_{cen} among the three types; φ_{cen} diminishes with an increased number of tails. This effect of tails is perhaps unsurprising, as tails add weight opposite to the direction of apex growth thereby suppressing the outward migration of the centroid. Interestingly, tails also influence φ_{cen} by imparting a local maximum into the signal (Figure 2.9a, single and double tail) corresponding to their migration toward cutoff. As tails migrate toward each other, they

begin to straighten. The peaks in φ_{cen} correspond to the straightening of the tails (i.e. tails approaching smaller $|C|_{avg}$) which acts to significantly reduce the weight of the tails on the centroid location. Not only is the magnitude of φ_{cen} dependent on tail behavior, the timing of its maximum (i.e. $max\left(\varphi_{cen}\right)$) also depends on the number of tails; more tails lead to earlier peaks (relative to time of cutoff).

The three dynamic measures show different aspects of an atom's evolution, but they are not independent of each other. Average migration rate peaks shortly after inception and then monotonically decreases until cutoff, whereas the growth rate is small near inception and grows to a maximum value before decreasing until cutoff. A typical *simple* atom (Figure 2.10) shows that the occurrence of these maximum or minimum dynamic metrics is not simultaneous. Average migration and centroid migration appear correlated until the tails of the atom begin affecting the centroid migration rate, causing its rise despite the decreasing overall average migration rate. Despite some apparent correlation, each measure provides unique information about the modes of planform migration.

2.4.3 Connecting Geometry and Historic Dynamics

A meander loop's dynamics arise from the continuous feedbacks between the morphodynamic, hydrodynamic, and geometric processes at play, and its planform shape bears the signature of their interaction. The relationship between a meander bend's curvature and dynamics (i.e. migration rates) has been explored in both real [114, 115, 116, 117] and simulated [35] channels, but these studies only consider instantaneous relationships. If meander bends remember their formative dynamics, a connection should exist between the bend's current planform configuration and the dynamic history that brought it to that state. This hypothesis, that the signature of formative dynamics remains in cutoff shapes, is tested using the methodologies developed in the previous two sub-sections.

A simple linear correlation analysis between each atom's maximum average migration rate and more than 30 metrics of cutoff atom geometry revealed the two strongest correlating variables are the efficiency ratio A_{cut}/L_{cut} (Figure 2.11a), which refers to how efficient an atom's centerline length at cutoff was in reworking the floodplain, and the apex curvature at cutoff $|C|_{max}$ (Figure 2.11b). This is perhaps an unsurprising result considering the work of [118] who showed that within a HIPS-type model both curvature and stream length

are of similar importance to meandering river migration dynamics. The consideration of both efficiency ratio and apex curvature improved predictions of maximum average migration rate (Figure 2.12). Maximum growth rates and maximum centroid migration rates produce similar results to Figure 2.12; that is, cutoff atom geometry predicts all three dynamic metrics well. However, because an atom's maximum average migration occurs very early in its life (see Figure 2.12), it provides the earliest measure of its dynamics and implies that the geometry at the end of an atom's life contains information about its dynamics near the time of its inception. Furthermore, the signature of formative dynamics in cutoff shapes supports the notion of a critical period early in a meander bend's life when its dynamic trajectory is most sensitive to perturbation. Deviations from the apparent trend in Figure 2.12 are mostly due to cutoffs occurring immediately upstream. Such cutoffs serve as high-curvature perturbations that may migrate downstream into the upstream-tail of an atom, and the maximum migration rate is amplified when this perturbation coincides with the peak growth rate of the downstream atom. Consistent with geometric and dynamic metrics, *rounds* exhibit the most variability in the predictive relationship between cutoff geometry and dynamics.

2.5 Discussion

The life story of meander bends predicted by a HIPS formulation is told through their extraction as atoms. An atom undergoes a birth and death, and its anatomy is composed of a head corresponding to the reach of centerline containing the apex of the bend between two inflection points and tails corresponding to the lengths of stream between the inflection points and cutoff locations. The death of an atom is marked by cutoff, and its timing for a given atom depends on i) the atom's dynamic history, ii) nearby perturbations, and iii) the overall river planimetric configuration. At its birth an atom is usually a mere squiggle of centerline (e.g. Figure 2.3b) and therefore cannot be easily visually detected. With respect to each of the three dynamic measures, *simple* atoms tend to migrate fastest and hence reach cutoff sooner than other geometries. *Long* atoms migrate the slowest and therefore live the longest before cutoff. The variability in *round* geometries is also seen in their dynamic trajectories, reflecting the influence of randomly-timed nearby perturbations due to cutoff. Conversely, *simples* and *rounds* have dynamic trajectories that cluster with smaller

variability. Some atoms' maximum growth rates (see slowest-growing *rounds*, Figure 2.8a) are apparently achieved early in their lives, suggesting that their cutoff geometry is set early in their life. This implies a critical period near inception when perturbations are most critical to development.

In our HIPS model, model dynamics do not include physical mechanisms such as transitions from sub- to super-resonant conditions as described by [36], and hence cutoff is the only localized perturbation mechanism through which new meander bends may form. This property, along with uniform treatment of post-cutoff centerline smoothing begs the question: how do the various observed morphodynamics arise? An atom's morphology is determined primarily by the local hydrodynamics driving bank erosion (u_b, Equation 2.2), but these local dynamics depend on both nonlocal and reachwide conditions that vary in time. For example, U_o, D_o, and λ_o are reachwide variables that affect the migration rate of a single node. Furthermore, the convolution integral in Equation 2.2 represents a nonlocal (yet non-reachwide) dependence on upstream curvatures. The hydrodynamics of an atom incorporate the variability from each of these scales and thus promotes variability in atom morphodynamics. In addition to variability in local hydrodynamics, the atom deformation process itself imparts an intrinsic geometric nonlinearity through the equations of migration (see [119]). The occurrence of cutoff imparts yet another source of variability into the migrating meandering river.

Ultimately, the various emergent atom morphodynamics and morphologies reflect the nonlinear interactions between the multi-scale dependent hydrodynamics, the migration equations, and the occurrence of cutoffs. Even in a relatively simple modeling environment like ours, unraveling the contributions of each of these to specific morphologic or dynamic variability presents a considerable challenge. A comparison of the computed terms contributing to excess bank velocity u_b reveals curvature effects are typically stronger than the slowly-varying reach-wide ones especially near cutoffs. That is, local curvature perturbations account for more of the variability in the distribution of shapes shown in Figure 2.6d; the resulting discontinuity in curvature after cutoff serves as the initial configuration of a new atom. Cutoffs sometimes also clearly affect nearby well-developed atom dynamics through the nonlocal term, usually acting to "artificially" augment migration rates (for example, the outliers in Figure 2.12). In the absence of localized perturbations, cutoff

geometries simulated by the HIPS model tend toward a uniform *simple* shape, suggesting an inherent archetypal form embedded in the model dynamics.

The curvature, area, and length of a meander loop at cutoff can be used to predict historic maximum rates of growth and migration as demonstrated by Figure 2.12. For example, Figure 2.6a shows oxbow lakes along the Mississippi River that had already formed at the time of the earliest aerial photographs in 1937; observations of their formative dynamics are unavailable. However, if this reach of the Mississippi River were well-described by a HIPS modeling scheme, historic migration rates of each loop may be estimated from their present-day oxbow c_r ratios. Even without fully modeling the historic evolution of this reach of the Mississippi River, relative migration rates of each oxbow may be inferred from a cursory analysis of their geometries.

The results presented herein were made possible only because the entirety of an atom's life is known, including the cutoff. If the cutoff location and time are known, the rest of the atom's evolution may then be backtracked until its origins and initial conditions are known. The algorithm introduced here requires highly temporally resolved centerline realizations to accurately track cutoff node histories. In principle this algorithm could be applied to cutoff loops from a series of aerial images with sufficient temporal resolution if a consistent method for gridding centerlines were established. Alternatively, adopting the classical notion of a meander bend as the reach of stream between inflection points (i.e. atom heads) would permit the technique's application to real reaches that have not yet been cut off. In that case, the methodology here is still useful because the heads are easily extracted from complete atoms while bypassing the previously discussed problems associated with automatic inflection point detection.

2.6 Concluding Remarks and Future Work

The primary motivation of this work was to test the hypothesis that bend scale cutoff geometry contains information about its formative dynamics. Testing this hypothesis requires both a large number of meander bends whose planimetric bend evolutions from inception until cutoff are well-resolved and a record of nearby disturbances that might affect the geometric-dynamic predictive relationship due to the nonlinear growth of local instabilities. In the absence of sufficient observational data, we resorted to a long-time,

physically-based numerical model that couples hydrodynamics, morphology, and cutoff and found that the deterministic model dynamics do indeed show evidence that meander cutoff shape contains the signature of formative meander migration dynamics. A necessary step for such an analysis requires the isolation of individual bends through time, and this work presented a robust algorithm to automatically extract single bends from long-time simulations of meander migration.

The ultimate objective, of course, is to apply these findings to real meander bends where "signature-shredders" [120] such as catastrophic floods or geologic activity may obscure or erase this signature. A critical component of such studies lies in the ability to discern which dynamic and geometric metrics might be most closely related. Limited observed meander dynamics data obscured by natural heterogeneities renders identifying such metrics problematic. Within the sterile modeling environment of this work, the apex curvature of cutoff meander bends and the efficiency ratio, defined as the area of a cutoff bend divided by its length, emerge as powerful geometric metrics that retain information about a bend's dynamics in its formative (early) stage of life. Furthermore, maxima of dynamic trajectories serve as suitable metrics characterizing atoms' historic evolutions. Informed by these clues from numerical modeling, future work will test the metrics and relationships developed here in real rivers such as highly-active meandering Amazonian rivers for which over thirty years of Landsat imagery is available. We are also applying and refining our metrics to more complex numerical models which incorporate additional physics and natural variability.

2.7 Figures and Table

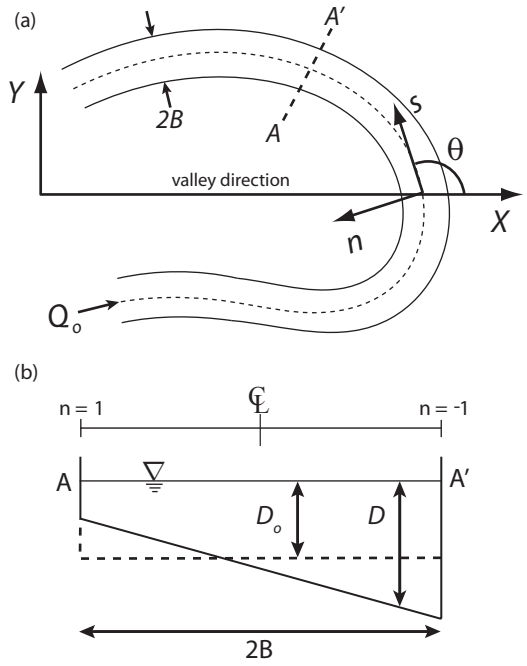

Figure 2.1: Coordinate systems and modeling variables. a) Planform view of a meander of constant width $2B$. The s coordinate always points in the streamwise direction, and the X-axis is aligned with the valley direction. b) Cross section of the channel. The outer bank corresponds to $n = 1$ and at the centerline $n = 0$.

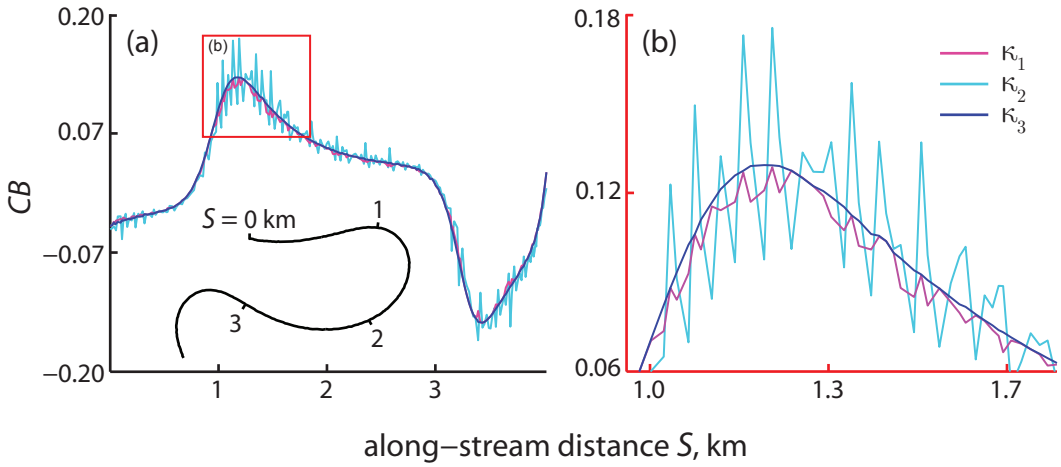

Figure 2.2: Comparison of three different curvature computation methods for the bend shown in a). The 4 km bend is scaled such that the aspect ratio is 1:1, and the upstream end is denoted by $S = 0$. The box around the region of maximum curvature in a) is expanded in b). Definitions for computing each κ_i are discussed in Section 2.2.2. Derivatives are estimated by first-order differencing. We employ κ_3 for the analyses herein.

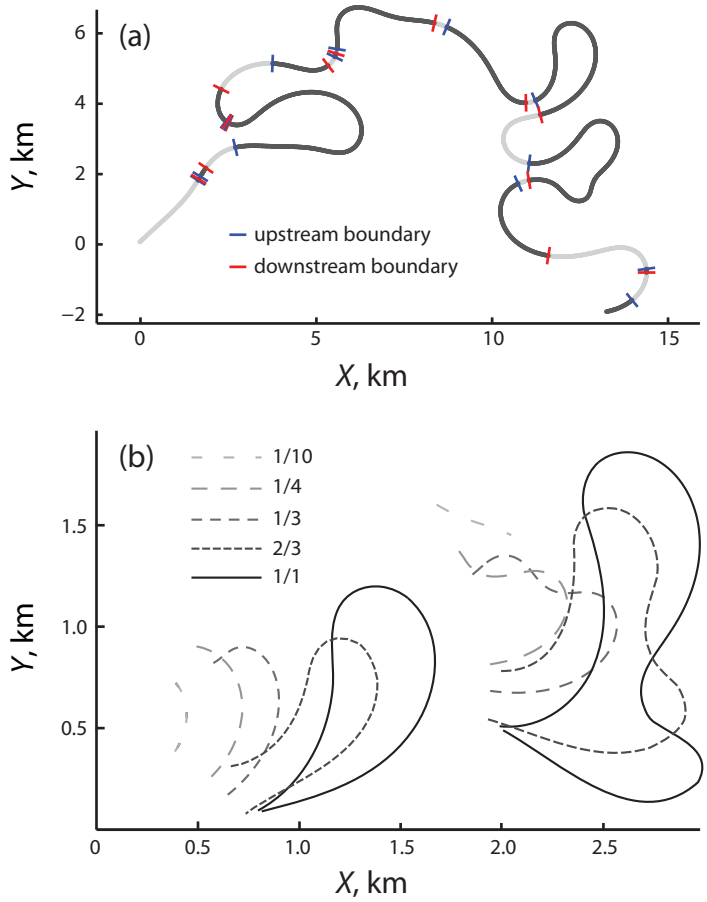

Figure 2.3: a) The dissection of a centerline reach into atoms. The dark portions of centerline are atoms whose extents are marked by blue (upstream) and red (downstream) boundaries. Some atoms are as short as three nodes, while some are approaching cutoff. The lighter portions of the centerline are fractions of atoms whose boundaries are yet unknown because their cutoff nodes do not yet exist. b) The development of two atoms' centerlines from inception until cutoff. Legend values represent the fraction of atom length L_a to its length at cutoff L_{cut}, i.e. 1/10 shows an atom at one-tenth its cutoff length (near inception) and 1/1 shows the atom at cutoff. The left atom shows the growth of an unperturbed single-loop, while the right atom develops a second loop due to a cutoff immediately upstream that occurs between 1/4 and 1/3. This figure highlights the ambiguity of atom inception; as tracking proceeds backwards, the atom loses its loop-like form and becomes a segment of almost constant-curvature centerline.

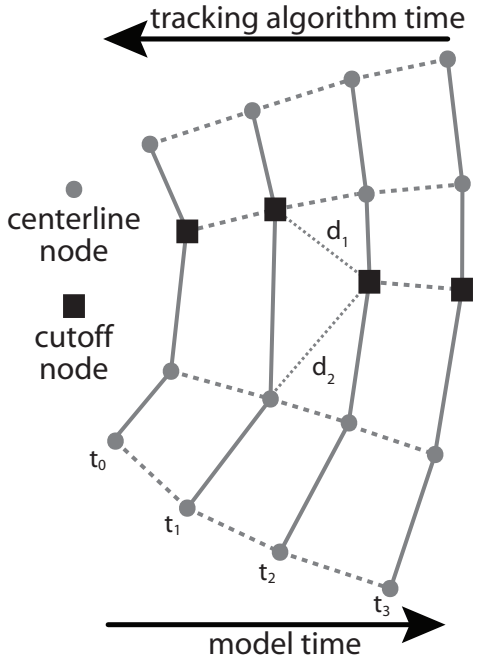

Figure 2.4: How the tracking algorithm deals with centerline node interpolations. Circles are centerline nodes and squares are the cutoff node being tracked by the algorithm. As the model advances in time, the distance between nodes increases until it becomes larger than the node spacing threshold, at which time a new node is interpolated at t_2. Conversely, the algorithm that tracks the cutoff node works backwards through time and sees the cutoff node removed after t_2. The cutoff node at t_1 is selected based on the shortest distance to the nearest neighboring nodes; in this case $d_1 < d_2$.

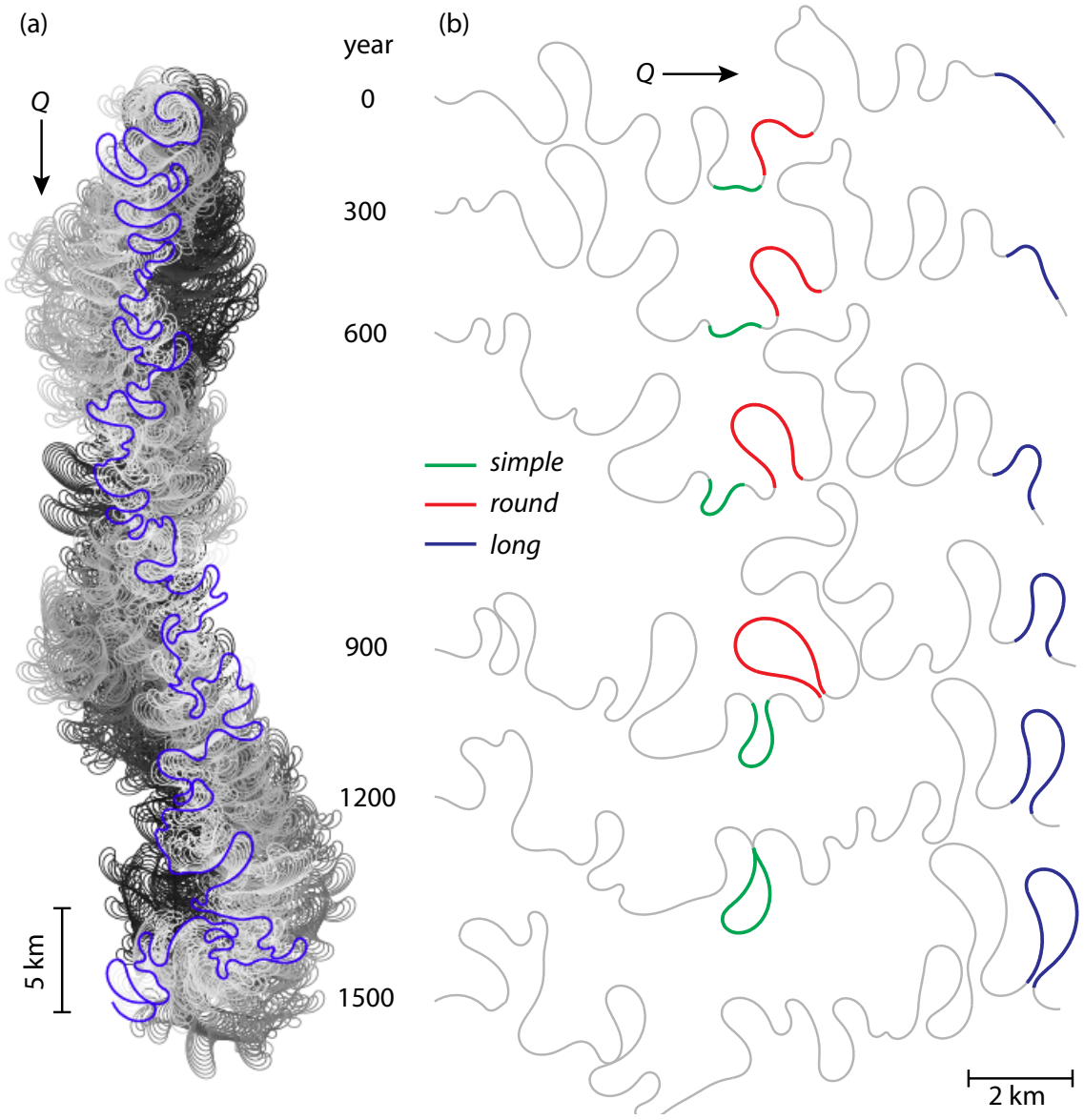

Figure 2.5: Results of the long-term simulated meandering river. a) 30,000 years of modeled centerline realizations. Older centerlines are darker; the blue centerline shows $t = 30,000$ years. The upstream boundary condition fixes the first centerline node in place, leading to the formation of the spiral pattern at the upstream boundary. No restrictions are placed on the downstream node so the river may migrate freely. b) A reach of simulated centerline selected to show the growth and cutoff of all three atom types. Realizations are 300 years apart. Note the complex multilobe meander that starts as double-lobed but develops a third lobe before cutting off between 900-1200 years.

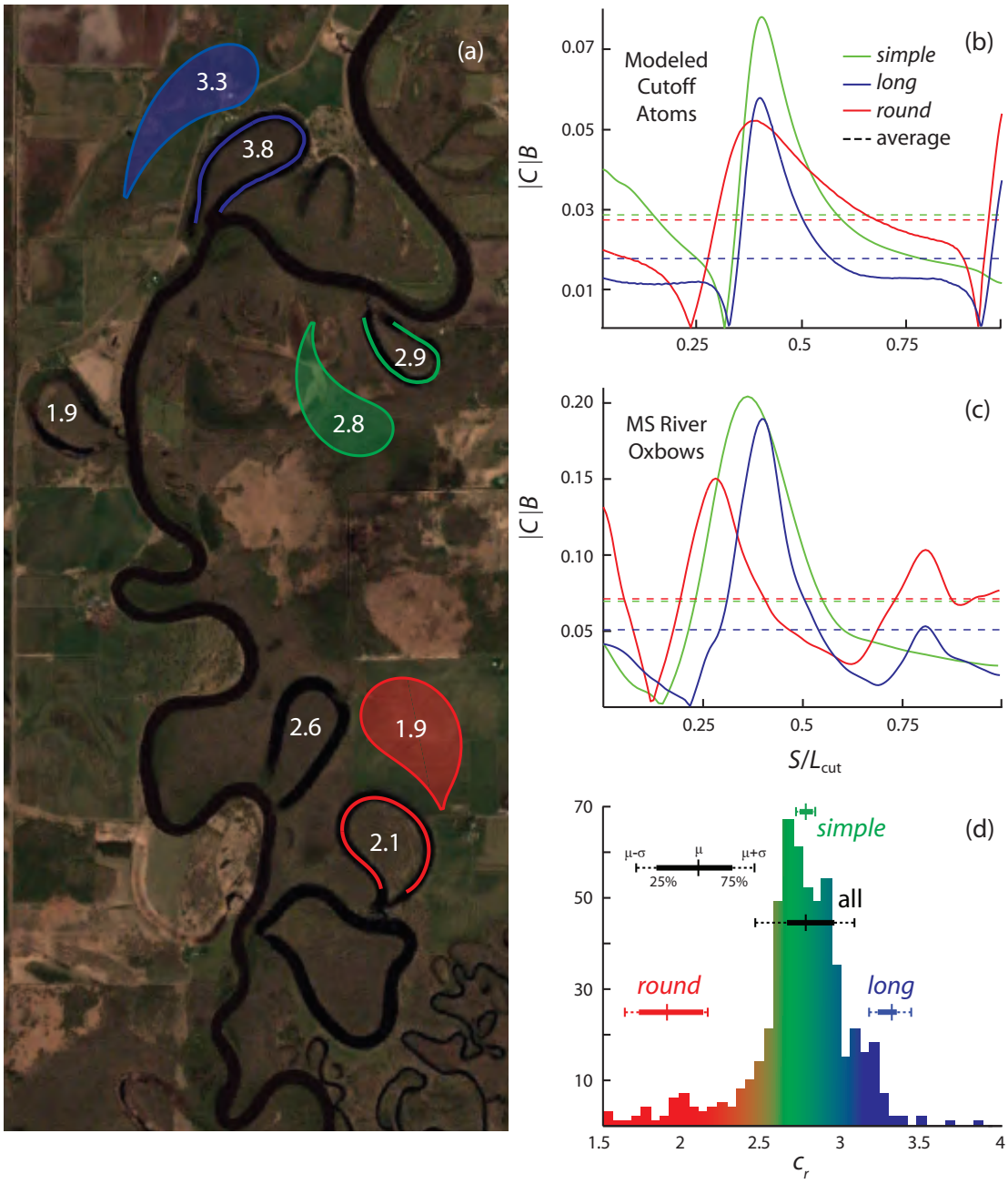

Figure 2.6: (Caption next page.)

Figure 2.6: (Figure previous page.) Geometric classification via curvature measures of modeled and real meander loops. a) Aerial imagery of a reach of the Mississippi River in Minnesota, USA. Centerlines of three oxbows have been traced in colors corresponding to the cutoff atom geometry they most resemble. The shaded meander loops are cutoff atoms simulated by the model and are positioned next to similarly-shaped oxbows. White numbers in the center of each oxbow or atom are c_r values. b) Absolute value of curvature signals for the cutoff atoms simulated by the model shown in a). Dashed lines are average absolute curvatures. b) Absolute value of curvature signals for the traced oxbow lakes of the Mississippi River shown in a). c) The distribution of c_r (ratio of apex curvature to average curvature) simulated by the model shows how c_r serves as a good metric for ordering meander loops of various geometries by shape. The color gradient of the c_r histogram emphasizes that simulated atom shapes are characterized by a spectrum rather than falling neatly into one of the three archetypal shape (*simple*, *round*, *long*) categories. Statistics for each group have sample size $n = 25$, while $n = 552$ for all cutoff atoms. The c_r mean value for all cutoff atoms is 2.77. Map data: *Google Earth: DigitalGlobe.* 46°37'31.36"N, 93°38'13.31"W. Imagery date 7/2/2011.

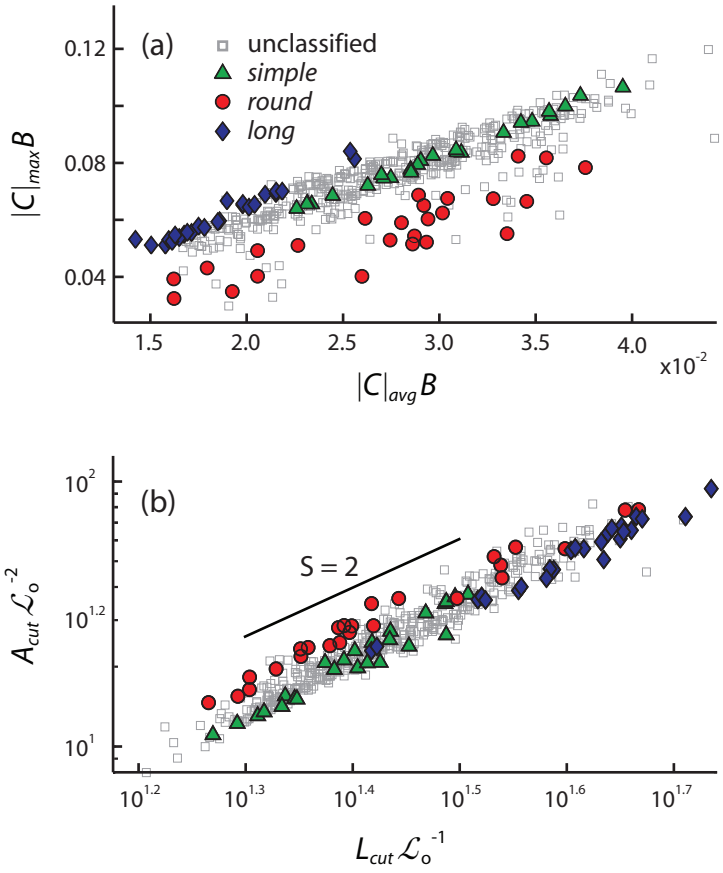

Figure 2.7: Geometric phase spaces for all *single* atoms at cutoff. a) Relationship between mean and maximum absolute curvatures for each *single* cutoff atom made dimensionless by channel width. Each symbol represents a unique cutoff atom geometry; unfilled circles are unclassified cutoff atoms, while filled green triangles are *simples*, red circles are *rounds*, and blue diamonds are *longs* as described in the text. The shape groups tend to follow straight lines because shape classifications were based on the approximately constant ratio $|C|_{max}/|C|_{avg}$. b) Log-log relationship between cutoff length L_{cut} and area A_{cut} for each *single* cutoff atom. Area and length are nondimensionalized with $\mathcal{L}_o$, the length scale relevant to meander migration described in Section 2.4.2. For a given cutoff length L_{cut}, *rounds* tend to cover a larger area whereas *simples* and *longs* occupy approximately the same area. The average slope of the marker cloud is two, since $A \sim L^2$ for nonfractal geometries.

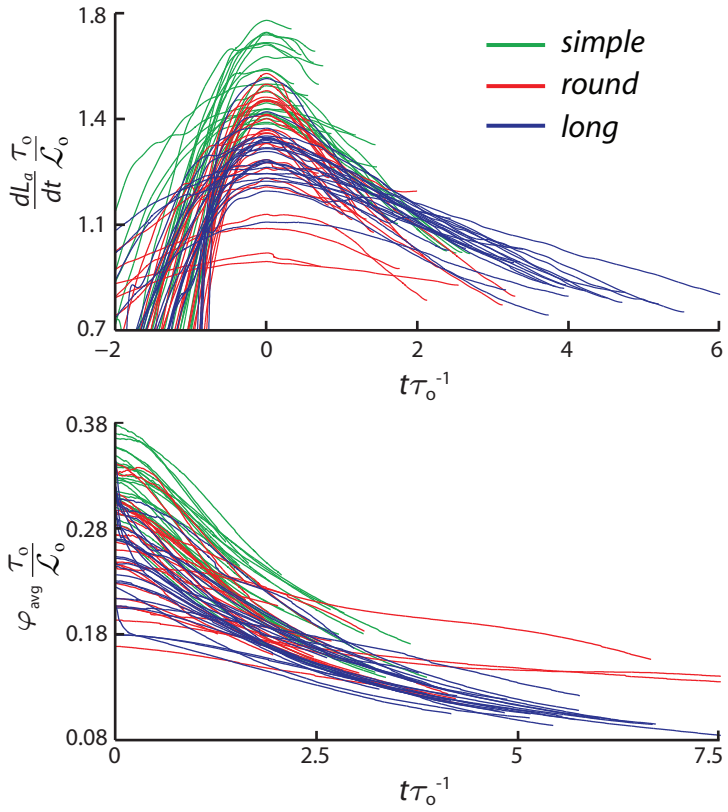

Figure 2.8: Collections of individual atoms' dynamic trajectories. a) Atom growth rates $\frac{dL_a}{dt}$. Each trajectory represents the evolution of a single atom's growth rate from near inception until cutoff. The right end of each trajectory corresponds to cutoff. Trajectories are aligned as described in Section 2.4.2 such that their maxima occur at $t = 0$ for comparison purposes. b) Average atom migration rates φ_{avg}. Again atoms are aligned such that their maxima correspond to $t = 0$. Colors correspond to the shape groups defined in Section 2.4.1. *Simples* and *longs* are well-distinguished but *rounds* exhibit significant variability.

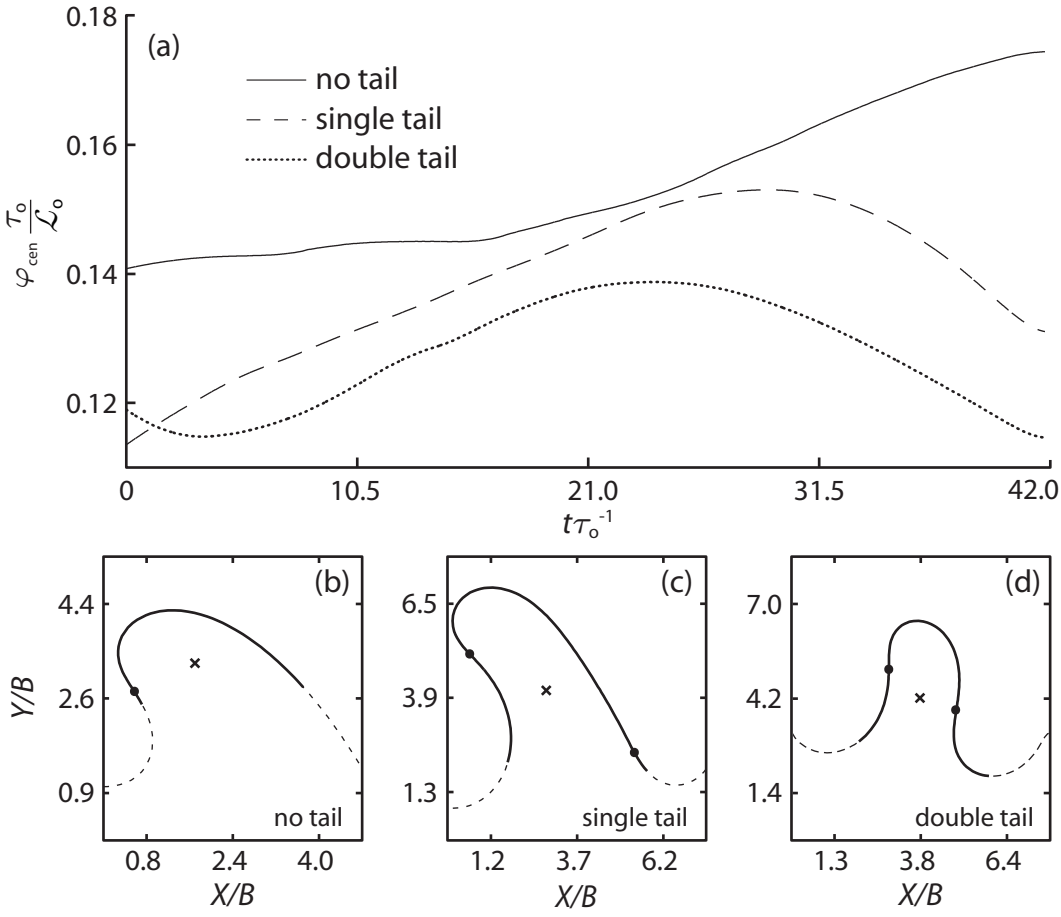

Figure 2.9: The effect of tails shown via centroid migration rates φ_{cen} through time for the three atom centerlines. See Section 2.4.2 for interpretation. a) Cutoff occurs at $t/\tau_o = 42.0$. b-d) The planforms for each of the atoms of different tail-types are plotted at $t = 0$. The solid black lines are the atoms and the continuing dashed line is the river centerline. The black dots in b-d) show the inflection points for each atom centerline, and the x's mark the centroid of each atom.

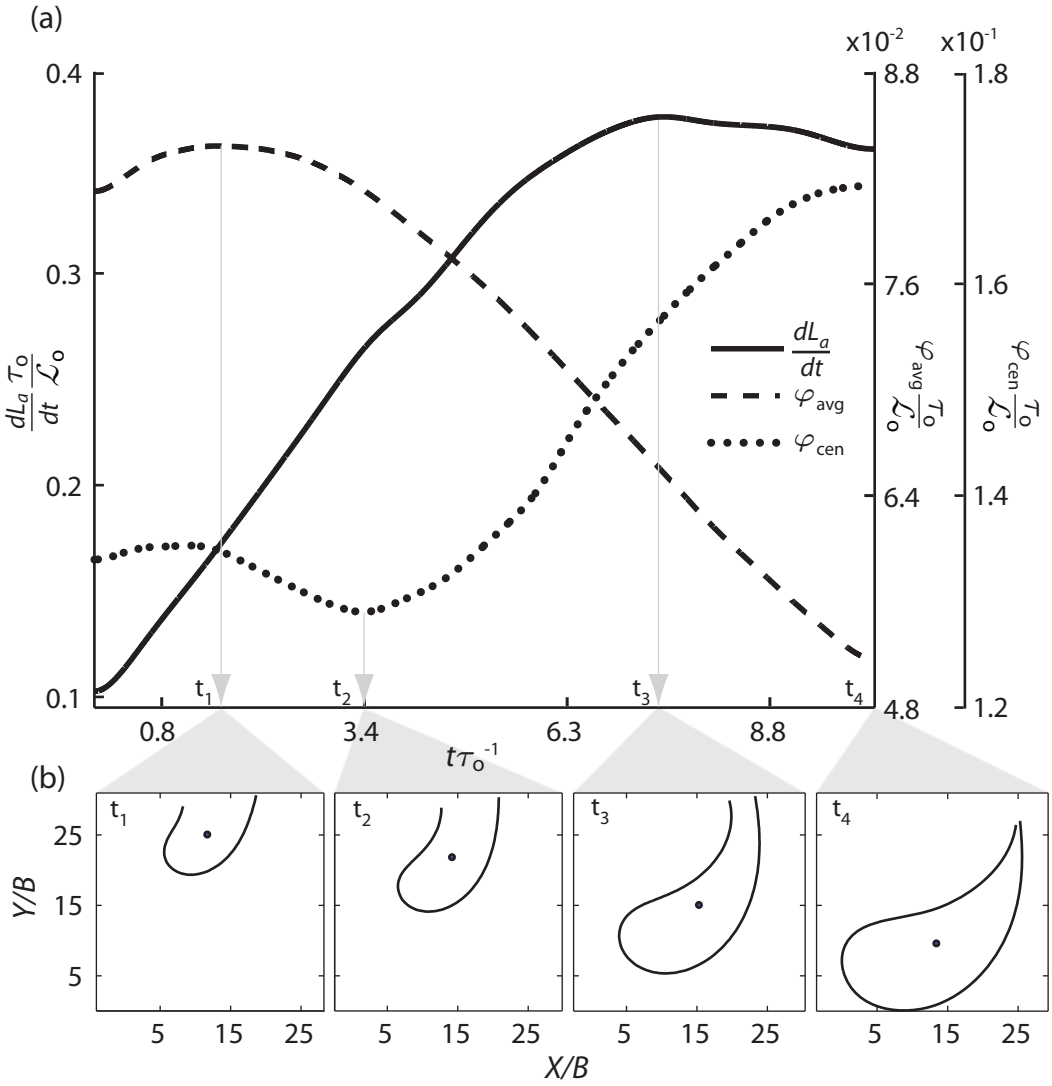

Figure 2.10: How dynamic metrics simultaneously evolve for a single atom. a) The evolution of a typical *simple* atom is visualized through three dynamic measures changing in time: growth rate (solid line), average migration rate (dashed line), and centroid migration rate (dotted line). Dynamic measures are nondimensionalized by the time and space scales described in Section 2.4.2. Vertical lines are drawn from each of the dynamic signals' local maxima or minimum to their times on the x-axis. The atom's planform is shown plotted at each of these times (t_4 corresponds to cutoff) in b). The dot inside each of the plotted atom centerlines shows the atom's centroid. After t_2 the left tail of the atom begins rapidly migrating toward the right causing the rebound of φ_{cen} and the atom's eventual cutoff.

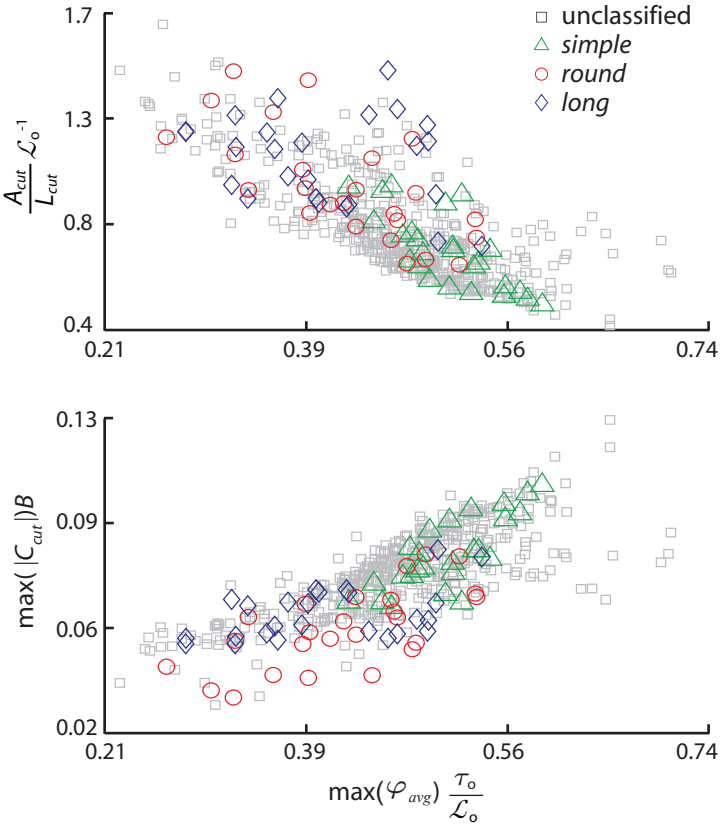

Figure 2.11: Relationships between cutoff geometry and historic dynamics for 552 *simple* cutoff atoms. a) The efficiency ratios A_{cut}/L_{cut} normalized by $\mathcal{L}_o$ for all cutoff atoms are plotted against their maximum average migration rates (shown in Figure 2.8b). Efficiency ratio refers to the efficiency of a given length of stream in reworking the floodplain. b) Each cutoff atom's apex curvature normalized by B is plotted against its historic maximum average migration rate.

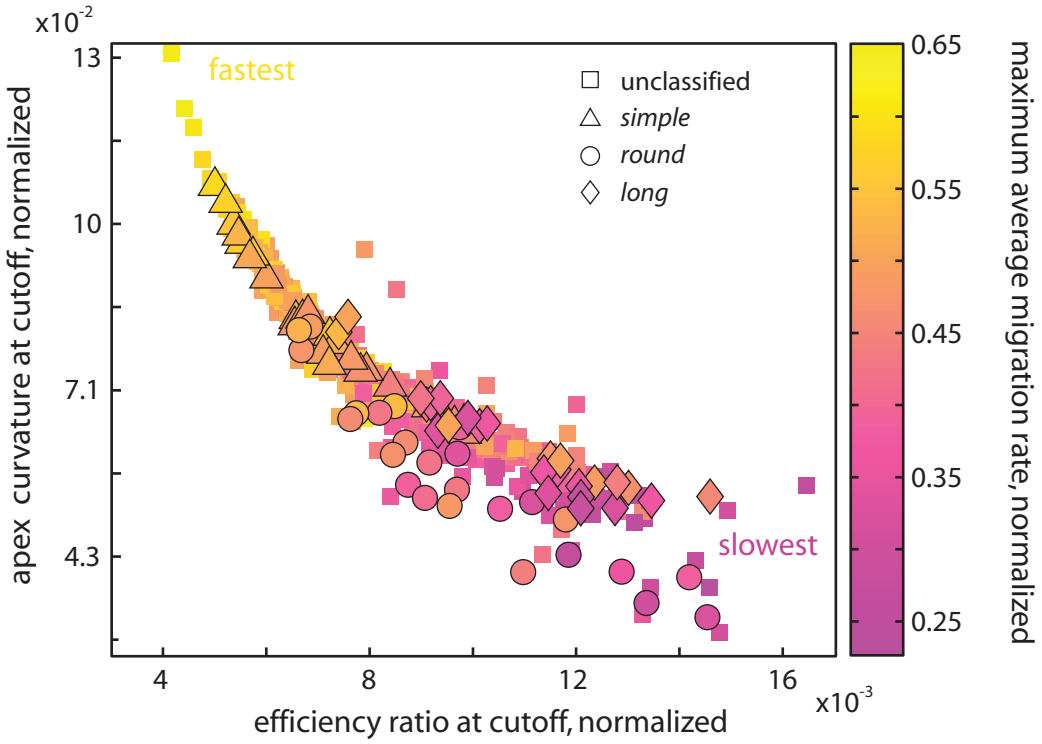

Figure 2.12: Connection between cutoff geometry and historic dynamics revealed. Measurements of atom geometries (x- and y-axis) at the end of each atom's life and a measure of their dynamics (coloration) made early in the atom's life link an atom's dynamic history with its cutoff shape. For each atom the dimensionless efficiency ratio at cutoff $A_{cut}/L_{cut}\mathcal{L}_o^{-1}$ is plotted against the dimensionless apex cutoff curvature $\max(|C|_{max})B$ and the point is colored by the dimensionless historic maximum average migration rate, $\max(\varphi_{avg})\tau_o/\mathcal{L}_o$ (i.e. the maxima of trajectories shown in Figure 2.8b). The fastest migrating atoms correspond to those with the highest apex curvatures and lowest efficiency ratios (top-left) and vice versa.

Chapter 3

Nonlinearity of meandering river planforms revisited

Meandering river planform evolution is driven by the interaction of local nonlinear processes and cutoff dynamics. Despite the known nonlinear dynamics governing the evolution of meandering rivers, previous attempts have found at most a weak signature of these dynamic nonlinearities in static meander planform morphologies. In this chapter, we unambiguously show that the spatial structure of meandering centerlines does indeed encode dynamic nonlinearities in a numerically simulated meandering river and three natural rivers. The effects of cutoffs on nonlinearity are investigated through the temporal evolution of the simulated river as well as annual observations over 32 years of an active, tropical meandering river. Cutoffs are found to obscure the imprint of dynamic nonlinearity, but by identifying the scales that contribute most to nonlinearity we show that cutoffs themselves also act as a source of nonlinearity.

3.1 Introduction

Physically-based, reductionist theory of long-time meander evolution developed over the past four decades has identified nonlinearities in the essential governing deterministic dynamics of meander formation and evolution. For example, the existence of a geometric nonlinearity was noted by [2] who reported that conversion from Cartesian to intrinsic

coordinates imposed nonlinearity on the evolving centerline structure. This geometric nonlinearity is expressed through the development of higher-order modes of sine-generated curves [121, 112] by fattening and skewing meander bends. [112] later generalized this notion via geometrical arguments (their Figure 2) showing that any curve evolving through time is governed by

$$\frac{\partial \zeta}{\partial s} = \frac{\partial \theta}{\partial t} - \frac{\partial \theta}{\partial s} \int_0^s \zeta \frac{\partial \theta}{\partial s} ds \tag{3.1}$$

where ζ is the rate of lateral movement at some distance s along the curve, θ represents the angle of the curve with respect to the horizontal, and $\partial\theta/\partial s$ is the curvature. This equation demonstrates a spatial nonlinearity inherent in evolving meanders due to the quadratic form of $\partial\theta/\partial s$ in the integral term. In addition to the inherent geometric nonlinearity of meander evolution, Equation 3.1 may also include dynamic nonlinearities arising from hydrodynamics, bed morphology, and/or their interaction expressed through the formulation of the lateral rate of migration (ζ). The earliest hydrodynamic models of flow through meander bends were achieved through perturbation analyses wherein the higher-order, nonlinear terms were discarded under the assumption of small centerline curvatures (e.g. [122, 2]). Eventually, 2D depth-averaged nonlinear hydrodynamic models were developed that included the discarded nonlinear terms that capture the nonlinear coupling of downstream velocity with secondary cells that deform the vertical flow profile [123, 4, 81]. The retention of these nonlinear terms in the governing hydrodynamic equations was shown to result in significantly different planform morphologies [87].

Nonlinearities associated with sediment dynamics have similarly been gradually included in models of meander evolution, though to a lesser extent than hydrodynamics. The nonlinear Exner equation accounting for conservation of mass is typically linearized (e.g. [112]) and closed with a nonlinear expression for bedload transport in the downstream direction, i.e. $q_{s,s} \sim \tau - \tau_c^m$ where τ_c is critical bed shear stress, and an assumed transverse bed profile that is related either linearly [80], sinusoidally [77], or exponentially [81] to local curvature. The observation of longer timescales of bed adjustment relative to the timescales of hydrodynamic forcings (i.e. floods) is often used to justify decoupling the hydrodynamics and morphodynamics [119], but the resulting sediment dynamics may still be forced

with a nonlinear flowfield through $\tau = f(u)$ for a velocity field u. Of course, 3D modeling using CFD techniques includes the full coupling of the nonlinear hydro- and morphodynamics and includes additional nonlinearities associated with turbulence [85, 124] and the expansion of the nonlinear terms of the Navier-Stokes and Exner equations into an additional dimension. Computational costs prohibit CFD simulations of meander trains over long times, but fully characterizing the effects of deterministic nonlinearities on planform morphology would require no less.

In addition to the small-scale deterministic nonlinear processes driving meander evolution, the occurrence of cutoff introduces a planform-scale threshold nonlinearity through the sudden removal of bends. Cutoffs have been argued to reduce overall spatial nonlinearity by removing older bends that have had more time to express the deterministic nonlinear dynamics of meander evolution [52, 3, 58]. However, local dynamics see cutoffs as perturbations to the system's state variables (e.g. slope, sediment flux, flow velocity) which may be magnified through the driving nonlinear dynamics and manifest through the planform morphology.

A handful of studies have suggested that meandering river planform morphodynamics exhibit chaotic behavior and self-organized criticality (SOC), both concepts resting on the assumption of a nonlinear dynamical system. [51] found evidence supporting a chaotic model for the curvature series of at least one natural river, although chaos was not similarly detected in simulated rivers [53]. The conceptualization of meandering rivers as SOC systems [125] was developed by [55, 126], including evidence from the power-law size-frequency distribution of oxbow lakes created by a simulated river [55]. Curiously, despite both theoretical justification for nonlinear processes driving planform evolution and empirical descriptions of planform morphodynamics by models requiring nonlinearity, direct attempts to detect and quantify nonlinearity have been unsuccessful in both real [52] and simulated [53] meandering centerlines. These studies cast signals of the spatial series of curvature into a phase-space in order to test for nonlinear and/or deterministic structure and found at most weak evidence of nonlinearity, suggesting that local nonlinear dynamics do not necessarily result in nonlinear spatial structure.

In this work, we show that the nonlinearity in the underlying meander evolution dynamics is manifest through the centerline curvature series of meandering rivers (Section

3.2). The effects of bend growth and cutoffs on nonlinearity are investigated for evolving centerlines: first using a long-time simulation of a meandering river where the underlying deterministic dynamics are exactly known, and then for annual realizations of an actively migrating, tropical meandering river over 32 years (Section 3.3). The sources of nonlinearity are further interrogated by identifying scales that contribute most to nonlinearity using wavelet-based techniques (Section 3.4). Implications of these results on the relationship between form and process in meandering rivers are discussed, as well as the caveats of interpretation (Section 3.5), and future research directions are identified (Section 3.6).

3.2 Detecting nonlinearity in two meandering rivers

The degree of nonlinear structure in a stationary signal, such as the curvature series of a river centerline, can be measured by comparing the signal with a surrogate of itself wherein its nonlinear structure has been destroyed, but its linear properties remain intact [127, 128]. The signal and its surrogate are cast into a phase space where their nonlinear structure is unfolded, and their difference is measured by the Transportation Distance (TD). Many surrogates are generated for a signal in order to test the statistical significance of nonlinearity and assess the degree of nonlinearity (DNL). In this section, the details of obtaining the curvature signal (Section 3.2.1), surrogate generation (Section 3.2.2), embedding in a phase space (Section 3.2.3) and computing the TD and DNL (Section 3.2.4) are given, followed by the application of these techniques to two meandering rivers in Minnesota, USA (Section 3.2.5).

3.2.1 Obtaining curvature signals

The spatial series of centerline curvatures used here to characterize meandering river planform morphology is given by

$$C(s) = d\theta(s)/ds \tag{3.2}$$

where C is the curvature, s is the along-stream distance, and θ is the channel direction defined discretely as $\theta_i = \tan^{-1}\left(\frac{y_{i+1}-y_i}{x_{i+1}-x_i}\right)$ for any two adjacent centerline nodes. As

the derivative of the channel angle, the curvature removes linear trends imposed by non-stationarities due to valley forcing or large scale heterogeneity in floodplain resistance, vegetation, etc. while capturing bend planform structure. Meandering river centerlines may either be digitized directly by hand from aerial imagery or maps [18] or calculated somewhat indirectly from digitization of banklines which may also be obtained by hand [129] or through image processing [130]. The choice of technique ultimately determines the sampling resolution and error. For measurements made directly on the centerline, such as meander wavelength and amplitude, errors associated with the digitization process are usually negligible. However, because curvature is a derivative measurement, errors in the original centerline discretization are magnified in the curvature signal and smoothing is required. The techniques presented here for acquiring curvature series with fidelity to the observed centerlines were developed using both hand-delineated (Minnesota rivers) and image processed centerlines (Ucayali River). After the centerlines were digitized, their x and y coordinates were smoothed with a Savitzky-Golay filter. A "temporary" curvature signal was computed according to Equation (3.2), and the number of bends N_b in the reach was estimated as the number of times this curvature signal crossed zero. A bend therefore was defined as a reach of river between two inflection points. The number of bends was verified by eye, and was noted to vary depending on the strength of the Savitzky-Golay smoothing filter due to the multiscale nature of meandering planforms [131]. The smoothed centerline was then resampled with evenly-spaced nodes with a density of $25N_b$ such that each bend contained 25 nodes on average. New nodes were interpolated by fitting piecewise parametric cubic splines to the smooth centerline [100] and integrating along the splines every $L/25N_b$, where L is the length of the reach. Finally, the curvature series was computed on the smoothed, evenly-spaced centerline according to Equation (3.2).

3.2.2 Generating completely linearized surrogates

Linear signals have statistical properties that are independent of their Fourier phases [127, 128]. For example, randomizing the Fourier phases of a signal has no effect on its autocorrelation structure, and a signal is therefore considered nonlinear if the randomization of its Fourier phases results in a significantly "different" signal [132]. Such modified signals, called surrogates, were introduced by [127] and have since been widely used in

many applications (see [133]).

A modified Iterated Amplitude Adjusted Fourier Transform (IAAFT) was used to generate a linear surrogate from a spatial series of curvatures $C(s)$ in four steps (see [134, 135]). First, the Fourier Transform decomposed the signal $C(s)$ into a series of various-frequency sinusoids, each with an associated amplitude and phase. Second, the phases of the component sinusoids were randomized, but the amplitudes were preserved. Third, the inverse Fourier Transform returns a signal with the same power spectrum. Finally, the values of the inverted signal are replaced by those in $C(s)$ via a rank-order matching process in order to ensure the same distribution of the original and surrogate series. This final step may cause minor mismatching between the original and surrogate spectra, and thus the entire procedure is iterated until a convergence criterion is met [133, 136]. The surrogate ultimately has the same values (probability distribution) and Fourier spectrum (autocorrelation) as the original signal. Multiple surrogates were generated from the same signal by performing different phase randomizations.

3.2.3 Casting signals and surrogates into embedding space

When a system's evolution equations are known a priori, it can be projected into a phase-space whose axes are the independent variables of the system, and the system's evolution through time is represented by a trajectory through the phase-space. The structure of the trajectory forms an attractor, or the set of points toward which the system tends to evolve. When the underlying deterministic equations are not explicitly and completely resolved as is the case with meander dynamics, the Takens theorem [137] states that under certain conditions, the attractor of the complete dynamic system may be reconstructed from a single measurement on the system through delay embedding. We assume the spatial series of curvatures as a measurement on the dynamic system and construct an m-dimensional embedding space with delay vectors of the curvature series:

$$\vec{C}_m = \left(C_{n-(m-1)\tau}, C_{n-(m-2)\tau}, \ldots, C_n\right) \tag{3.3}$$

where m is the dimension of the embedding space and τ is the lag. For a given series of length n, a total of $n-(m-1)\tau$ points will be contained in each of the m vectors. The embedding dimension m should roughly correspond to the number of independent

variables in the dynamic system. This dimension is determined through an evaluation of "false nearest neighbors," which are points in phase-space that are nearby in lower dimensions but separate when cast into a higher dimensional phase space [138]. In practice, the choice of m is constrained by the length of the signal, and large m are computationally infeasible. We tested $m = 2, 3, 4$ and found the results insensitive in agreement with others (e.g. [139, 140]), and thus used $m = 3$ for all analyses herein. The lag τ should be large enough to remove significant linear correlation between subsequent points in $\vec{C}_m$, which we estimated as the lag of the zero-crossing of the series' autocorrelation function.

3.2.4 Computing Transportation Distance and Degree of Nonlinearity

After reconstructing the attractors of the original curvature series and its surrogate using delay embedding, the difference between the attractors was estimated as the "distance" between the density functions of the two attractor geometries within the embedding space. This measure was developed by [139] as the Transportation Distance (TD) and is equivalent to the more intuitive Earth Mover's Distance [141] which simply measures the minimum amount of work required to transform one pile of dirt into another pile, where work is the amount of dirt to be moved times the shortest distance it must be moved [142, 143]. In our case, the piles of dirt are the densities of each attractor within the embedding space, and the minimum amount of work required is the TD [139]. The details of computing the TD are given in Appendix B. Larger TD indicates a greater difference between the structure of the two attractors and implies a greater difference between their underlying dynamics. Because distances are measured in an embedding space whose axes are defined by lagged vectors of the original signals, TD has units of the input signals. Other nonlinear metrics (e.g. Lyapunov exponents) are notoriously difficult to measure in real systems due to noise and insufficient signal length, but the TD has been shown to be more robust and revealing [140].

Given two series in an embedding space (in our case an original signal and its surrogate), the transportation distance (TD) metric [139] was used to compute their difference. Two series F and G were embedded within a phase space according to Equation 3.3. The domain occupied by F and G was discretized into B boxes by dividing each mi axis into $B^{1/m}$ intervals. The probability that series F occupies any box B_i was estimated as $f_i(B_i) =$

$N(F, B_i)/N(F)$, where $N(F, B)$ is the number of points in series F that lie within box B_i and $N(F)$ is the length of series F. The discretization of each m_i axis intervals may be performed such that either (a) each interval is the same size (equally spaced bins), or (b) each interval contains the same probability (equal probability bins). We employed the latter method herein as it added robustness against outliers. Now, let $\mu_{ij} > 0$ represent the amount of probability shipped from box B_i to B_j according to transportation plan μ. To preserve initial and final distributions of F and G, the following conditions must be met: $\sum_{i=1}^{B} \mu_{ij} = f_j$ and $\sum_{j=1}^{B} \mu_{ij} = g_i$. Finally, let $M(f, g)$ represent all transportation plans meeting these requirements, and then the transportation distance (TD) may be defined as the minimzed transportation cost: $TD(g, h) = \inf(\mu \in M(g, h) \sum_{i,j=1}^{N} \mu_{ij}\delta_{ij})$ where $\delta_{ij}$is a taxi cab metric normalized to the embedding dimension between the centers of B_i and B_j. Thus, the TD effectively measures the least amount of work required to ensure equal probability of both series F and B in all B_i boxes. We also note that since the axes of the embedding space have the units of the input data, the distance traveled by shipped probabilities and therefore the TD were computed in units of the input data. The number of intervals used to compute the transportation distance was chosen according to the following formula: $B^{1/m} = \min(8,\ floor((N/5)^{1/m} - 1)$. The ability of the TD to discriminate between some common linear and nonlinear signals is shown in Figure 3.6.

A signal is considered nonlinear if the null hypothesis that there is no significant difference between the nonlinear structure of the signal versus its linear surrogates is rejected. For each test, 199 surrogates were generated and the TD was measured between each original-surrogate pair (OS) and 199 surrogate-surrogate pairs (SS), resulting in two distributions of TD: OS_{TD} and SS_{TD}. The SS_{TD} distribution characterizes the difference between linear surrogates with themselves; if the original signal is invariant with respect to its Fourier phases, the OS_{TD} and SS_{TD} distributions would completely overlap. For a two-tailed hypothesis test of significance level $\alpha = 0.01$, if each of the $(2/\alpha) - 1$ TDs in the OS_{TD} distribution is greater than the TDs in the SS_{TD} distribution (i.e. the OS_{TD} and SS_{TD} distributions are completely non-overlapping), then the null hypothesis is rejected and nonlinearity is inferred. Beyond simply detecting nonlinearity, the degree of nonlinearity (DNL) can be estimated as

$$DNL = median(OS_{TD}) - median(SS_{TD}) \tag{3.4}$$

(e.g. [140, 144]). The DNL provides a measure of the degree of difference between a signal and its linear counterpart. The randomization required by surrogate generation can result in OS_{TD} and SS_{TD} distributions with large standard deviations or outliers, and the median is used as a robust metric of each distribution to limit the influence of such variations.

3.2.5 Nonlinearity in two meandering rivers

The single-threaded, meandering Blue Earth and Watonwan rivers in Minnesota, USA were mapped at two times from aerial photography taken in 1938 and 2008 (Figure 3.6). The Watonwan is a tributary to the Blue Earth, and both rivers flow through a watershed dominated by row crop agriculture (80% coverage). The hydrologic regime shifted substantially around the 1970s due to a combination of anthropogenic and climate changes [145]. Migration rates along both rivers were highly spatially variable between 1938 and 2008, but the Blue Earth migrated an average of 0.26 meters/year compared with the Watonwon's 0.15 meters/year. Over the 70-year period, the Blue Earth underwent 22 cutoffs but grew 1.1 km longer, while 14 cutoffs occurred along the Watonwan and its length was reduced by 2.0 km. The Watonwan widened by 19% and the Blue Earth by 11% over the same period. Planform and migration characteristics for both rivers are given in Table 5.1.

3.3 The evolution of nonlinearity

A meandering river's degree of nonlinearity depends on the evolution of its bends and their removal through cutoff. Understanding the relative importance of bend evolution and removal to the overall DNL requires observations with sufficient temporal resolution to capture these effects. To this end, we analyze the time evolution of the centerline DNL from a simple numerical long-time model of meander migration (Section 3.3.1). Additionally, annual observations of the dynamic, meandering Ucayali River over a 32 year period give insight into the relationship between centerline growth, cutoffs, and DNL in a natural setting (Section 3.3.2).

3.3.1 Detecting nonlinearity in a simulated planform

We used a simple, long-time numerical simulation of a constant-width, migrating, meandering channel with a linear flow field and a linear migration rule [2]. The curvature-driven model, including parameters and boundary conditions, is described in detail and offered as downloadable MATLAB scripts in [146]. The centerline is initially straight with small Gaussian perturbations that evolve into somewhat uniform bends until cutoffs begin. Cutoffs introduce discontinuities in the centerline which are expressed as high-frequency (small wavelength) perturbations in curvature that drive initial rapid bend migration and growth. Over time the planform dynamics through the occurrence of cutoffs give rise to a rich assortment of bend morphologies and lower frequency centerline modulations. The decoupling and linearization of the model's hydro- and sediment dynamics implies that any observed nonlinearities must be either geometric in nature or due to the cutoff process.

We measured the DNL of the evolving curvature signal from the initially-straight centerline for 30,000 years of simulated meander evolution (Figure 4). Initially, the nearly-straight centerline was 800 channel widths (W) and grew to 3200W by year 30,000. Length and sinuosity are closely related since the endpoint positions of the simulated centerline change slowly. Figure 4b shows that in the pre-cutoff state, DNL grew nearly monotonically as the planform developed meander trains populated by individual bends that became larger and more asymmetric. It is interesting to observe that after approximately year 3000, the DNL fluctuated around a steady-state value while the length of the centerline exhibited a slight positive trend that arose from very low-frequency undulations of the centerline occurring within the very long simulated meandering channel and its non-fixed boundaries. Qualitatively, Figure 3.4a shows that sustained elongations or shortenings of centerline length corresponded to increases and decreases of the DNL, though no clear relationship was found between their magnitudes. Changes in the DNL roughly correspond with changes in length once steady-state was achieved for both, but individual cutoff events did not necessarily reduce the total DNL. Between the pre-cutoff and steady-states was a transitional period where the original bends continued to grow while some were simultaneously removed. A maximum DNL was attained in this period before the effects of cutoffs on centerline configuration balanced the effects of bend growth. Overall, the numerical experiment indicated

that cutoffs act to reduce DNL, but the transitional period also shows that for some centerline configurations the effects of cutoff may either be overwhelmed by bend growth or perhaps even amplify the DNL.

3.3.2 Evolving nonlinearity of the Ucayali River

The Ucayali River in Peru is a highly-active, sand bedded, predominantly meandering channel originating in the Andes Mountains and flowing through the Amazon before joining the Amazon River. Using Landsat imagery, annual realizations of Ucayali centerlines were obtained from 1984-2015 (see [147] for processing methods). Over this 32 year period, the 700 km study reach of the Ucayali underwent 26 cutoffs while migrating an average of 51 meters/year. With an average bankfull width of 800 meters, the Ucayali's width-normalized migration rate is an order of magnitude larger than the MN rivers', allowing a faster planform response to flow and sediment pulses and perturbations due to cutoff. The Ucayali widened by 20% between 1984 and 2015.

The Ucayali River underwent significant planform change in the observed 32 year period (Figure 3.5). In particular, in 1997 a major 73 km triple-lobed cutoff near Masisea set off an avalanche of smaller cutoffs and accelerated migration rates both up- and downstream of the Masisea cutoff [147]. The DNL dropped during this time period of post-Masisea adjustment (Figure 3.6), but recovered by 2014 to pre-Masisea-cutoff magnitudes, agreeing with the results from the simulated river suggesting that cutoffs overall tend to decrease the DNL, but the relationship may not hold for each individual cutoff. Conversely, bend growth enhanced the DNL, as observed in Figure 3.6 where periods of reach lengthening generally correspond to periods of increasing DNL. Again, this relationship does not hold across all years; for example, in 2004 the reach shortened by 17 km but the DNL nearly doubled. It is interesting to note that while the DNL eventually returned to pre-Masisea-cutoff magnitudes (by 2014), the reach length remains 10.5% shorter than pre-Masisea-cutoff and is "recovering" at a much slower pace than DNL.

Surprisingly, the DNL only slightly responded to the Masisea cutoff event itself but changed more drastically as subsequent accelerated bend growth and cutoffs occurred, apparently somewhat independently of their size. This result suggests that DNL is not strictly related to the magnitude of bend removal through cutoff. Because DNL measures

the complete centerline structure, the location of the cutoff may also play an important primary role, along with the subsequent bend growth. Overall, the covariation of channel length and DNL suggests that cutoffs and bend growth play a primary role in the DNL of a migrating meandering river, but the magnitude of DNL in response to individual cutoffs or bend growth is also modulated by the resulting arrangement of bends.

3.4 Identifying sources of nonlinearity

In the absence of cutoffs, the DNL in the simulated meandering river arises solely from the geometric nonlinearity of Equation 3.1. Although cutoffs weaken the effect of this geometric nonlinearity on DNL, they also introduce a planform dynamic that may itself impose nonlinearity onto the centerline structure. The normalized wavelet power spectrum in Figure 3.6 shows that cutoffs "spread" the spectral energy of the centerline curvatures by introducing new scales to the curvature series. Immediately before cutoffs, the *developed bend scales* (i.e. the fully developed individual bends of the t=450 yr centerline in Figure 3.4) dominated the spectrum. Most of the energy of the precutoff centerline curvatures was contained by scales near the average length of a developed meander (40 channel widths). After cutoffs occurred, the centerline energy spread across a wider range of scales. Cutoffs imposed sharp perturbations into the curvature signal at *birth scales* smaller than 8.6 channel widths which eventually grew to developed bends before being cut off again. Cutoffs also resulted in planform configurations that allowed the development of *superdeveloped scales* (scales larger than 68 channel widths) when bends grew larger than the developed bend scale before they were removed.

In order to assess whether the scales introduced by cutoff also contribute to the DNL, a localized space-frequency analysis of the curvatures series is needed that decomposes it into a local (e.g. wavelet) rather than a global (e.g. Fourier) basis (Section 3.4.1). This analysis is performed on precutoff and postcutoff centerlines to determine whether cutoffs are also a source of nonlinearity (Section 3.4.2).

3.4.1 Linearizing surrogates partialy with Gradual Wavelet Reconstruction

Fourier-based linearization provides a way to measure a signal's degree of nonlinearity relative to its fully linearized counterpart, but it does not give insight into which features of the signal (i.e. scales and/or locations) contribute most to its nonlinearity. For that, a localized space-frequency analysis is needed that decomposes the signal into a local (e.g. wavelet) rather than a global (e.g. Fourier) basis. Gradual wavelet reconstruction (GWR) was introduced by [148] as a surrogate generation method that allows partial linearization of the original signal. To perform GWR, a signal was decomposed with a Maximal Overlap Discrete Wavelet Transform (MODWT) [149], resulting in $J \times K$ coefficients $w_{j,k}$, where J is the number of scales of decomposition and K is the length of the signal. The MODWT is advantageous to use for GWR primarily because it allows the preservation of the power spectrum and autocorrelation function at each scale while providing K coefficients at each level of decomposition, but see [135] for a discussion of its other desirable properties. The total energy E of the signal is the sum of the squared wavelet coefficients:

$$E = \sum_{j=1}^{J} \sum_{k=1}^{K} w_{j,k}^2 \tag{3.5}$$

The desired fraction of wavelet energy to retain in the surrogate was selected as ρ ($0 < \rho < 1$). The squared coefficients were sorted from largest to smallest, and the largest-energy coefficients accounting for ρE of the total energy were fixed in place. The IAAFT was applied to each scale of the transform, shuffling the non-fixed wavelet coefficients while preserving the wavelet spectrum. The MODWT was finally inverted to recover a surrogate signal that fixed in place a ρ^{th} fraction of the energy of the original signal.

The systematic variation of ρ allows identification of the wavelet coefficients most important to the nonlinear structure of the signal. Consider generating a surrogate for $\rho = 1$. In this trivial case, all the energy of the original signal is fixed in place and the surrogate is therefore no different than the original signal (so the DNL is necessarily zero). Now we proceed to generate surrogates for incrementally reduced values of ρ; we used increments of 0.1 herein. Each time ρ is reduced, additional wavelet coefficients are randomized. Therefore changes in ρ correspond to specific coefficients in the wavelet domain which provide

scale and/or location information. By measuring the DNL of surrogates generated by incrementally decreasing ρ, large changes in DNL with respect to ρ can then be attributed to the specific wavelet coefficients (and hence scales) that were un-fixed for that ρ increment, thus identifying the scales and locations that contribute disproportionately to the signal's nonlinear structure. For $\rho = 0$, all coefficients are randomized to create a completely linearized surrogate, and in these cases the Fourier-based surrogate generation method was used.

3.4.2 Contribution of cutoffs to nonlinearity

GWR was applied to two curvature signals from the simulated centerline: one immediately before cutoffs began and the other once a steady-state sinuosity had been achieved through the balance of bend growths and cutoffs (see Figure 3.4). The DNL was measured for both centerlines as ρ was varied in constant increments of 0.1, and the resulting DNL(ρ) curves in Figure 3.6 agree with the results of Figure 3.4 insofar as the total DNL was higher for centerlines immediately preceding cutoff than those during the postcutoff state. Indeed, total DNL (i.e. $DNL(\rho = 0)$) is nearly twice as high for the precutoff centerline.

The slopes of the DNL(ρ) curves in Figure 3.6 indicate which ρ increments, and therefore which wavelet coefficients, are most important in accounting for total DNL. These slopes can be written as $d(DNL)_i/d\rho_i$ for the i^{th} increment of ρ, where $d\rho = 0.1$ for all i. In other words, for each incremental reduction of ρ, 10% less of the total wavelet energy from the original signal is fixed in place in the surrogates. The three steepest slopes (shown by bold line segments) correspond to the three largest $d(DNL)_i$ increments, i.e. those that contributed the most to the total DNL. Recall that total DNL is measured against surrogates that have $\rho = 0$. Total DNL may also be written as the sum of the contributing increments: $total\ DNL = DNL(\rho = 0) = \sum_{i=1}^{N} d(DNL)_i$ for $N = 10$ increments. The wavelet energy accounted for by the three bold segments of each centerline accounts for 30% of the total energy, while the DNL contributed by the three bold segments is $\sum_{i=4,8,9} d(DNL)_i / \sum_{i=1}^{N} d(DNL)_i = 63.4\%$ of the total DNL for the precutoff and $\sum_{i=1,8,10} d(DNL)_i / \sum_{i=1}^{N} d(DNL)_i = 62.3\%$ for the postcutoff centerlines. The coefficients from the three largest contributing increments to DNL were summed across all locations in the wavelet transform to identify those scales of the original signal that were

most important to the overall nonlinearity. In Figure 3.6, these scales are shown on top of the wavelet power spectrum for the entire signal. For the precutoff centerline, scales near the emergent bend scale were not only most present in the total energy, but they also accounted for the largest fraction of DNL. Smaller scales contributed less to overall DNL, but were more important as a fraction of the total energy at each scale. For the postcutoff centerline, the source of DNL was spread across a wider range of scales, including those that were not present in the precutoff centerline. Particularly, new contributions came from birth and superdeveloped scales while the developed bend scales became less important to the total DNL.

3.5 Discussion

3.5.1 Sources of nonlinearity

Measuring DNL in evolving real and simulated rivers and synthetically-generated centerlines provides insight into the features contributing to nonlinearity. Even for linearized and decoupled treatments of hydro- and sediment dynamics, simulated meander morphodynamics include the geometric nonlinearity of Equation (3.1). The simulated river before cutoff showed that planform nonlinearity grows as bends enlarge and skew. The scales that contribute to nonlinearity identified through a GWR analysis of pre- and postcutoff centerlines suggest that cutoffs also introduce nonlinearity into the planform morphology. Cutoffs "spread" the spectral energy of the curvature signal into a wider range of scales, and these new scales were found to be primary contributors to the total DNL. Even though plenty of energy was contained at the emergent bend scale after cutoffs occur (79% of total energy in precutoff versus 64% in postcutoff), the relative contribution of these scales to DNL was much smaller.

Although cutoffs serve as a source of nonlinearity, their overall effect is a reduction of the DNL through the removal of bends and consequent rearrangement of the planform. Results from the simulated river showed that the maximum DNL was achieved when cutoffs had been active for a short time, and that the river's steady state DNL had a lower magnitude than before cutoffs began. Two Minnesota rivers and the Ucayali River in Peru also showed that cutoffs generally act to reduce DNL while bend growth promotes DNL, despite

the additional nonlinearity that cutoffs impose. However, the same results also indicate that predicting how an individual cutoff event affects overall centerline nonlinearity is not straightforward as the size of the cutoff could not be simply related to the corresponding drop in DNL.

Previously, cutoffs had been argued to reduce the overall nonlinearity in meandering river spatial structure through the removal of bends that had sufficient time to express inherent deterministic nonlinearities [52, 58]. Our results suggest a more subtle reasoning; the degree to which cutoffs also destroy planform nonlinearity depends on the position of the removed bend(s) relative to its neighbors in the meander train. In our simulation, cutoffs reduced the amount of energy present at the emergent bend scales by only 10%, but the contributions from these scales to DNL were reduced 61% after cutoffs occurred. In other words, although the emergent bend scales were still present in the meander train after cutoffs were active, they contributed significantly less to its nonlinear planform structure. This suggests that cutoffs break the nonlinear pattern of bend arrangement within a meander train expressed through an altered topological structure in the embedding space such that the attractor's nonlinearity is reduced. The difficulty in determining the degree to which a particular cutoff will affect the DNL can also be attributed to the simultaneous evolution of the rest of the meander train. Following a major, triple-bend cutoff, the Ucayali River showed that the planform evolution of the entire meander train responded rapidly enough to return to pre-cutoff DNL levels although the river's length (or sinuosity) remained substantially lower than before the cutoff.

3.5.2 Implications for nonlinearity in meandering rivers

The relationship between process and form is at the heart of many problems in geomorphology and holds particular intrigue in meandering rivers (e.g. [150, 151, 152, 146]. Previous studies have implicitly assumed that the spatial structure of meandering rivers represented the local formative dynamics. In this work, we explicitly assumed this link between form and process by taking the spatial structure of a meandering channel as a "measurement" on the complete dynamic system that governs meander evolution. While this notion may seem obvious, it is possible that this spatial "measurement" linearizes the driving nonlinear dynamics. Furthermore, the nonlinearities in the deterministic dynamics that drive

meander morphodynamics had yet been curiously difficult to detect in meander morphology. The discovery of planform nonlinearities presented in this paper (Figures 3.6 and 3.4, specifically) at least partially justifies the assumption that dynamic nonlinearities are encoded in spatial structure and should encourage further efforts to link meander process and form from spatial signals of meander planforms. This discovery also shows that meandering river spatial structures fulfill the necessary but not sufficient condition of nonlinearity required by the use of phase-space models (e.g. chaos) or certain conceptual models (e.g. self-organized criticality) to describe meander morphodynamics. Phase-space models have been widely applied to many physical systems but have seen only limited application to meandering river morphodynamics. Our results show that centerline reconstruction in an appropriate embedding space reflects the nonlinearity of the system dynamics–an essential requirement to building phase-space models that exploit nonlinear structure to describe and predict meander planform migration.

3.5.3 Comparing DNL between rivers

Like sinuosity (see [153, 154, 155], the DNL also exhibits a degree of scale-dependence, as the properties of the analyzed curvature signal are dependent on both the sampling density of the centerline and smoothing [88, 100]. Since the TD is measured in units of curvature, a consistent basis for obtaining comparable curvatures derived from different data sources and rivers of various scales is a prerequisite for comparing DNL between different rivers. The problem of scale-dependence of sampling and smoothing of centerlines on curvature signals is beyond the scope of this work and requires further investigation, especially considering the widespread use of curvature signals to characterize aspects of meandering river planforms. We chose not to normalize DNL measures by a characteristic reach scale (e.g. channel width or dominant wavelength) for two reasons. First, because meander train planforms are multi-scale features, selecting a single characteristic value may bias the normalized DNL depending on the nature of the planform nonlinearity, although promising recent research has attempted to grapple with the multi-scale structure of meandering rivers using wavelets [131, 156, 157]. Second, the normalization constants may not actually be constant, as evidenced by the nearly 20% increase in width for the Blue

Earth and Ucayali rivers over relatively short time scales. The decision not to normalize means that DNL values measured for different rivers are not yet directly comparable without further investigation of sampling, smoothing, and scale effects on spatial signals. However, the observed presence (or absence) of nonlinearity is unaffected by normalization, and changes in DNL in time for the same river are comparable since biases due to sampling and smoothing parameterizations are minimal.

3.6 Conclusions and Future Directions

The results herein confirmed that the spatial structure of meandering river planforms are indeed nonlinear by analyzing three real rivers and one simulated. Spatial nonlinearity arises from the local nonlinear deterministic dynamics governing meander evolution and the occurrence of cutoffs, but the overall degree of nonlinearity is generally attenuated through cutoffs. As previously proposed, cutoffs destroy nonlinearity by removing fully-developed nonlinear bends, but the degree of nonlinearity also depends on the relative positioning of bends within a meander train. The relative importance of these effects remains unclear, but further synthetically-generated planforms and meander simulations will help clarify the effects of cutoffs on spatial nonlinearities. The removal of developed bends appears to play the primary role in a reduction of a reach's spatial nonlinearity, while the alteration of bend arrangements within the meander train seems to play a lesser but significant role.

Our model featured linearized flow and sediment dynamics and a linear bank erosion law. While this model was appropriate for isolating the effects of cutoffs and the inherent geometric nonlinearity of meander evolution on spatial nonlinearity, detailed nonlinear process models should be implemented to quantify the effects of local, nonlinear hydro- and sediment dynamics. Such modeling efforts could determine if different process nonlinearities leave unique signatures in the spatial structure, and the DNL could then potentially identify particular processes from observations of planform morphology alone. The degree to which spatial nonlinearities measured by DNL in real rivers are indeed measurements of underlying process rather than reflecting heterogeneity and nonstationarity in environmental conditions remains unknown. Heterogeneity in floodplain resistance (e.g. [72, 73, 61]) or sediment size (e.g. [158]) can introduce complexity into planforms that may be difficult

to distinguish from dynamically-driven complexity. Nonlinearities in natural meandering rivers may also be subject to a degree of signal shredding [120], nonstationary dynamics, or human, climatic, or geologic [159] forcings. Future research will aim to untangle the role of each of these using numerical modeling and observations of natural rivers, and further work is also underway to develop consistent sampling, discretization, and normalization techniques so that DNL may be compared across rivers of different scales and mapped by different methods.

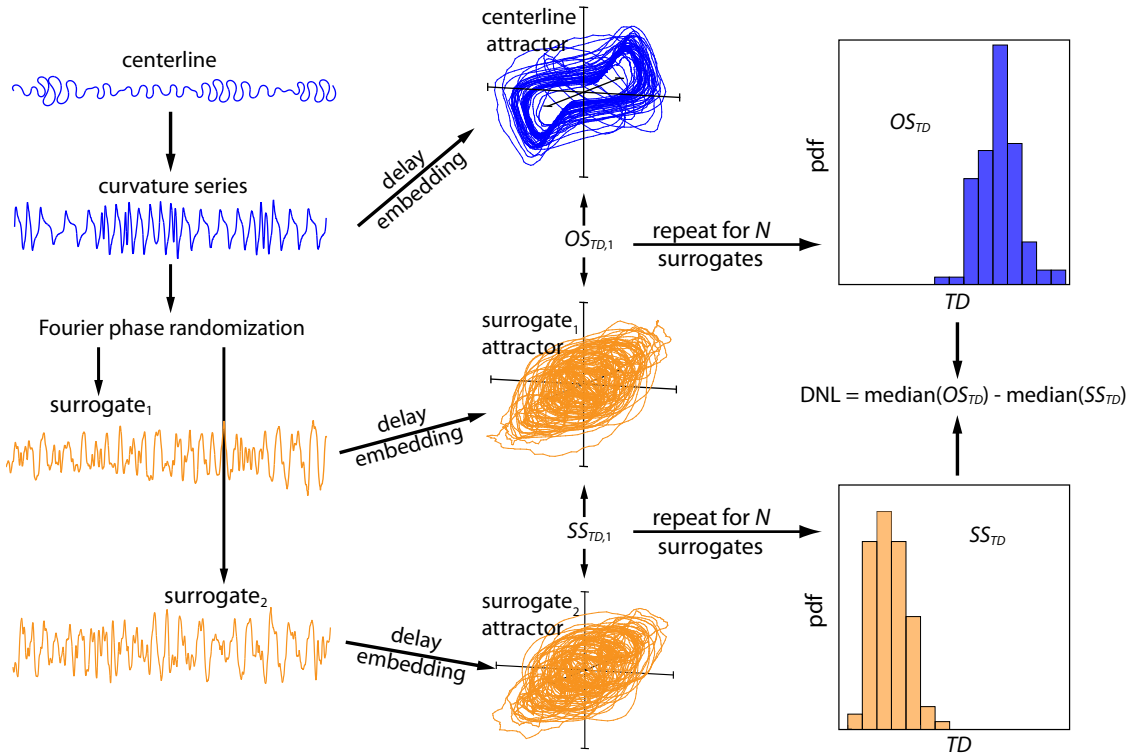

Figure 3.1: The procedure for computing the degree of nonlinearity (DNL) is shown. First, the curvature series is computed from a centerline. N surrogates of the curvature series are generated (only two are shown) by randomizing their Fourier phases. The curvature series and its surrogate are embedded in phase space and the difference between attractors ($OS_{TD,1}$) is measured with the transportation distance (TD). This procedure is repeated N times, resulting in the OS_{TD} distribution. The same procedure is used to generate the SS_{TD} distribution except that surrogate-surrogate pairs are compared in the embedding space. The DNL is then estimated as the distance between the medians of the SS_{TD} and OS_{TD} distributions.

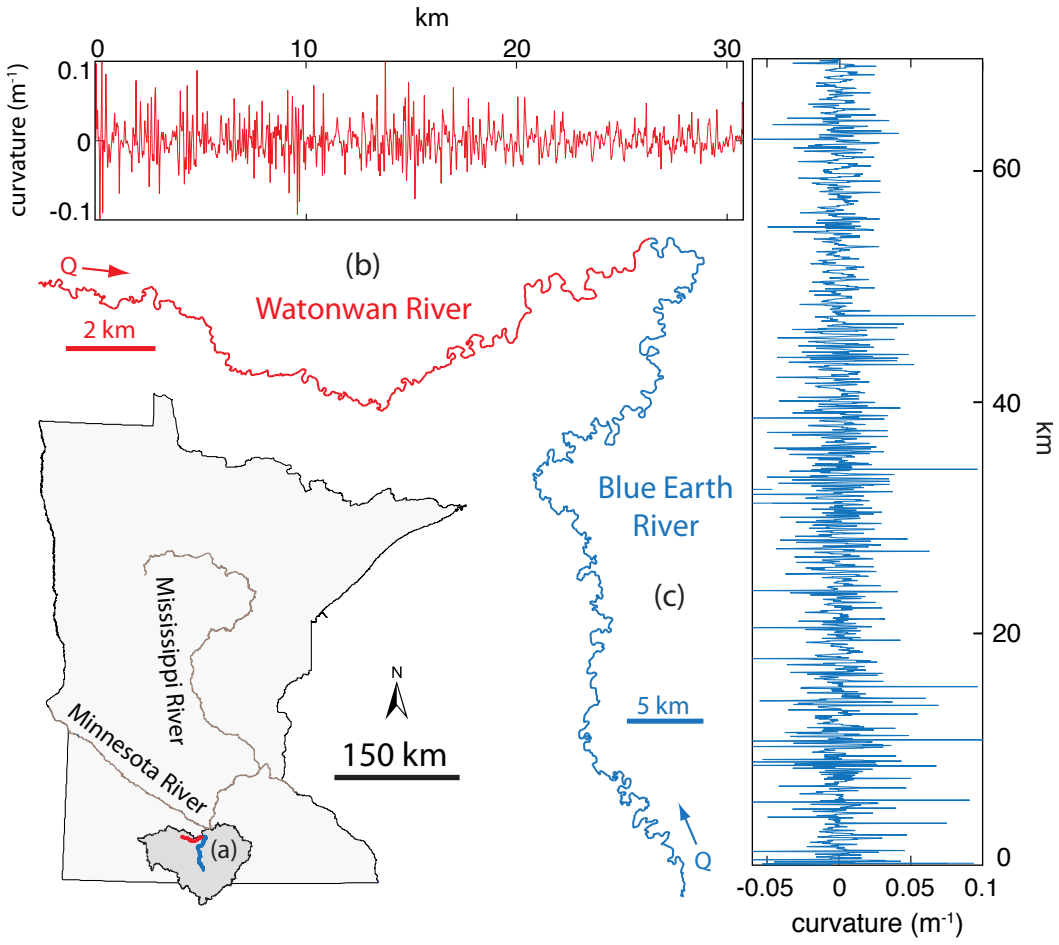

Figure 3.2: The locations of the Blue Earth (in red) and Watonwan (in blue) rivers are shown within the Greater Blue Earth Basin (a) in Minnesota, USA. In (c) and (d), the 2008 Watonwan River and 2008 Blue Earth planforms are shown in more detail along with their curvature series. As shown, both rivers flow to the same location but note the different scales for each.

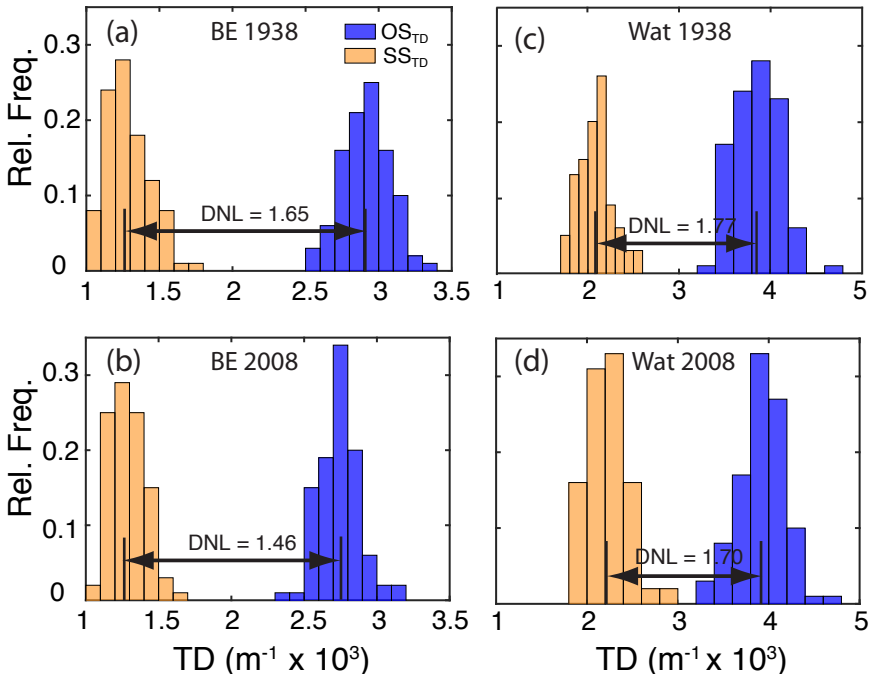

Figure 3.3: The distributions of transportation distances (TDs) between the original centerline curvature series and their surrogates (OS_{TD}) and between surrogates and surrogates (SS_{TD}) are shown for the Blue Earth River, 1938 (a) and 2008 (b) and the Watonwan River, 1938 (c) and 2008 (d). The degree of nonlinearity (DNL) is shown as the distance between the medians (vertical black lines) of the OS_{TD} and SS_{TD} distributions. Units of DNL are the same as TD ($m^{-1} \times 10^3$).

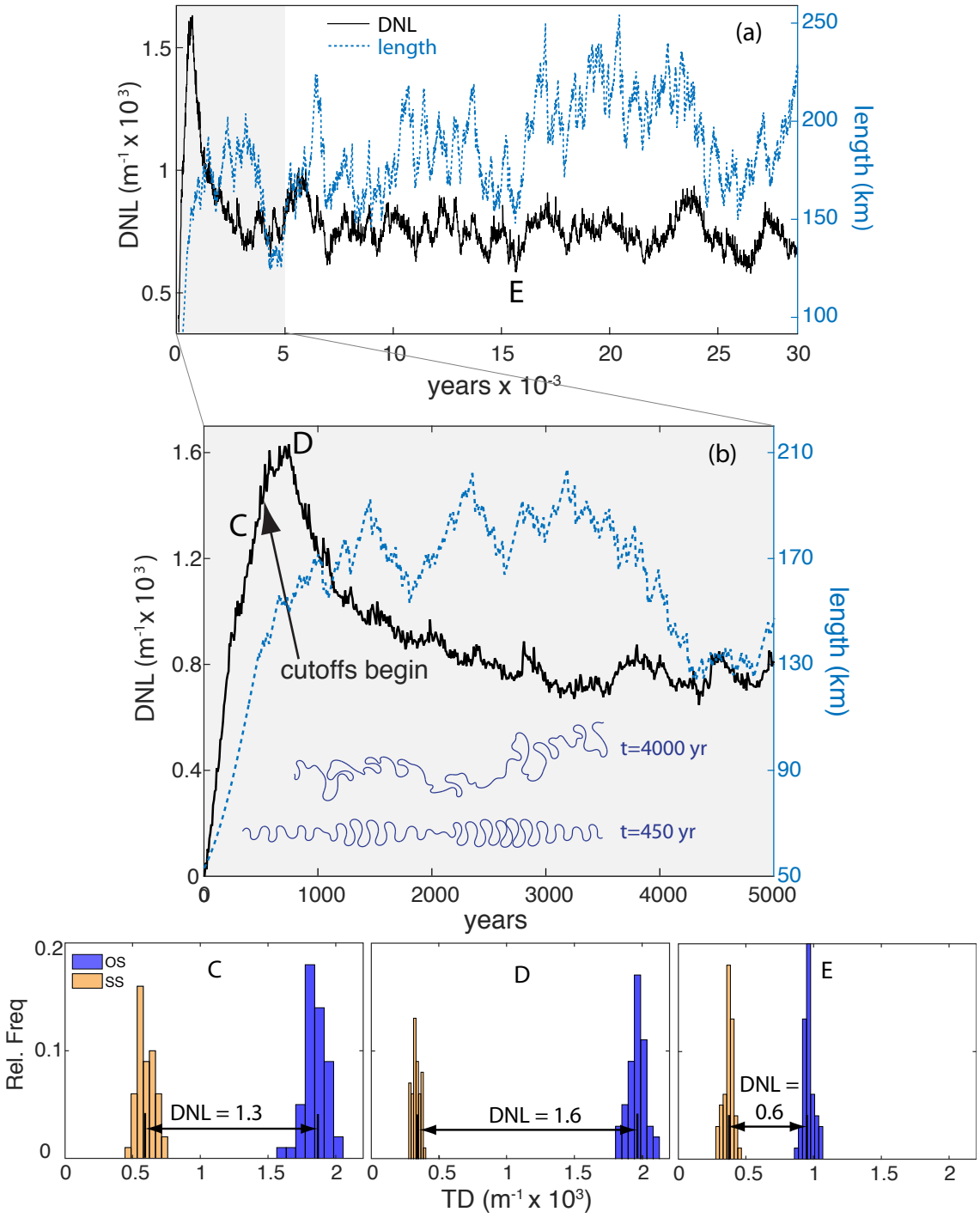

Figure 3.4: (Caption next page.)

Figure 3.4: (Figure previous page.) The evolution of the degree of nonlinearity (solid black line) is shown for 30,000 years of the simulated centerline evolution, and the length of the centerline is shown as a dotted blue line in (a). DNL reaches a steady state near year 2900, and the length does so around year 2200. A closer view of the initial evolution and the transitional period is shown in (b). An arrow denotes the year (480) when cutoffs began. A pre-cutoff centerline from year 450 (lower) and post-cutoff centerline from year 4000 (upper) are shown. Flow is from left to right. The OS_{TD} and SS_{TD} distributions are shown at the times marked C, D, and E (year 15,700) to verify that significant nonlinearity is present in precutoff, transitional, and postcutoff conditions. D represents the maximum DNL, while E shows a local minimum of the DNL. DNL has the same units as TD ($m^{-1} \times 10^3$).

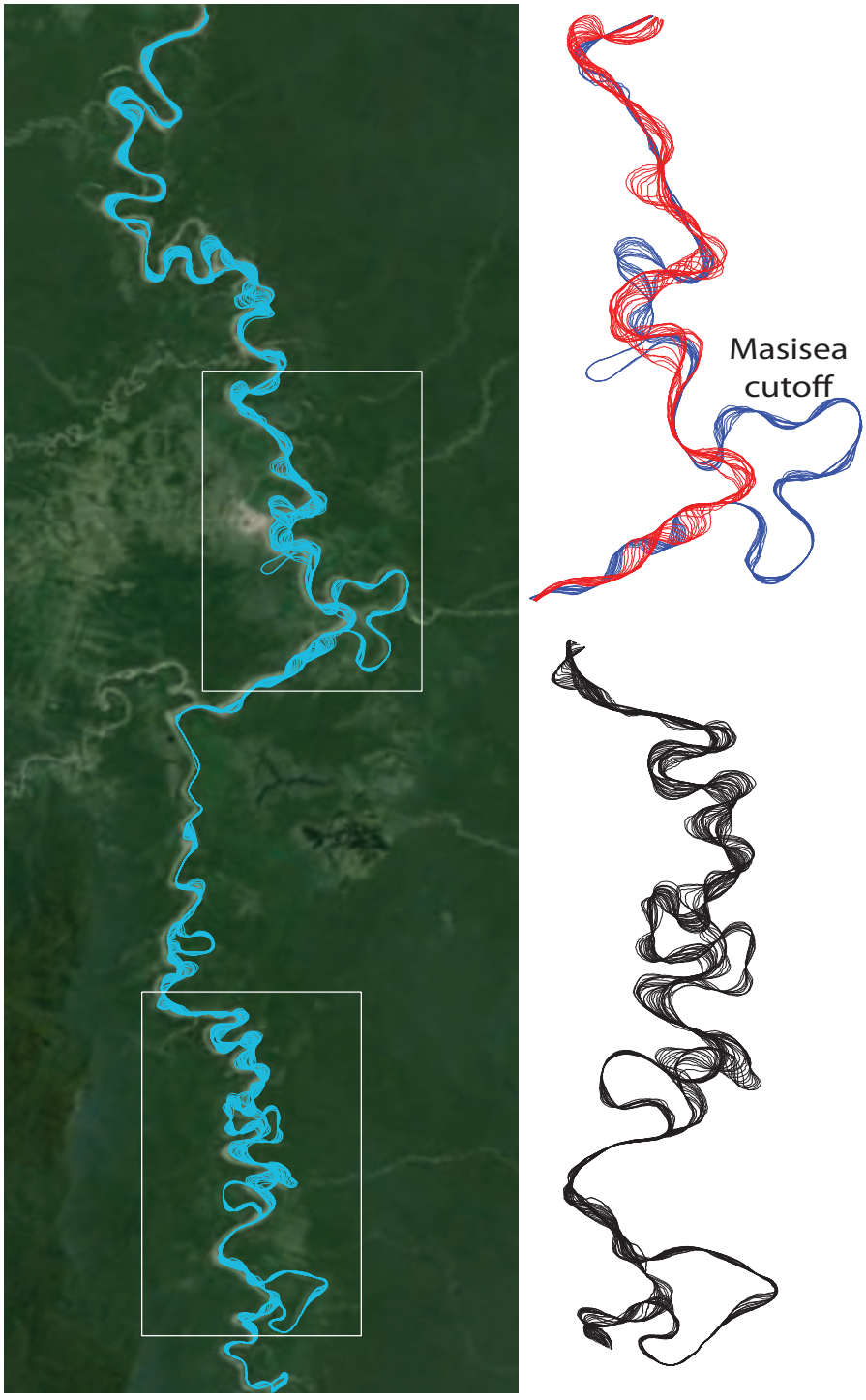

Figure 3.5: (Caption next page.)

Figure 3.5: (Figure previous page.) The reach of the Ucayali River, Peru analyzed in this study is shown. (a) Annual centerlines from 1984-2015 are plotted atop aerial imagery from 2013. Details of centerline extraction are given in [130]. (b) The effects of the 1997 cutoff of the triple-lobed, 73 km bend on channel morphodynamics are shown at a closer view. Pre-Masisea-cutoff centerlines are blue; postcutoff red. (c) Morphodynamics for an active southern portion of the reach are shown in more detail. Aerial imagery from Google Earth.

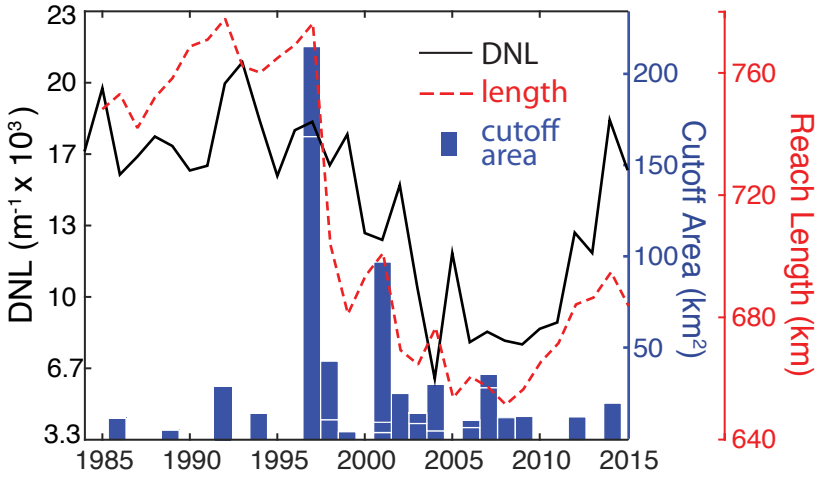

Figure 3.6: Degree of nonlinearity is shown in black for annual realizations of the actively migrating Ucayali River. Blue bars show the area of cutoffs removed between years. Multiple cutoffs that occurred in the same year are separated by a small white gap. The length of the studied reach is shown in red. Length may also be interpreted as sinuosity since the locations of the reach endpoints do not change through time. Length was not computed for 1984 due to inability to fully resolve because of poor satellite imagery that year.

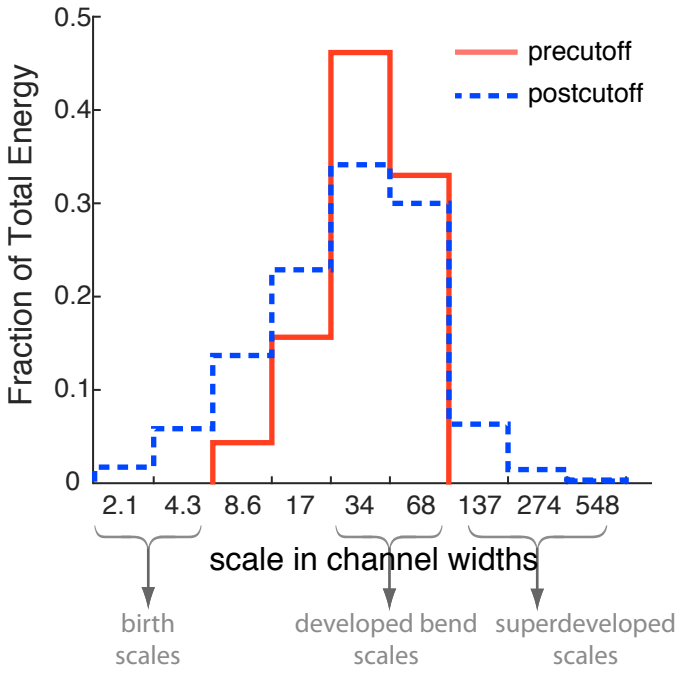

Figure 3.7: A normalized wavelet power spectrum for the precutoff (red) and postcutoff (blue) centerline curvatures are shown. Each distribution represents the summation of wavelet coefficients across all locations normalized by the total energy. Three scale ranges are defined as *birth*, *developed*, and *superdeveloped*.

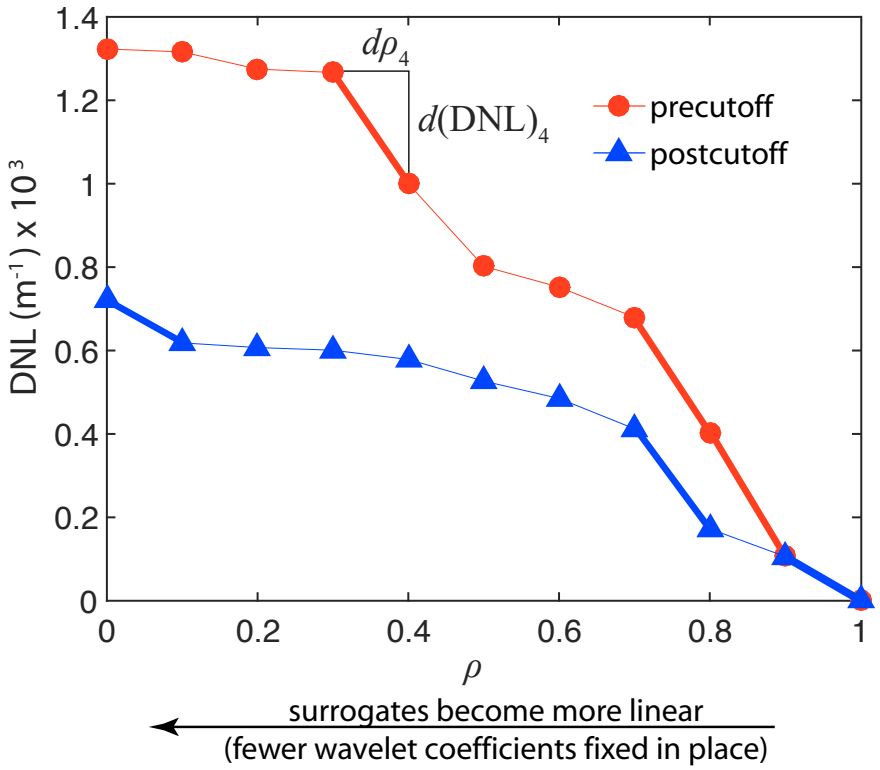

Figure 3.8: The degree of nonlinearity (DNL) is shown as a function of ρ for precutoff (red circles) and postcutoff (blue triangles) centerline curvatures. With decreasing ρ, fewer original wavelet coefficients are fixed in place resulting in more linear surrogates. The trends of these lines indicate that as surrogates become more linear, the difference between the original signal and the surrogates (i.e. DNL) increases. For both the precutoff and postcutoff curvatures, three bold line segments highlight the three largest increments of ρ that contributed most to the total DNL. The definitions of $d\rho_i$ and $d(DNL)_i$ are shown for i = 4. Total DNL corresponds to $\rho = 0$.

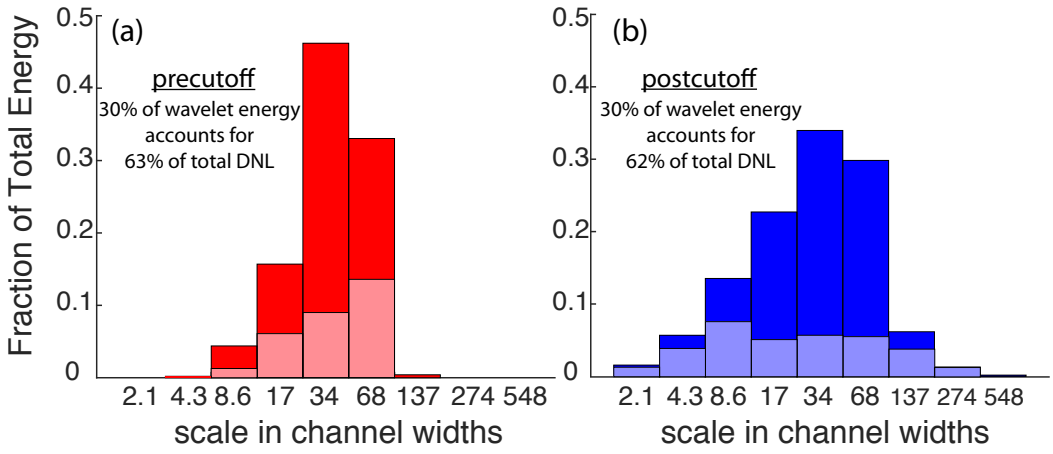

Figure 3.9: The normalized wavelet power spectra are shown for precutoff (a, dark bars) and postcutoff (b, dark bars) centerlines, as in Figure 3.6. The lighter bars in (a) and (b) represent the most energetic 30% of the total wavelet energy and account for 63% (precutoff) and 62% (postcutoff) of the total DNL. Total DNL is much higher in precutoff (1.3 km^{-1}) than postcutoff (0.72 km^{-1}) centerlines. The lighter bars represent the scales that contribute disproportionately more to the total DNL and correspond to the summation of the scales of the bold line segments in Figure 3.6. The lighter colors represent 30% of the total energy of the original centerline signals, but account for 63% and 62% of the total DNL in the precutoff and postcutoff centerlines, respectively.

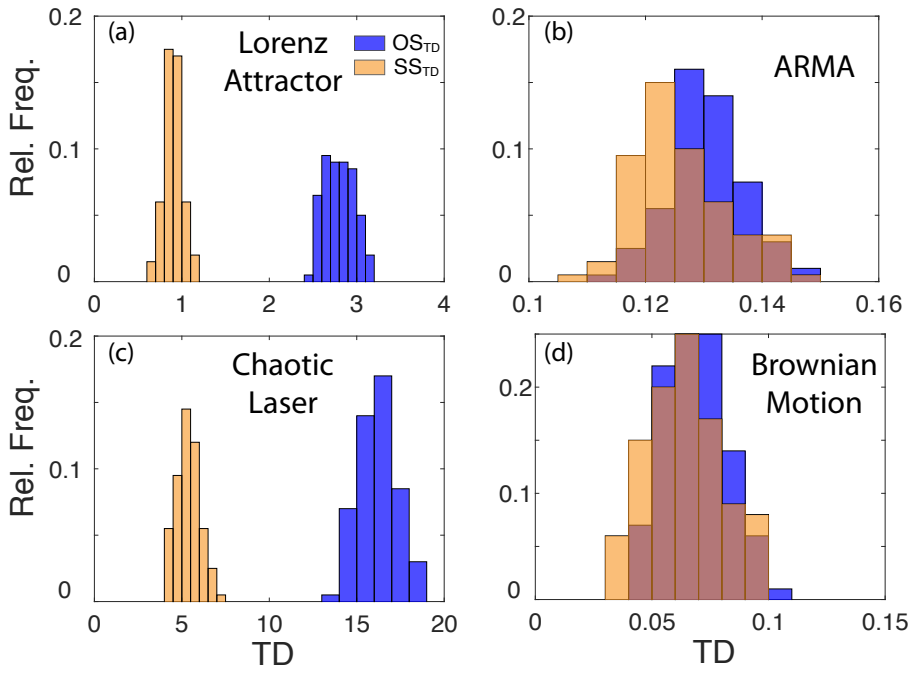

Figure 3.10: Distributions are shown for surrogate-surrogate (SS_{TD}, in orange) TDs and original-surrogate (OS_{TD}, in blue) TDs for four series: (a) the Lorenz "butterfly" attractor, (b) a linear ARMA(1,1) series [1], (c) time series from a chaotic laser provided as part of the Santa Fe Institute competition series, and (d) a linear random-walk process. The degree of nonlinearity (DNL) is measured as the difference between the medians of the OS and SS distributions.

River	width(m)		length (km)		sinuosity		slope	M_r^a (m/yr)	cutoffs	$A_{cutoff}/A_{river}{}^b$ (%)
	1938	2008	1938	2008	1938	2008				
Watonwan	24.5	29.1	61.3	59.3	2.28	2.21	5.2×10^{-4}	0.15	14	15.8
Blue Earth	45.4	50.4	165.5	166.6	2.94	2.96	5.2×10^{-4}	0.26	22	8.9

Table 3.1: ^{a}Migration rate (M_r) is computed as $A_{mig}/length/69\,yr$, where A_{mig} is the area the centerline traversed between two realizations in time. $^bA_{cutoff}$ is the area encompassed by a cut off portion of centerline, and A_{river} is the planform area of the channel.

Chapter 4

The secret lives of migrating meanders of the Ucayali River

Quantifying planform changes of large and actively migrating rivers, such as those in the tropical Amazon, with high temporal frequency is essential for advancing river morphodynamic theory, identifying controls on migration, and understanding the roles of climatic and human influences on planform adjustments and flooding potential. This paper presents the challenges of quantifying planform changes over large spatial domains using Landsat imagery and introduces a set of efficient methods to map and measure spatial and temporal planform changes including channel widths, areas and rates of centerline and bankline migration, erosion and accretion, and cutoffs. The techniques are assembled in a comprehensive Matlab toolbox called RivMAP (River Morphodynamics from Analysis of Planforms), which is discussed extensively herein. As a proof-of-concept, the RivMAP toolbox is applied to over 1,300 km of the actively-migrating and predominately meandering Ucayali River in Peru. Landsat 5 and 7 images collected from 1985-2015 are classified with a supervised classifier, and annual composite images are created that are shown to resolve bankfull channel and bar morphologies. Hydraulically-connected and single-thread channel masks obtained from the composite images are then used to quantify planform changes in river width, migration rates, and accretion/erosion rates and map and measure 57 cutoffs throughout the reach. The uncertainty of the analysis is estimated by quantifying planform changes for three abandoned, pseudo-stationary bends. Multiscale spatial

and temporal variability around multi-decadal trends in migration rates along the Ucayali River suggests that climate, proximity to tributaries, and cutoffs may act as controls on meander migration.

4.1 Introduction

Efforts to map and measure meander migration have resulted in fruitful insights into the dynamics of these fascinating fluvial forms. However, the difficulty of observing multidecadal river migrations at high temporal and spatial resolutions has hampered efforts to fully resolve natural planform dynamics [22]. Observations made over longer periods (decades to centuries) are often compiled from various sources such as historic maps, surveys, and aerial photographs that do not capture intermediate planform changes [29, 160, 30] due to nonstationary flow regimes [161, 162] , individual floods [163, 31], cutoffs [164, 165, 166], or human activities [167, 168, 169], among others. On the other hand, studies that resolve detailed migration dynamics at event-scale frequencies from aerial photographs are often constrained to significantly shorter durations than the inception-to-cutoff time of a typical meander bend (e.g. [170]). Highly-temporally resolved meander dynamics have been estimated over longer durations from scroll bars [171], point bar surfaces [115], and tree rings [172], but these studies were not spatially continuous over distances larger than a few meander bends. Many researchers have turned to numerical modelling to simulate river planform and floodplain development over long durations and large spatial domains with high temporal frequency [72, 54, 173, 33, 146]. However, validation of such long-time models has received less attention, due partly to the limited availability of observations [97].

Satellite imagery offers the potential to map spatially-continuous planform changes over large domains and with high temporal resolution. The Thematic Mapper (TM) sensors aboard Landsat satellites have collected worldwide imagery at 30m resolution at least every 16 days since the launch of Landsat 5 (L5) in 1984. In terms of observing natural fluvial planform change, 30m Landsat data overcome the obstacles of poor temporal resolution and limited spatial coverage, but its 32-year record is significantly shorter than the inception-to-cutoff timescale of most meandering rivers. Nevertheless, a growing number of studies have leveraged Landsat imagery to map and measure planform changes of major rivers

(e.g. [174, 175, 176]). Rivers flowing through the tropical Amazon region have been of particular interest [177, 178, 179] partly due to their rapidly changing planforms. For example, full lifecycles (i.e. inception to cutoff) for a number of smaller meander bends in the Amazon were captured within the growing 32 year window of Landsat imagery. Most studies of river changes resolved the planforms at time intervals longer than two years, although [180] analyzed two anabranching bends using annual time steps, as did [181].

This work investigates the feasibility of quantifying annual bankfull planform dynamics from Landsat imagery for over 1,300 km of the Ucayali River in Peru from 1985-2015. To this end, a suite of modules written in Matlab was developed to quantify channel planforms from aerial or satellite imagery and compiled into a Matlab toolbox called RivMAP: River Morphodynamics from Analysis of Planforms. A variety of toolsets and programs are already available for determining planform channel characteristics from remotely sensed imagery and/or planform maps, including channel width (e.g. [182]), planform geometry (e.g. [183, 184]), and planform change (e.g. [185, 186]). RivMAP differs from these by providing a comprehensive toolbox to both characterize river planforms and quantify their changes through time using centerline-based and mask-differencing techniques written as easily-modifiable and intuitive Matlab functions. The RivMAP toolbox was developed to make possible the analysis of many large images (on the order of multiple Landsat scenes) without supercomputing resources or hand-delineations by exploiting the efficient image processing capabilities and built-in Matlab functions.

This paper is organized as follows: Section 4.2 describes the study reach of the Ucayali River. Section 4.3 details the process of acquiring and classifying Landsat data. Section 4.4 outlines the procedure for creating annual bankfull composite images from individual Landsat images. Section 4.5 describes a technique to create channel masks from composite images. Section 4.6 explains the functions for quantifying planform characteristics and changes included in the RivMAP toolbox. Section 4.7 shows the multiscale spatial and temporal variability of planform changes along the Ucayali River quantified via RivMAP and presents an uncertainty estimation. Section 4.8 concludes with an overview of the analysis and potential applications of RivMAP toward developing mechanistic understanding and numerical modeling of river morphodynamics.

4.2 Study Area

The Ucayali River flows south-to-north through Peruvian rainforest along the southeastern base of the Andes Mountains before joining the Marañon River to become the Amazon River about 100 kilometers south of Iquitos, Peru. Although the Ucayali River begins near Cusco, Peru in the Andes Mountains, its remarkably active migration begins near the city of Atalaya at its confluence with the Tambo River. From its headwaters in the Arequipa region of Peru to its confluence with the Marañon River, the Ucayali River stretches approximately 2,670 km, but this study focuses only on the final 1,300 km between the confluences with the Tambo and Marañon Rivers (Figure 4.2). The study reach of the Ucayali River exhibits some braiding and anastomosing but features a predominately single-thread, meandering planform with many bends that contain secondary chute channels.

The Ucayali River is an extraordinarily dynamic river featuring abundant cutoffs and point-bar developments. Oxbow lakes and scroll bars pepper its floodplain. An annual average migration rate of 36 m/yr was recently reported [178], but migration rates exceeding 750 m/yr were observed locally along some bends. The Ucayali's extraordinary activity is driven, in part, by large sediment loads [178] supplied by four major tributaries draining the westerly Andes Mountains (56% of its catchment is Andean) and sediment and flow contributions from nearly a dozen smaller tributaries from the easterly Amazon Rainforest. This study found bankfull widths ranging from 400 to over 1,500 m with an average of about 800 m, and the average depth was reported as 10 m though scour holes are sometimes 10 m deeper than the average bed elevation [187]. Mean annual flows at the confluence with the Amazon River have been reported to range from around 9,500 m^3/s [188] to 13,500 m^3/s [189], but discharge is cyclic with a strong seasonal dependence [190]. Flow and sediment (D_{50} = 0.25 mm) are transported along slopes on the order of 10^{-4} [Ettmer and Alvarado-Ancieta, 2010]. The river is relatively unimpacted by anthropogenic activity, although at least one major cutoff event was unintentionally initiated by locals near the Masisea community [191, 192]. The Ucayali River is vital to the livelihoods of nearly 500 local communities [193], providing economic and transportation benefits to millions of Peruvians [192].

For this study, the Ucayali River was divided into four boxes (R3-R6, Figure 4.2C) in order to reduce the computational demand of downloading and processing imagery. Box

boundaries were drawn to intersect the river at reaches of minimal planform change. Eight Landsat scenes contributed imagery to resolve the river within the boxes. The Ucayali River contains a major avulsion in R3 (Figure 4.2,R3) where the southern reach is approximately twice the width of its northern counterpart. Both avulsions were retained in the analysis, although reachwide analyses only include the southern branch.

4.3 Classifying Landsat imagery

Continuous, worldwide satellite images at 30 meter resolution were first collected by NASA's Landsat 5 (L5) beginning in 1984. L5 provided complete satellite images of Earth every 16 days. In 1999 Landsat 7 (L7) was launched and began recording imagery every 16 days. In conjunction, L5 and L7 provided complete global coverage every eight days, although many views of the Earth's surface were obscured by clouds. On May 31, 2003, the scan line corrector (SLC) aboard L7 failed, resulting in stripes of missing data across all its succeeding scenes (see boxes 1-4 in Figure 4.4). L5 continued collecting imagery until 2013. This study used publicly-available Landsat data from L5 and L7 spanning 1984-2015, although insufficient imagery was available to fully resolve the Ucayali River in 1984. In 2013 Landsat 8 was launched, but L8 data were not used herein. L5 images were not available for the Ucayali River in 1999.

Landsat data for each of four bounding boxes in Figure 4.2 were downloaded via Google's Earth Engine API. The API allows users to download Landsat imagery based on inputs of sensor type, start and end dates, and coordinates of a bounding box. Downloads returned georeferenced $N \times B \times T$ Landsat files for each region of interest, where N is the number of Landsat scenes intersecting the bounding box, B is the number of spectral bands (seven for L5 and L7) , and T is the number of realizations of each scene.

Each pixel of each image was classified independently using Support Vector Machine (SVM) classification models within a hierarchical framework. SVMs have been widely used for classification of remotely sensed images [194, 195, 196]. SVM models were constructed iteratively via training samples collected from the region and satellite of interest. First, initial samples were selected by eye from images unobscured by clouds. These initial samples were collected only from land cover types that were visually well-defined. The performance of the initial models tended to be poor because some ambiguous land cover

types, such as sediment pixels at the boundary of the river, were not represented in the training set. The SVM models were accordingly updated by trial-and-error approach to incorporate ambiguous pixels as well pixels from various seasons to improve each model's performance. SVMs were developed iteratively for each region until the classification model achieved adequate accuracy across multiple image types per visual confirmation.

A total of eight SVM models were constructed, corresponding to an L5 and L7 model for each of the four R bounding boxes. Four pixel classes were defined: land, sediment, water, and cloud. For each pixel, the corresponding SVM model searched for a positive identification of a single class. If none were found, the next class was checked until either the pixel was successfully classified or could not be described by any of the classifications. The sediment class was checked first, followed by water, land, and finally cloud. Pixels not classified by the SVM were given a "NoData" tag.

4.4 Compositing imagery

For each year, individual classified images were "smashed" together to make a single composite image. Annual composites are required to overcome some difficulties inherent in using Landsat imagery. Landsat scenes within the same path are observed on the same day, but scenes from adjacent paths are collected at a minimum of eight days later. Thus where the river crosses Landsat paths (e.g. from path 6 to 7 for the Ucayali), a complete image of the river will not be available for the same date and a composite is necessary. Composites also allow information to be included from scenes that are partially obscured. For example, in some images clouds may hide portions of the river or the SLC malfunction of Landsat 7 creates stripes of missing data across the entire scene. Composite images have additional benefits beyond overcoming data shortcomings; they maximally resolve exposed in-channel sediment (bar morphologies) and provide consistent estimates of the bankfull channel planform.

4.4.1 Resolving bankfull planforms through compositing

In order to compare planforms interannually, the delineation of the river planform boundaries must be consistent for each year and should be independent of river stage. In other

words, an estimate of the bankfull channel planform [197] is required. Conceptually, the bankfull stage represents the water level at which flow begins to spill from the channel onto the floodplain. Though somewhat abstract, the bankfull discharge has been linked to more precise concepts of dominant discharge [198], i.e. the discharge performing the most geomorphic work, effective discharge [199], i.e. the discharge that transports the largest fraction of the annual sediment load, or the "x-year flood," i.e. the discharge that occurs with frequency of about one to three years [200]. In practice, field evidence of bankfull stage includes breaks in bank slope, changes in near-bank vegetation, transitions in soil type, and tops of bars [201]. In the absence of detailed field measurements across the large space and time domains of this study, the bankfull channel planform area was defined by the main channel (water pixels) plus connected exposed bars (sediment pixels).

Identifying bankfull stage thus requires a robust resolution of sediment from Landsat images–a difficult task due to the spectral similarity of sediment and clouds and the spectral "fuzziness" of partially inundated or vegetated bars. By compositing images, gaps and misclassifications of sediment from individual images are "filled in" by sediment identified in others. Average width computed from seven Landsat images (R4) within a single year where an unobscured view of the river was available demonstrates the variability in width measured from individual Landsat images alone (Figure 4.3A). Average reach widths obtained from individual images ranged from 25-31 pixels, while the composite image resulted in a greater average width (33 pixels) than any of the individual images, reflecting the integration of sediment pixels from the three images used to create the composite. Images composited through time will also integrate planform changes into the final composite. For example, if a series of images through which the river undergoes substantial migration is used to create a composite, the composite image would contain an artificially wider planform. In order to ensure a near-stationary channel across individual images, only those from periods of low discharges when lower shear stresses prevent substantial migration were selected for use. Flow in many tropical rivers is cyclic [202]; in the Ucayali, flows tend to be lower from June-October and larger from January-April (Figure 4.3A). These drier months are also conveniently the least cloudy and therefore provide the clearest images of the river. Very few unobscured Landsat images were available of the river at flood stage. Within R4, only two such images existed over the 1985-2015 period. These images were compared with

their corresponding composite images to confirm that the composite planform agreed with the high-stage (bankfull) planform (Figure 4.4).

4.4.2 The compositing process

An image bank was constructed for each year by selecting only the images from within the May-1 through Oct-31 window. For each year, each image in the bank was plotted, and N images with properly classified and clear views of the river were selected for inclusion in the composite. N ranged from 2-11; larger N were required for composites where cloud cover obscured the view of the river in many images. In order to minimize the accumulation of errors inherent in Landsat imagery and the classification process, no more than four clear views of the river were used to create a composite. With the exception of a section of R3-1990, the six-month search window was sufficient across all scenes and dates to create a reliable composite image.

The compositing algorithm gave preference to sediment pixels to maximally resolve in-channel and point bars. The N images were combined into a single $P \times N$ stack where P is the number of pixels each image contains, and a $P \times 1$ composite image was initialized with zeros. Each p^{th} pixel in the composite image was assigned according to a hierarchical scheme that gave preference to sediment, followed by water, land, and finally cloud classes. For example, if any of the N pixels in the pixel stack were classified as sediment, the composite image's pixel would be set as sediment. If not, the stack was checked for water, followed by land, and finally clouds. An example of the compositing process is shown in Figure 4.5A-D.

For each composite image, a corresponding datemap was also created by storing the date of the image that each pixel was drawn from. If, for a pixel, more than one image in the stack of N were the same class as the final composite class, the image whose date was nearest to the center of the search window was selected as the datemap value. Datemaps show the relative contributions of each image to the final composite (Figure 4.6). For the R3 and R5 boxes, no image from a single date could cover the entire river because it crosses Landsat paths. Thus these boxes required approximately twice the number of images to create a single composite. In R4, over 70% of each composite was contributed by a single image except for 1990, 2002, and 2012. In R6, exceptional cloud cover necessitated more

individual images to create composites.

The compositing process also revealed errors in georectification of some Landsat images (Figure 4.5E-F). A total of 20 scenes from the May-October window in 1985-2015 across all R boxes were found to be misaligned. These images were detected through by visual inspection of each composite and removed from the stack which was subsequently recomposited. In 2016, the USGS announced a reprocessing of all Landsat imagery to correct these and other geolocation errors `http://landsat.usgs.gov//about_LU_Vol_10_Issue_1.php`, but the corrected Landsat products were not available at the time of this study.

The compositing procedure was developed iteratively. Initially, compositing was performed using all available images within the six-month window to create the image stack. More sophisticated algorithms were developed to determine the composite pixel class from a pixel stack; for instance, the composite pixel would be sediment class only if >30% of the pixels in the stack were sediment. This methodology was robust against improperly classified pixels, but it failed to resolve the bankfull channel for cases where few full, clear scenes were available. The simpler method employed here resulted in noisier composites (e.g. where clouds are misclassified as sediment, they show up as sediment in the composite), but required fewer images to create a representative composite. As a result, the composites required additional cleaning discussed in the following section.

4.5 Creating channel masks from composite imagery

Planform statistics including migration rate, width, radius of curvature, and channel direction require a well-defined centerline. The Ucayali River's abundant chute channels, avulsions, connections to oxbow lakes, tributaries, and riverside cities required disconnection from the main channel body before a centerline could be identified. Additionally, noise in the composite images from errant classifications should be removed wherever it intersects the channel body. Manual cleaning of the composites is thus required. Cleaning is also important to ensure consistency across imagery. For example, consider quantifying erosion and deposition by differencing composite-derived channel masks at different times. If a composite contains a chute channel at t_1 but not at t_2 due to poor Landsat imagery, but the chute is again detected at t_3, its absence at t_1 will appear as deposition, and its reemergence at t_2 will be considered erosion, while no erosion or deposition actually

occurred.

Each composite image was thus manually cleaned by removing all connected components that were not hydraulically connected to the river (i.e. tributaries, cities, misclassified clouds, cutoff remnants etc.). First, a binary mask of the composite was created from the water and sediment pixels. This mask was plotted alongside the original composite image for reference, and the areas not connected to the main river body were removed. In order to achieve consistency across the cleaned images, the cleaned binary image from the previous time step was superimposed onto the image being cleaned. The most common cleaning procedures included the removal of tributaries, cities, and misclassified clouds and the filling of missing data due to insufficient Landsat imagery, cloud cover, or SLC-off bands. Hand interpolation because of missing data was required for only a few composites, and interpolations were over distances less than a channel width. The result after cleaning was stored as a binary image containing all the hydraulically connected area of the main channel.

Cleaning was performed using RivMAP's *hand_clean* function, which allows the user to create a mask from a hand-drawn region of interest (ROI). After drawing an ROI, its class (e.g. water, sediment, land, etc.) was defined by a numeric input and further ROIs were drawn and re-classed until cleaning was complete. The hand cleaning process was the most time-consuming step of this study and could be improved or eliminated with a refined classifier, more Landsat imagery, and/or a path-finding algorithm that follows the main channel banklines.

Following cleaning, a single-thread channel mask was created by selecting the primary river path at each bifurcation. In order to determine the active channel in a multi-threaded portion of the river, channel width and temporal consistency were prioritized. As avulsions or chutes gradually emerged from a bend, imagery from the next several years was referenced to ensure a consistent channel devoid of artificial jumps in the centerline. For example, in many meander bends a "tip cutoff" would occur where a smaller chute channel would bypass the apex of the meander bend. Though narrower initially than the meander bend tip, this chute channel would grow through time and eventually coalesce with the bend tip. If the chute channel became wider than the bend during its evolution, it was considered the main path of the river throughout all times. Similarly to the cleaning

procedure, creating a single-thread mask was performed with the mask from the previous time superimposed to ensure consistency of path selection. The resulting image after path selection was stored as a binary image of the dominant, single-thread river path.

4.6 River Morphodynamics from Analysis of Planforms

RivMAP provides tools for quantifying static planform geometries from binary channel masks including centerline and bankline extractions, widths, lengths, angles, and curvatures. Functions are also provided to measure changes in time, including centerline and bankline migrated areas, areas of erosion and accretion and cutoff identification. The toolbox was developed using 30 meter Landsat data but may be applied to binary channel masks of any resolution. The large spatial domain and high temporal frequency of this study demanded functions be rapid yet computationally inexpensive, and to this end some functions are parallelized. Though not described here, the toolbox also contains a function to stitch together georeferenced imagery so that results may be recombined post-processing. The toolbox was designed and tested for analysis of single-thread channels, but many of the functions will handle braided channels as well. The algorithms and a demo with data from the R6 box are provided in the supplementary information. Though no GUI is currently offered, functions are written intuitively and well-commented for ease of customization and application to various problems. The RivMAP toolbox does require Matlab's Image Processing Toolbox. The following sections detail some of the algorithms included in RivMAP.

4.6.1 Centerlines and banklines from channel mask

The RivMAP tool for obtaining a centerline from an image mask (*centerline_from_mask*) requires only two inputs: a channel mask and a two-character variable (*exit_sides*) that denotes the sides which the channel enters (upstream) and leaves (downstream) the image. For example, the channel shown in Figure 4.7A would have *exit_sides*='EW'. First, holes in the input mask are filled, and any areas of the mask not connected to the main channel are removed. The mask is then skeletonized by evenly eroding its boundaries without breaking its connectivity. Skeletonization resolves the centerline well, but poses two problems. First,

the skeleton at the ends of the channel mask no longer traces the centerline, as it must intersect the corners of the object (channel mask) being skeletonized (Figure 4.7D). This is overcome by padding the channel mask image with mirrored versions of itself, providing a channel with smooth transitions beyond the boundaries of original mask. The centerline is obtained from the padded image and then cropped to remove the boundary effect of skeletonization. The second problem of skeletonization is the presence of unwanted spurs that must be removed (Figure 4.7D). Rather than removing spurs individually, the centerline is found as the shortest path along the skeleton between its endpoints. The coordinates of the shortest path are arranged from upstream to downstream and returned as a two-column vector. These original centerline coordinates are retained for further processing, and a smooth centerline is also created with a first-order Savitzky-Golay [203] smoothing filter. See [103] for effects of centerline smoothing with the Savitzky-Golay family of filters. The centerline is resolved at single-pixel resolution, so centerline node spacing depends on the resolution of the input mask. Centerlines may be computed for both single- and multi-threaded channels, but for the latter the centerline of the holes-filled channel mask will be returned.

Banklines are extracted from a binary channel mask by taking advantage of Matlab's efficient image processing tools. The *banklines_from_mask* function requires inputs of a channel mask and its exit sides; if the input mask contains a multi-threaded channel, the function will return the extents of the mask as the banklines. The mask image is first cropped such that the ends of the river intersect the edge of the image, and any holes within the mask that border the image boundary are filled (Figure 4.7F-G). The perimeter of this image is found and separated into left and right banks by removing all pixels at the image boundaries except the bankline pixels (two for each exit side). Banklines are found as the shortest distance between the bank endpoints. This technique has the effect of bypassing diagonally-connected pixels, returning a smoother bankline than the set of mask edge pixels (Figure 4.7J). Bankline coordinates are found by tracing each bankline, and coordinates are evaluated to determine the left and right banks (looking downstream) and arranged in an upstream-to-downstream order.

4.6.2 River Widths

The RivMAP toolbox includes two methods for computing river widths. An image-based average reach width between any two streamwise distances is computed by *width_from_mask*, while width at any point along the centerline can be computed using *width_from_banklines*. The *width_from_mask* routine requires inputs of a channel mask, its centerline, and the desired interval to compute widths. Intervals can be defined as a single value in the same units of the centerline (pixels) or a vector containing the streamwise distances defining the edges of buffer polygons. First, the centerline is parameterized by the streamwise distance computed as the sum-of-squares between successive (x_i, y_i) centerline points:

$$ds_i = \sqrt{(x_{i+1} - x_i)^2 + (y_{i+1} - y_i)^2} \tag{4.1}$$

The reach-average width of the entire channel mask is then computed for use in parametrizing centerline smoothing and buffer sizing:

$$W_{ra} = \frac{P}{\sum ds_i} \tag{4.2}$$

where P is the number of pixels in the holes-filled channel mask and the summation of dsi is over all centerline nodes in the channel mask. Centerline coordinates are smoothed via a first-order Savitzky-Golay filter [203] with a window of $2W_{ra}$. Smoothing permits a continuous, stable estimate of the centerline direction at each node computed as

$$\theta_i = \arctan\left(\frac{y_{i+1} - y_i}{x_{i+1} - x_i}\right). \tag{4.3}$$

The centerline is broken into J segments of equally-spaced length defined by the input spacing, and a buffer polygon is created for each jth segment by first constructing perpendicular vectors of length $4W_{ra}$ at the first and last nodes of the segment. If the channel mask planform contains variations in width greater than $4W_{ra}$, the length of the perpendicular vectors should be increased. The perpendicular vectors are connected by polylines defined from the centerline nodes within segment j for the left and right banks:

$$\begin{aligned}(x_{lb,i}, y_{lb,i}) &= (x_i - (\sin(\pi - \theta_i))\, 2W_{ra}, y_i - (\cos(\pi - \theta_i))\, 2W_{ra}) \\ (x_{rb,i}, y_{rb,i}) &= (x_i + (\sin(\pi - \theta_i))\, 2W_{ra}, y_i + (\cos(\pi - \theta_i))\, 2W_{ra})\end{aligned} \tag{4.4}$$

This scheme creates buffer polygons that follow the channel planform direction rather than rectangular buffers which can produce excessive unwanted overlap, especially along sharp bends. In regions of high centerline curvature, the perpendicular vectors at the beginning and ending of segment j may intersect; in these cases the buffer is truncated at their intersection (Figure 4.8A). The buffer polygon is converted to a binary image of the same size as the input mask, and the intersection of the buffer mask with the channel mask returns the number of channel mask pixels within the j^{th} buffer (P_j). The centerline length within each jth buffer is found by

$$l_j = \sum_{i(j)}^{i(j+1)} ds_i \tag{4.5}$$

where $i(j)$ refers to the i^{th} centerline node at the beginning of segment j. The width of segment j is finally computed as

$$W_{avg,j} = \frac{P_j}{l_j} \tag{4.6}$$

where P_j is the number of pixels in segment j.

Buffers are conservative in the sense that each pixel in the channel mask belongs uniquely to a buffer, i.e. no pixel is double-counted and no pixel is uncounted. Typically, the overlap between the buffer and the channel mask contains only one region of connected area called a "blob" (see Figure 4.8C). However, in some cases, particularly where the river doubles-back on itself, the buffer might also overlap a portion of the doubled-back reach resulting in multiple blobs. Unwanted blobs are detected by computing the distance from the centroid of each blob to the midpoint of the centerline between the beginning and ending nodes of segment j. If this distance is greater than $1.5\bar{l_j}$ the blob is removed, where the overbar denotes the mean over all j segments.

Channel widths at each centerline node may be computed from banklines with the *width_from_banklines* function, which requires inputs of the left and right banks, centerline, and a nominal reach width (e.g. W_{ra}). Line segments perpendicular to each centerline node are generated whose lengths depend on the local centerline. Channel widths tend to increase where curvature is larger, i.e. around bend apices, thus longer perpendicular segments are created for higher curvatures (Figure 4.8D). The segment length's dependence

on curvature ensures that each segment intersects both banks. The points of intersection between the perpendicular segments with both banks are found, and the channel width (W_{bl}) is computed as the distance between them. In cases where a perpendicular segment intersects more than two banks, only the two nearest intersections are kept.

4.6.3 Migrated areas and cutoffs from centerlines and banklines

The RivMAP toolbox includes two methods for quantifying channel migration by measuring the areas traversed by the planform. Centerline and bankline migration areas are computed with the *migration_cl* tool, and erosional and depositional areas are obtained by planform mask differencing by the function *migration_mask*. Both functions contain routines for separating cutoffs from migrated areas. The functions to quantify planform migration and identify cutoffs rely on image processing techniques rather than vector-based (e.g. [186]).

The *migration_cl* tool requires inputs of coordinates obtained at different times, their exit sides, a nominal channel width (e.g. W_{ra}), and the size of the image from which coordinates were derived. Both centerline or bankline coordinates may be used, and they may be smoothed or not. The example shown here is a pair of smooth centerlines from R5, 1987-1988. First, a binary mask is created for both centerlines (Figure 4.9A). The areas to the side of each image are filled (Figure 4.9B-C) resulting in two images I_{half,t_1} and I_{half,t_2}. The side selected for filling depends on the provided exit sides and is consistent for both images. An image of migrated area is computed by the union of the forward and backward difference of the images at times t_1 and t_2:

$$I_{M,cl} = (I_{half,t_2} - I_{half,t_1}) \cup (I_{half,t_1} - I_{half,t_2}) \,. \tag{4.7}$$

A check ensures that the centerline at t_1 contributes no area to $I_{M,cl}$ and that the centerline at t_2 does, except for pixels where the centerline has not migrated (Figure 4.9E).

If the centerline undergoes cutoffs between t_1 and t_2, the cutoff areas will appear as migrated area in $I_{M,cl}$ and require separation. Dynamic rivers such as the Ucayali can undergo multiple cutoffs in a single year, and cutoff bends take on a variety of sizes and shapes from the classic fully-developed Kinoshita bend to "tip cutoffs" where only the tip of a bend is bypassed. After finding the image of migrated areas, the RivMAP function

migration_cl identifies cutoffs by thresholding the change in streamwise distance between centerline segments (Figure 4.10). First, all intersections between the centerline at t_1 and t_2 are found and ordered upstream-to-downstream. Each consecutive pair of intersections defines a segment; the centerline length of each segment is found for both t_1 and t_2 centerlines as:

$$seglen_{j,t_1} = \sum_{i(j)}^{i(j+1)} ds_i \tag{4.8}$$

where $i(j)$ refers to the i^{th} centerline node corresponding to the j^{th} segment. Cutoffs are defined by segments that were shortened by more than twice the channel width, i.e. when $seglen_{j,t_1} - seglen_{j,t_2} > 2W_{ra}$. A binary mask is constructed from the t_1 and t_2 centerlines bounded by segments fulfilling this inequality. Migrated area maps of the Ucayali showed that cutoffs often featured "tails" of thin migrated area where adjacent bend migration areas connect to the cutoff area (see Figure 4.10C-D). These tails are disconnected by eroding the cutoff mask and keeping only the largest connected area. The eroded mask is then over-dilated to ensure all actual cutoff area is retained, and the mask is applied to $I_{M,cl}$ to separate cutoff areas from migrated areas. The *migration_cl* function returns an image of migrated areas with cutoffs removed, an image of cutoff areas, the areas of each cutoff, and the cutoff indices along the t_1 centerline.

4.6.4 Migrated areas and cutoffs from mask differencing

The *migration_mask* function in the RivMAP toolbox provides a second way to quantify planform change through channel mask differencing. Mask differencing requires no centerline, thus both hydraulically-connected masks or single-thread masks may be used. The function requires two channel masks at t_1 and t_2 and a nominal channel width (e.g. W_{ra}). A differenced image is created via

$$I_{diff} = I_{t_1} - I_{t_2} \tag{4.9}$$

and erosional, no change, and depositional area images are found:

$$
\begin{aligned}
I_e &= I_{diff}(-1) \\
I_{nc} &= I_{diff}(0) \\
I_a &= I_{diff}(1)
\end{aligned}
\tag{4.10}
$$

Two methods are included for identifying cutoffs from mask-differenced areas. If the image of cutoff areas computed by *migration_cl* is provided, cutoff areas are identified as the connected areas of the I_a image that overlap the input cutoff areas image. Otherwise cutoffs are identified with a simple area threshold on the connected areas within I_a. For the Ucayali, a threshold of $3W_{ra}^2$ successfully discriminated between cutoffs and large patches of connected accretion areas (see Figure 4.11). Four images are returned by migration_mask: I_e, I_a, I_{nc}, and an image of cutoff areas.

4.6.5 Quantifying changes in space and time

Annual images of bankline or centerline migrated areas or erosion and accretion may be used to compute migration rates over desired space and time domains. For example, the average rate of migration for a reach between two times can be defined as

$$
M = \frac{A}{l_{avg}(t_2 - t_1)} \tag{4.11}
$$

where A is the total migrated area traversed by the centerline (A_{cl}) or eroded (A_E), l_{avg} is the average centerline length between t_1 and t_2, and M has units length/time. This definition of M quantifies the average area of migration per length of centerline and is not directly comparable with at-a-point lateral migration rates measured with respect to the perpendicular of the channel axis, e.g. the migration rates measured via erosion pins by [204]. Migration rates may also be normalized by channel area by replacing l_{avg} by the channel area (A_{chan}) in Equation (4.11). The RivMAP function *spatial_changes* returns the quantities A, l_{avg}, and A_{chan} at desired intervals along a channel. The main challenge in quantifying spatial changes lies in constructing a mesh of buffer polygons that include all channel positions through time, are roughly equally spaced, and orient approximately normal to the channel belt axis.

The *spatial_changes* function requires all the images of migrated areas and channel positions as well as each of the individual centerline images found using *centerline_from_mask*.

A desired spacing (D) over which to compute quantities is also required. First, the channel belt boundaries are found by dilating the image of all channel positions and calling the *banklines_from_mask* function to return its edgelines. Each edgeline is "oversmoothed" with a first-order Savitzky-Golay filter [203] of window size $50W_n$ to remove bend-scale edgeline variations while preserving the lower-frequency channel belt meandering. A mask of the channel belt is then constructed from the oversmoothed banklines. The smoothing procedure typically decreases the width of the channel belt so that its boundaries no longer include all the channel positions. The procedure is thus repeated with dilations incrementally increased by $0.5W_n$ until the mask overlaps all pixels of the all channel positions image (Figure 4.12A).

After the edgelines of the channel belt are found, they are coarsely resampled at intervals of $20W_n$. The nodes of the coarsely-sampled edgelines are used to construct an intermediate piecewise cubic spline [100], and the edgelines are resampled from the spline at a finer resolution ($0.1W_n$), resulting in two densely sampled edgelines that have been smoothed via a third-order interpolant (Figure 4.12B). Resampling via piecewise cubic splines is necessary to provide a smooth curvature signal. An approximate centerline is computed as the average coordinate positions of the edgelines, and its inflection points are found by zero-crossings of its curvature signal. Centerline inflection points are filtered such that each inflection is at least $3D$ away from the ends of the centerline and at least $3D$ away from the nearest adjacent inflection. For each inflection point, a line perpendicular to the centerline is intersected with each edgeline, thus matching each centerline inflection node with a corresponding left (pl_i) and right (pr_i) edgeline node. The number of buffer polygons ($n_{b,i}$) to create between each inflection point is computed as $\left(S\left(pc_i+1\right)-S\left(pc_i\right)\right)/D$ where $S(pc_i)$ is the streamwise distance from the upstream end of the reach to centerline inflection point pc_i. Finally, each edgeline is again resampled from the piecewise cubic spline at intervals defined by $\left(S\left(pl_{i+1}\right)-S\left(pl_i\right)\right)/n_{b,i}$ and $\left(S\left(pr_{i+1}\right)-S\left(pr_i\right)\right)/n_{b,i}$ (see Figure 4.12C).The procedure results in buffer polygons that are roughly perpendicular to the larger channel belt, while locally the buffers themselves are wider along outer banks and narrower along inner banks (Figure 4.12E).

Buffer polygons are constructed by connecting each node of the left edgeline with its

right edgeline counterpart, and connecting each node to its nearest upstream and downstream neighboring nodes (Figure 4.12D). A mask is created from each buffer polygon and applied to each image of areas, returning a $Y \times n_b$ matrix where Y is the number of realizations (e.g. 30 for this study). This matrix quantifies areal changes in space and time, and can be plotted as a spacetime map of planform changes (see Figure 4.16A). The average centerline length (l_{avg}) within each buffer polygon is also computed. The example shown in Figure 4.12 demonstrated centerline migrated areas, but areas of erosion, accretion, channel position, and sediment may be found with the tool.

4.7 Application and insights from the Ucayali River

Quantifying reachwide spatial and temporal morphodynamic variability and identifying controlling processes and events that contribute to this variability is critical for contextualizing local or bend-scale analyses of a river system. RivMAP was applied to the single-thread channel masks of the Ucayali River to quantify its morphodynamic evolution. Secondary channels along the Ucayali River captured by the hydraulically-connected binary masks may also play significant roles in floodplain reworking and the sediment budget but are beyond the scope of this study. The following subsections present quantified planform changes in length, width, erosional and accretional areas, and migration rates through the interpretation of spacetime maps. Each spacetime map was created by applying the buffer polygons shown in Figure 4.12E to the relevant reachwide map of areas (Figure 4.15) each year. The distance along the channel belt centerline was used to parameterize the downstream distance for the maps. The analysis is appropriate for quantifying planform changes at the reachwide scale, acknowledging that bend-scale analyses may require more precise tools or smaller buffer polygons. The Ucayali River is relatively data-sparse, but available regional precipitation records, local stage recordings, and SRTM elevation data are used to interpret some of the observed variability in planform changes of the Ucayali River. This section concludes with an uncertainty analysis performed by applying the classifying, cleaning, compositing, and quantifying planform change techniques to three pseudo-stationary bends where planform changes were assumed to be negligible.

4.7.1 Centerline changes including cutoffs

Annually-resolved centerlines for over 1,300 km of the Ucayali River from 1985-2015 created using RivMAP illustrate the complex and active morphodynamics of the river (Figure 4.13). Bends along the Ucayali River exhibited a variety of migration modes including translation, expansion, extension, and/or rotation [110]. Two mild-curvature bends in R5 (right zoom) displayed nearly pure downstream translation with little deformation. Consistent with linear perturbation models of long-time meander migration under subresonant conditions [2, 112], the length of most bends increased in time as meanders developed upstream-skew asymmetries. The development of multilobed meanders from single loop meanders is particularly striking in R6 (left zoom) and R4 (left zoom). At least two bends "reverse-developed" by shortening and initially increasing apex curvature over 30 years (one shown in R4, right zoom).

Centerline length changes were quantified via sinuosity computed as the ratio of the centerline length to the length of the valley centerline axis. The valley centerline was estimated by averaging coordinates of the channel-belt edgelines (shown in Figure 4.12E). From 1985-1996, sinuosity fluctuated around 2.07, reflecting an apparent balance between channel elongation and the 14 cutoffs of the period. In 1997 the largest cutoff within the study area and period—a human-induced 73 km triple-lobed cutoff at Masisea—occurred near Pucallpa [191], overwhelming the river's potential for centerline growth and leading to a sharp decline in sinuosity which achieved a minimum of 1.9 in 2005 following a series of smaller cutoffs. Despite the prevalence of cutoffs throughout the reach from 2006-2010, sinuosity rebounded to its 2015 value of 1.97.

The occurrence of cutoffs does not necessarily imply a decline in reachwide sinuosity between two times, as sinuosity depends on the balance between the cutoff rate and the elongation rate (e_r) of the river given by

$$e_r = \frac{l_{cl,t_2} - l_{cl,t_1} + l_{cut,t_2}}{t_2 - t_1} \tag{4.12}$$

where l_{cut,t_1} is the total cutoff length at time t_1. For example, the cutoff rate from 1997-2002 (39 km/yr) was nearly equal to the 2006-2010 period (37 km/yr), yet the sinuosity declined 7% for the former and increased 1% for the latter. The discrepancy is due to elongation along the reach (Figure 4.14B). The period of lowest sinuosity (1998-2010) was also

the period with the largest elongation rates, reflecting the Ucayali's self-adjusting response to its loss of floodplain access and steeper reachwide slopes due to cutoffs. The elongation rate of the Ucayali exhibited an overall increasing trend across the 30 year period, including a maximum rate of 51 km/year, or about 4% of the centerline length/yr. The average absolute reach curvature maintained a steady value from 1985-1997 despite a number of large cutoffs (Figure 4.14C). Beginning in 1998, average reachwide curvature began a steady decline in tandem with decreasing sinuosity, indicative of centerline straightening. While sinuosity rebounded throughout the 2000s, the average reach curvature continued decreasing, signifying a period of increasing average meander wavelength.

4.7.2 Spatio-temporal changes in widths and erosion/accretion areas

Average channel widths (W_{avg}) were computed annually using RivMAP's *width_from_mask* function to analyze the single-thread channel masks at intervals of approximately 3.5 channel widths (2.7 km) along the channel belt centerline. The spacetime map of the Ucayali River's bankfull widths shows remarkable multiscale variability (Figure 4.16A) around an average width of 813 meters. Averaging width across time (Figure 4.16B) reveals a reach-scale trend of downstream widening consistent with downstream hydraulic geometry relationships due to flow accumulation [205]. At the bend-scale, widths oscillate around this trend of downstream widening corresponding to larger widths near meander apices. Intermediate-scale variations in width, e.g. from km 80-100, over multiple meander bends indicate the presence of additional local controls on width. Such intermediate scale variations that persist across all times may be due to flow and sediment inputs from nearby tributaries, local discontinuities in floodplain resistance, or local geologic controls, while those that vary in time may represent morphological adjustments to cutoff perturbations.

Averaging width across space shows the temporal evolution of the average width of the Ucayali River (Figure 4.16C). The bifurcated reaches of R3, beginning at a downstream distance of 540 km, were not included in the spatial averages due to difficulties in aligning downstream distances for both reaches. Average width decreased 72 meters from 1985-1997, followed by an increase of 115 meters from 1997-2015. The trends of changing width may be partially due to climatic influence, as average width tended to follow the annual

precipitation depths for the Ucayali region [190]. However, for some years increased precipitation corresponded to decreased width (e.g. 1988-1990) and vice versa (e.g. 1987-1988, 1990-1991, 1993-1994). The spacetime map of average widths showed persistent channel widening at km 175-290 beginning in 1997, corresponding to the time and location of the largest cutoff in the domain (Masisea cutoff, 73 km long). A second region of increased widening is observed at km 60-100 beginning in 2002, corresponding to the second-largest cutoff in the domain (Tumboya cutoff, 43 km long). Temporal variations in channel width are thus likely modulated by both changes in climate and localized cutoff disturbances.

Channel width changes depend on the elongation rate and the balance between eroded and accreted areas. The spacetime map of reworked floodplain areas depicts the local annual balance of erosion and deposition (Figure 4.16D). Qualitatively, the map shows that regions of erosion or accretion tend to alternate through time rather than persist. Approximately 82% of locations featured persistence times, defined as the duration an area remains erosive or accretive, of less than two years; 55% switched after only a single year. Persistence through space was more prevalent, where the average persistence length was roughly 17 km of river centerline length (28 channel widths). These results suggest that net floodplain areal changes are likely controlled by reachwide temporal variations such as climate fluctuations.

Summing the eroded and accreted areas across 30 years reveals the spatial variability of local areas of floodplain growth and loss (Figure 4.16E). No downstream trend toward erosion or accretion was detected for the full reach, though significant spatial variability was observed. The downstream cumulative reworked areas reveal significant aggradation over a short distance surrounding the Masisea cutoff followed by a prolonged region of net erosion. A similar pattern was noted near the Tumboya cutoff, although to a lesser degree. A sediment budget of the Ucayali River Basin revealed that the Ucayali's floodplain from km 0 to km 238 (Pucallpa) acts as a sediment sink, storing 205 Mtons annually [206]. The observed aggradation downstream of the two cutoffs may result from lost access to floodplain storage via primary flow bypassing the cutoff reaches. The potential local effects of the Masisea cutoff to accelerate accretion may be amplified by the presence of the two largest tributaries along the reach, which join the Ucayali River near the Masisea cutoff (see Figure 4.17D). The spacetime plot provides further evidence that these tributaries do

promote local accretion, as large accretion areas were observed prior to the 1997 cutoff event.

Overall, the spatial balance of reworked floodplain areas across the reach exhibited very little net erosion or accretion despite local sustained imbalances between accretion and erosion. The time series of reworked areas shows a similar temporal balance over the 30 year period (Figure 4.16F). The short persistence times of accretion and erosion observed locally in the spacetime map are expressed in the annual sums as well. Floodplain reworking switched from net erosion to accretion, or vice versa, at most every two years. Cumulative reworked area through time shows that relative to 1985, the river was net erosional for only four years, primarily due to large accretions in 1994 and 2003. However, by 2010 the cumulative reworked area returned to zero after a 15-year period. Both spatially and temporally, the study domain and period was large enough to capture decadal and reachwide cycles of net erosion and accretion that suggest the Ucayali sustained both a spatial and temporal balance. However, the long-time and large-space balances are maintained by local variations affected by cutoffs, proximity to tributaries, annual climate fluctuations, variability in floodplain resistance, and local flow dynamics.

4.7.3 Spatio-temporal distribution of migration rates

Locally, reaches along the Ucayali have migrated as much as 750 meters per meter of centerline in a single year, while other reaches have barely moved over 30 years. The spacetime map of annual areas traversed by the centerline (MA_{cl}) normalized by channel area (Figure 4.17A) shows a large migration hotspot sustained throughout the full 30 year period (km 70-120) and another spanning 1997-2015 (km 200-270). Due to these hotspots, an overall trend of decreasing migration rates is observed in the downstream direction for the full reach. Neglecting the hotspots, a decreasing downstream trend of small magnitude persists downstream of the hotspots (Figure 4.17B). Within the hotspots, local migrated areas exceeded up to 40% of the total channel area for some years. On average, the Ucayali River's centerline traversed 5.9% of the local channel area per year. Curiously, between the two hotspots is reach of river that remained nearly stationary across 30 years (km 160-175). The reach consists of two mild-curvature bends that are 35% narrower than the average reach width and displayed almost no exposed in-channel sediment throughout the

period. High-resolution imagery revealed no apparent human modifications to their banks or floodplain. A second shorter reach (km 360-363) exhibited similar characteristics of stationarity, narrowness (20% smaller than average width), mild curvature, and no bars.

Averaging migration rates over space provides the temporal evolution of reachwide migration rates (Figure 4.17C), which show an increasing trend across the 30 year period. Over this same period, annual rainfall depths for the Ucayali River Basin and its neighboring Huallaga Basin increased on average 1.4 mm/yr [190], suggesting precipitation as a driver of long-term migration trends. In the absence of available discharge records along the Ucayali, daily stage data collected at Pucallpa (km 238) provided local estimates of the river's flow. Prior to the Masisea cutoff in 1997, annual variations of average migration rates closely follow annual variations of maximum annual stages (R^2=0.36, Figure 4.17C). The synchronicity between migration rates and mean annual stages (not shown) is less pronounced (R^2=0.30). A similar relationship between maximum flows and channel activity was reported for the Rio Beni [181]. Following the 1997 Masisea cutoff and initiation of the northern hotspot, the annual synchronicity between maximum annual stage and reach average migration rates breaks, although they continue to follow a similar decadal trend. The stage data was recorded near the Masisea cutoff and may have been affected by morphological changes such as bed aggradation induced by the cutoff.

The northern hotspot (km 200-270) appears to have been initiated by the 1997 Masisea cutoff event. Prior to 1997, migration rates along the reach were not substantially higher than the reach average. While it is likely that the Masisea cutoff induced the northern migration hotspot, major tributaries delivering water and sediment loads may have amplified migration rates initiated by the cutoff perturbation [178]. The locations of major tributaries to the Ucayali, i.e. those with drainage areas larger than $3x10^6$ km^2 are shown in (Figure 4.17D). The largest tributary, the Pachitea River (T1), alone accounts for 17% of the Ucayali's suspended sediment load immediately downstream its confluence [206]. However, sediment and discharge loads from large tributaries cannot explain the southern hotspot (km 60-130). Two major cutoff events occurred within the hotspot (see Sampaya 1 & 2, Figure 4.15C) that may have promoted accelerated migration rates, but the hotspot persisted prior to both cutoffs. A slope profile generated from SRTM data shows that between the upstream end of the study reach and Pucallpa (km 0-238), the Ucayali River

valley slope becomes steeper than the reach average for extended lengths [206]. These local regions of larger valley slopes may explain the location of the southern hotspot.

	length, pixels		W_{avg}, pixels		M_{cl}, $\frac{\%}{yr}$		Erosion Rate, $\frac{\%}{yr}$		Accretion Rate, $\frac{\%}{yr}$	
	mean (std)	range	mean (std)	range	mean (std)	max	mean (std)	max	mean (std)	max
Bend 1	451 (1.6)	7.2	21 (0.4)	1.4	1.2 (0.4)	2.1	3.5 (2.3)	9.8	4.0 (2.6)	12
Bend 2	222 (1.7)	6.6	19 (0.5)	2.1	1.2 (0.3)	1.9	2.5 (1.1)	5.7	4.1 (3.0)	13
Bend 3[a]	222 (1.1)	4.5	18 (0.7)	3.7	1.0 (0.1)	4.3	5.3 (1.0)	57	4.7 (5.0)	26
Bend 3[b]	221 (1.0)	3.8	19 (0.3)	1.1	0.7 (0.4)	1.5	3.3 (2.4)	7.4	4.0 (3.0)	11

Table 4.1: Uncertainty estimates obtained by applying RivMAP to three abandoned, non-active bends. Statistics are computed for 31 years of annual composite-derived channel masks. Centerlines were not smoothed. W_{avg} was found by averaging W_{bl} across all centerline nodes. Centerline migration rate M_{cl} was computed by Equation (4.11) using $A = A_{cl}$. Erosion and accretion areas were normalized by channel area. [a]Statistics include two years containing misgeorectified imagery. [b]The misgeorectified years were removed.

4.7.4 Estimating uncertainty

Uncertainty depends on the quality and resolution of the planform mask which integrates errors in geolocation, classification, and cleaning. Uncertainty bounds for planform variables measured by RivMAP were estimated by analyzing three abandoned bends annually from 1985-2015 following the procedures previously described. The bends were disconnected from the main river channel but were fed by small ($< 0.1W_{bend}$) tributaries. The planforms of bends were assumed to be stationary, although fluctuations in their stages and therefore their planforms may have occurred due to climate fluctuations or flooding. Conservatively, any measured planform changes of the bends were interpreted as systemic error. The bends were selected to sample various potential sources of uncertainty; Bend 1 was adjacent to a city (Pucallpa) that required separation each year, Bend 2 was highly obstructed by clouds and SLC-off bands for many years, and Bend 3 contained misgeorectified images in 1985 and 1987. The classification of sediment may also contribute significantly to errors in resolved planforms. However, the bends contained no exposed sediment so these errors are not represented. No stationary reaches with exposed sediment could be identified.

Table 4.1 shows that errors in planform variables are small relative to the 30-pixel width of the Ucayali River. However, Bend 3 demonstrates that measurements obtained from Landsat-based composites are highly sensitive to improperly georectified imagery. Errors in migration metrics are especially sensitive, as they are manifest in both the time when they appear as well as the succeeding time when the error is no longer present. In the absence of improperly georeferenced imagery, the maximum error for width was 2.1 pixels with a standard deviation of 0.5 pixel. Maximum errors for migration rates computed from migrated centerline areas, eroded areas, and accreted areas were 2.1, 9.8, and 13% of the total channel area , respectively. Centerline migration errors are lower than mask-differenced erosion/accretion errors due to the relative insensitivity of the centerline to spurious clouds or misclassified pixels along the channel mask boundaries. The error estimated here may not reflect the extent of potential errors across the full study area, but they provide an estimate for the typical sources of uncertainty. Analysis with RivMAP requires no input parameters other than a nominal channel width used to generate buffer boxes and parameterize cutoff threshold area, so errors reported here reflect the uncertainties associated

with processing Landsat imagery including classification.

4.8 Conclusions and Future Work

This study demonstrated the feasibility of quantifying planform changes in large, active meandering rivers on an annual basis by compositing images from Landsat data. Based on estimates of uncertainty associated with classifying and compositing Landsat data, the procedure described herein can provide meaningful annual morphodynamic insights in large and/or highly active rivers from Landsat imagery. The largest source of uncertainty comes from improperly georeferenced Landsat images that can affect long reaches if unaccounted. A forthcoming (2016 target release) re-processing of the Landsat database by the USGS should reduce or eliminate much of this uncertainty, permitting the analysis of smaller and less active rivers, as well as inter-annual analysis of individual Landsat scenes. With current Landsat data, over a dozen large, tropical meandering rivers, e.g. the Mamoré, Beni, Juruá, Fly, and Sepik Rivers, are ideal candidates for quantifying morphodynamic changes and identifying process controls on planform adjustments from Landsat imagery.

The RivMAP toolbox provides intuitive, easily-customized, and parallelizable Matlab codes tailored for working with meandering river masks derived from Landsat imagery, although they are applicable to binary planform masks obtained from other sources, e.g. aerial photographs, historic maps, or DEMs. By taking advantage of Matlab's efficient image processing functions, RivMAP tools can quantify widths, centerlines, banklines, centerline migrations, and erosion and deposition rates over large spatial domains with high temporal frequency using a personal computer. For example, once clean binary masks were obtained, computing these quantities for 1,300 km of the Ucayali River was performed in less than two hours on a quad-core laptop. The tools themselves are easily parallelizable across time and space (e.g. computing along-channel width) with Matlab's *parfor* command, and initial bounding boxes may be arbitrarily sized and processed in parallel. Finally, although applied to single-thread channel masks in this study, RivMAP can also quantify planform changes for multi-threaded channels.

The Ucayali River was particularly challenging due to its complex migration patterns, numerous secondary channels, and pervasive cutoffs, and RivMAP was designed around these complications. The 57 identified cutoffs along the Ucayali River in only 30 years

of observed change combined with their apparent effect on migration rates highlight the importance of high-frequency (annual) morphodynamic analysis. The vast potential for gaining insights into meandering river morphodynamics was demonstrated by showing spatial and temporal variations of planform change. Two major migration hotspots were identified along 1,300 km of the Ucayali River and linked to climate, local sediment supply from tributaries, and cutoffs. Although not analyzed in this work, the methods presented here also resolve in-channel sediment dynamics through planform views of bars exposed at low stage. Further study of the data is underway to more fully understand the effect of cutoffs as perturbations to migration rates, characterize floodplain residence times and dynamics, link meander migration to channel morphology, and investigate the effects of bar morphology on planform dynamics.

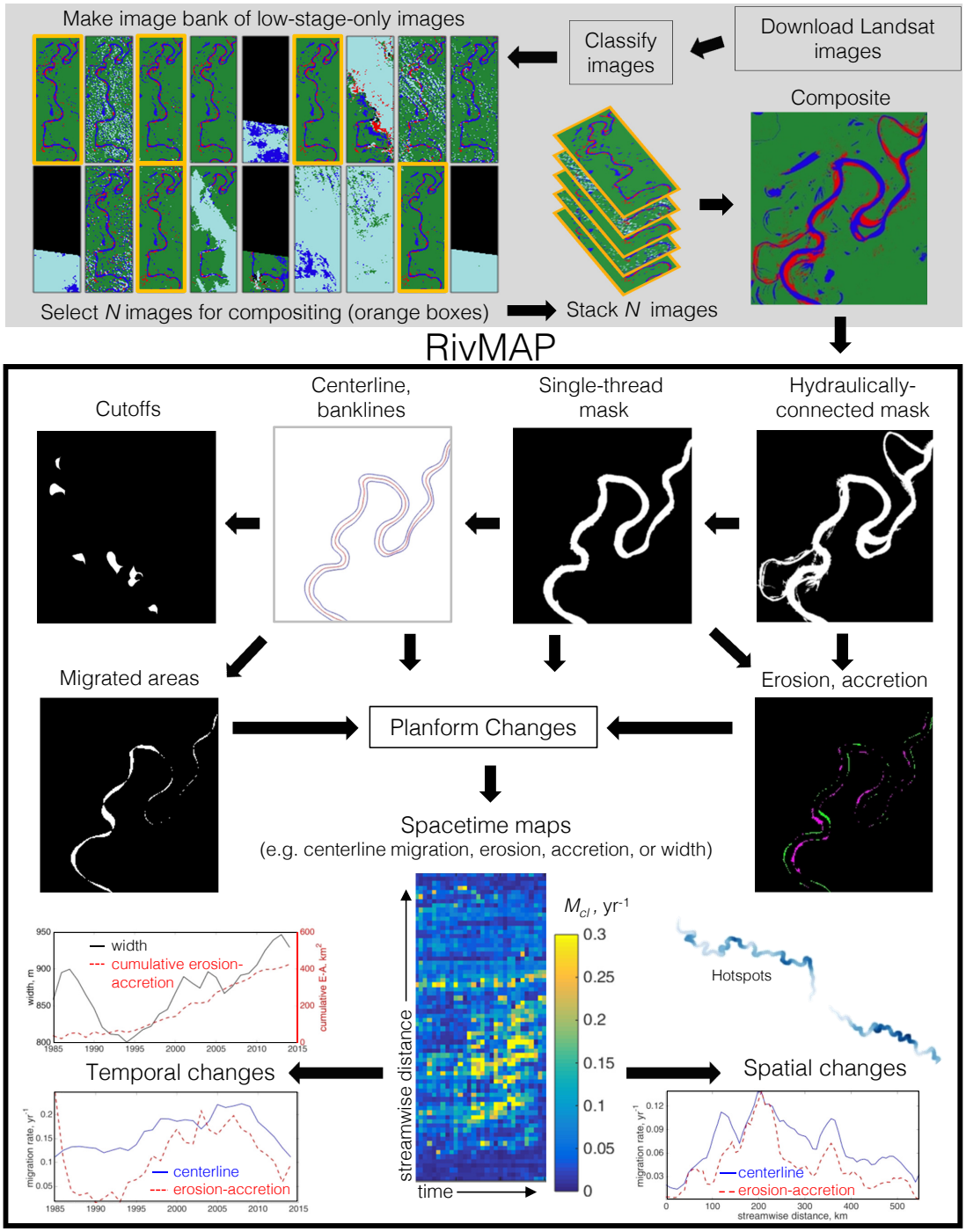

Figure 4.1: (Caption next page.)

Figure 4.1: (Figure previous page.) Diagram of the steps involved to quantify annual planform change from Landsat imagery. Imagery is downloaded, classified, and composited annually. The color images shown are classified Landsat imagery of a reach along the Ucayali River. Channel masks are created from the composite images. From there, the RivMAP toolbox is used to compute centerlines, banklines, widths, migrated areas, erosional/accretional areas, and cutoffs. The processing steps within the black box are supported by RivMAP. Examples of quantifying planform change are shown, including a spacetime map showing migration rates in space and time for a reach of the Ucayali River. Examples of temporal changes include average width, cumulative erosion-accretion, and migration rates, and spatial changes include migration rates, erosion-accretion, and mapping hotspots.

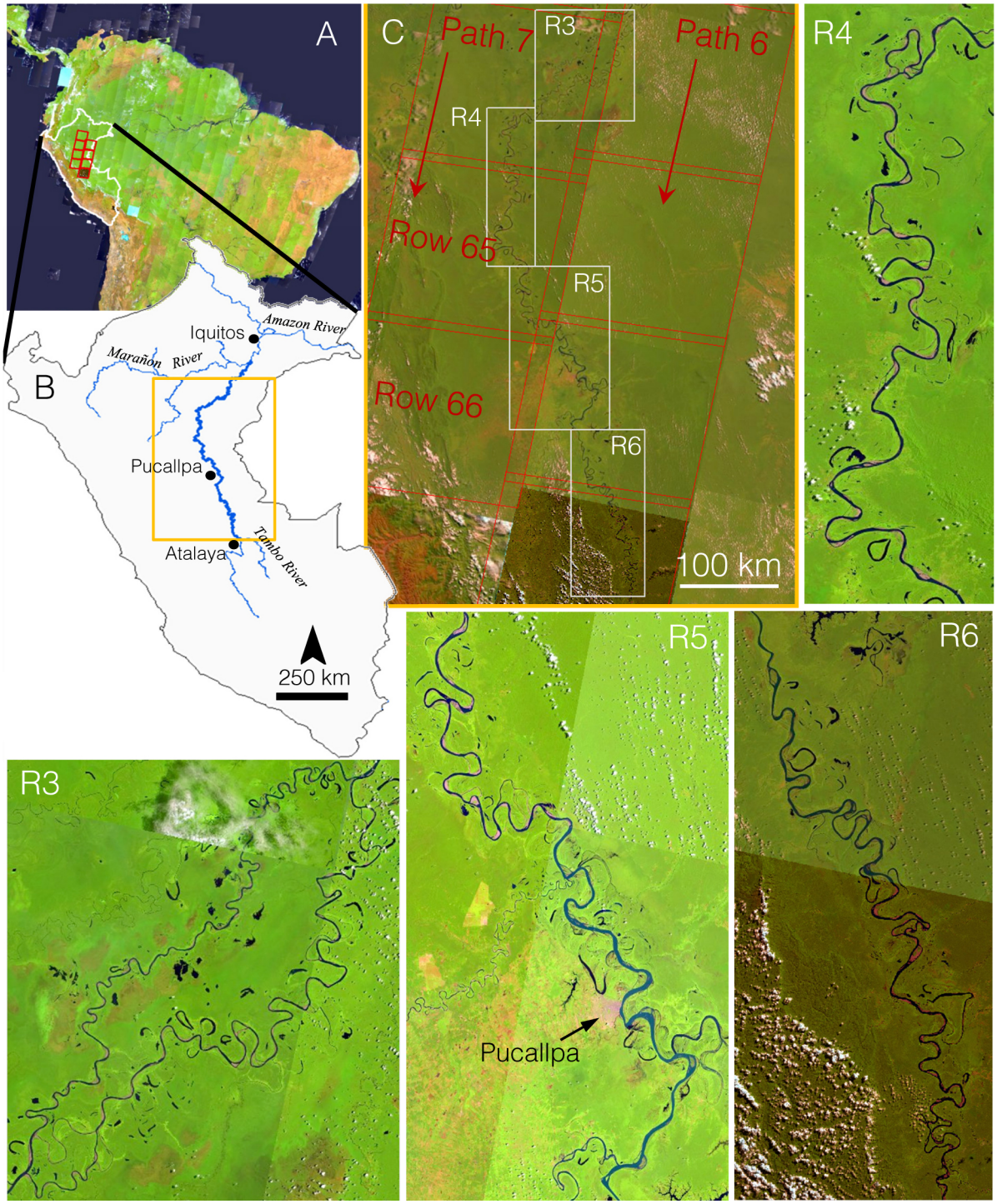

Figure 4.2: (Caption next page.)

Figure 4.2: (Figure previous page.) The Landsat scenes covering the study area are shown by the red boxes in (A). The extents of the study reach within Peru are delimited by an orange box in (B). A zoom view of the extents is shown in (C) with the Landsat scenes (red) and bounding boxes (white) overlain. The eight Landsat scenes intersecting the R boundary boxes range from Path 7, Row 64 (top left) to Path 6, Row 67 (bottom right). Each of the R bounding boxes is shown in more detail; the lower portion of the Ucayali's avulsion in the R3 box is considered the main channel for the analysis. Imagery is the latest available from the Landsat 8 Views collection spanning 2015-2016.

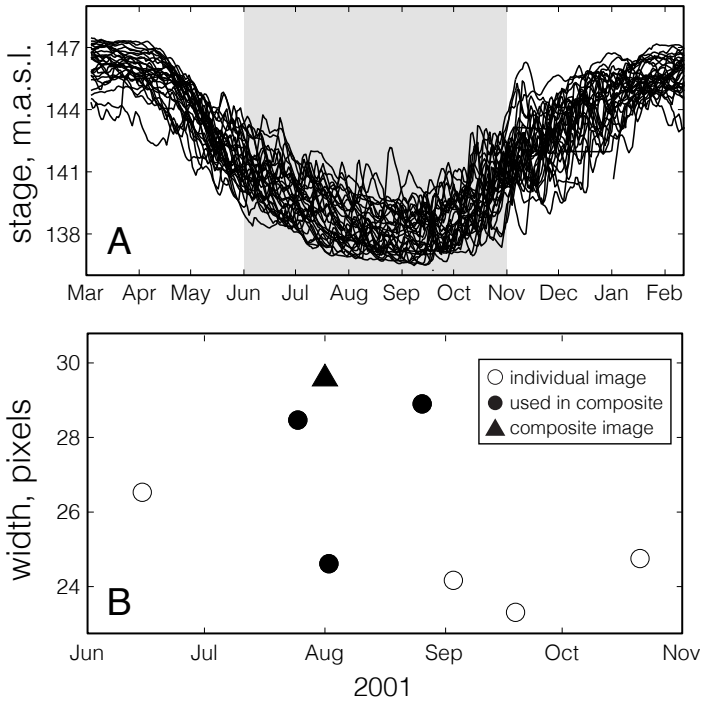

Figure 4.3: In (A), each line is a year of stage recordings of the Ucayali River at Pucallpa, Peru from 1981-2015. The shaded region delineates the period over which individual Landsat images were used for compositing. In (B), average widths of the Ucayali River within the R4 box (see Figure 2) are shown for individual Landsat images in 2001 (circles). Filled circles show the three images used to create the composite. The width of the composite image for 2001 (filled triangle) is plotted at the nominal date of August 1.

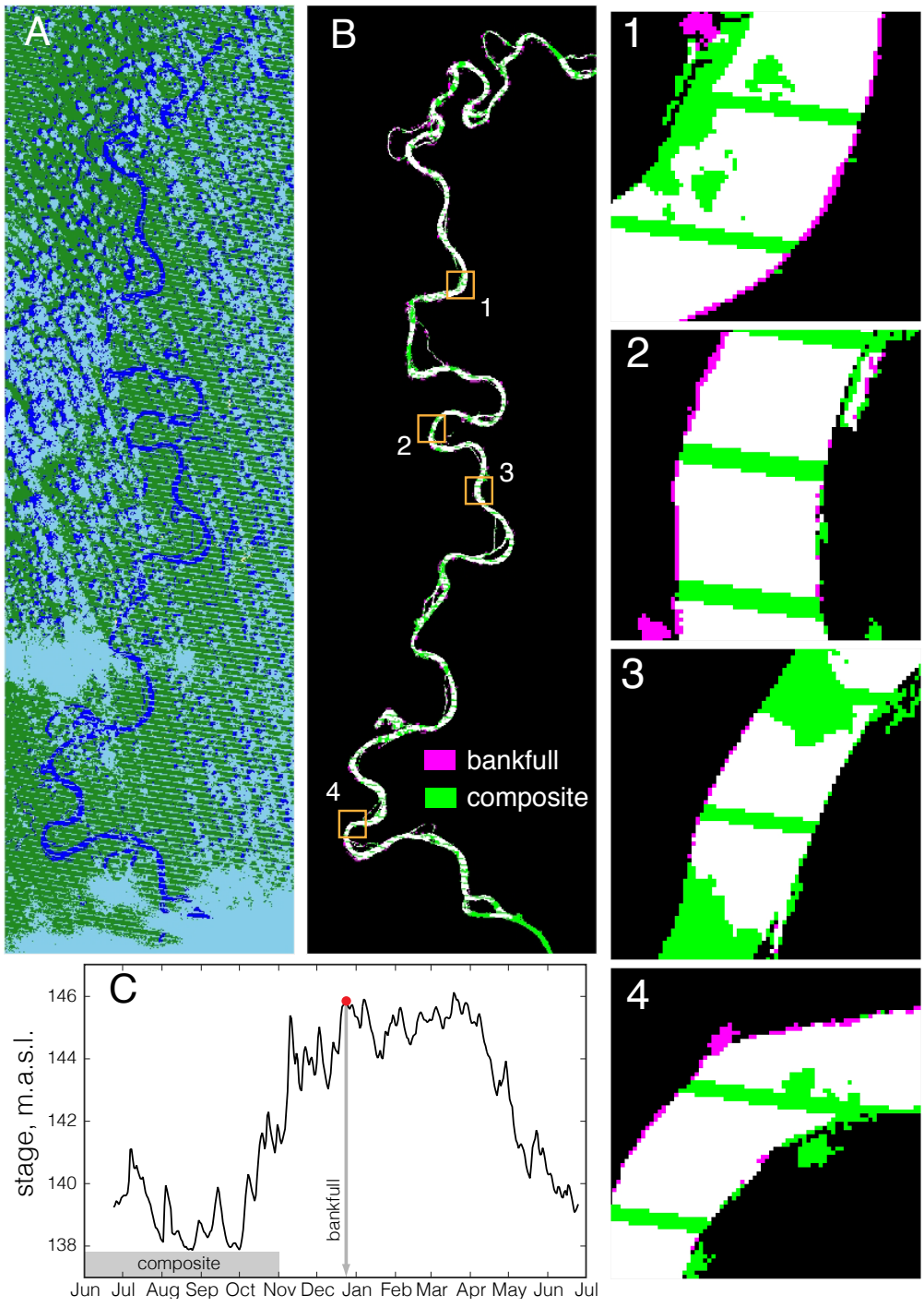

Figure 4.4: (Caption next page.)

Figure 4.4: (Figure previous page.) The river's planform at flood stage (bankfull) is compared with its planform from the composite image of the same water year. In (A), the classified Landsat image from Dec. 24, 2004 (R4) is shown. The river is at flood-stage; note the absence of exposed sediment (red pixels). The bankfull channel mask is superimposed with the composite in (B). Magenta indicates the presence of only bankfull channel, green shows the presence of only the composite image, and white corresponds to the presence of both. Four reaches displayed in more detail (1-4) show that the differences between the bankfull image and composite tends to occur only at outer banks, implying that migration is responsible for the discrepancies rather than an incomplete composite. The nearly complete overlap of the flood-stage mask and composite demonstrates that the composite reasonably captures the bankfull channel planform. In (C), river stage is shown from 2004-2005 with the stage at the time of the bankfull image is denoted by a red circle. The grey box spans the period over which images were drawn from for compositing, while the grey arrow points to the day of the bankfull image.

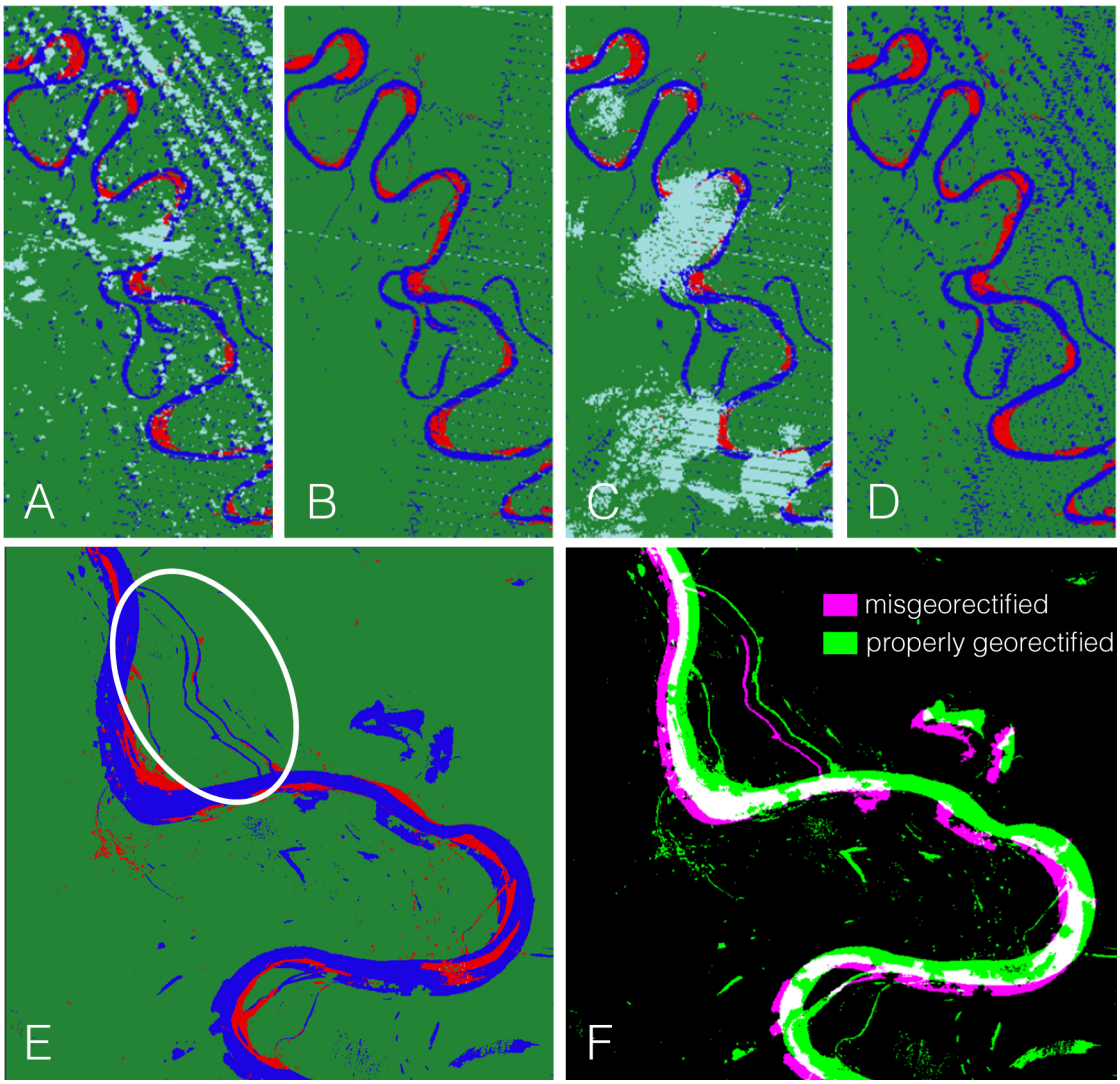

Figure 4.5: Three classified Landsat images from different dates (A-C) are used to create a composite image (D). Blue is water, red is sediment, and light blue is cloud. The portions of river obscured by clouds in (A) and (C) and the Scan Line Corrector-off lines in (B) and (C) are resolved in the final composite by information from the other images. Undesirable cloud shadows in (A) classified as water are carried through to the composite. An example of a composite created with an incorrectly georectified Landsat scene is shown in (E). The improper alignment is readily observed by the doubled chute channel (circled), but is more difficult to detect from the main river body alone. In (F), the two binary masks of the Landsat images used to create the composite are superimposed. This scene is from R4, 1989, and the individual images were taken 96 days apart.

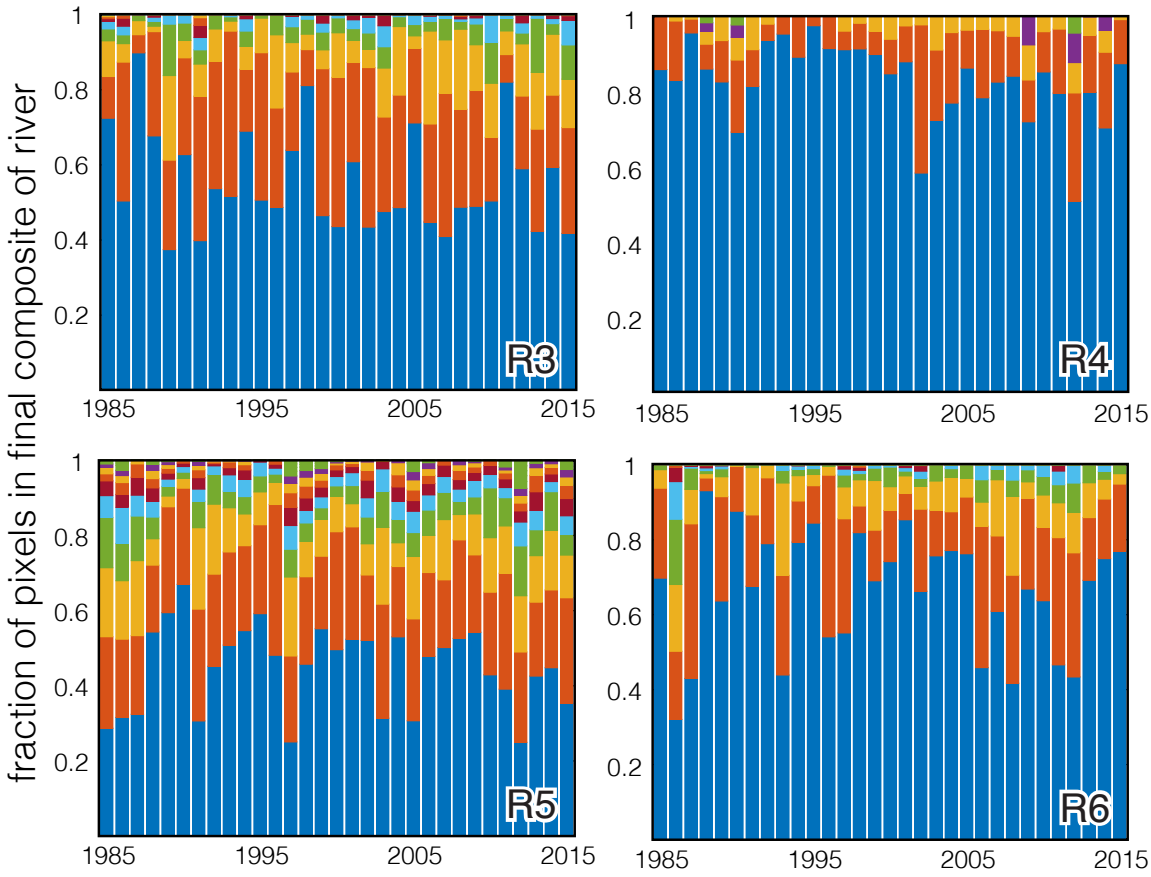

Figure 4.6: The contributions of pixels from individual classified images to the final composite river mask are shown for each year within each R box. The y-axis represents the number of pixels contributed divided by the total number of pixels in the binary channel mask. Each color represents a different individual image; the number of colors for a given year corresponds to the number of images that contributed to resolving the channel. Contributing image fractions are sorted from largest to smallest (bottom to top).

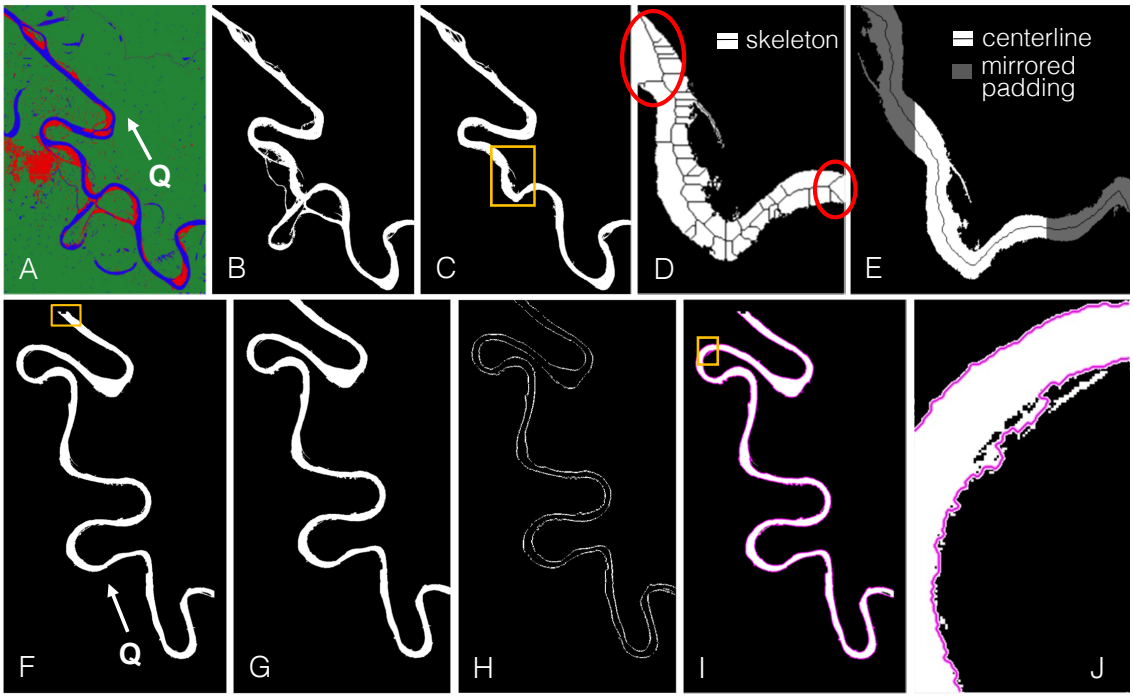

Figure 4.7: The steps for obtaining a centerline (top row) and banklines (bottom row) from a composite image are illustrated. A composite image is shown in (A) from R5, 1989. The red patch is the city of Pucallpa, Peru. In (B) the cleaned, hydraulically-connected channel mask is shown and its single-thread counterpart is shown in (C). The orange box denotes the extents of the image in (D). In (D), the skeleton of the channel mask is shown. The problematic ends of the skeleton are circled. The padding technique for resolving the ends of the centerline is illustrated in (E) along with the final centerline for the channel mask. The steps for extracting banklines from a channel mask are illustrated in the bottom row (F-J). A binary channel mask from R5, 2007 is shown in (F) with a notch artificially removed from the downstream end (orange box) to simulate a multi-threaded channel edge. The image after cropping is shown in (G), and its perimeter in (H). The extracted banks are shown in (I), and a zoom view in (J) shows how the banklines bypass corner-connected pixels of the channel mask.

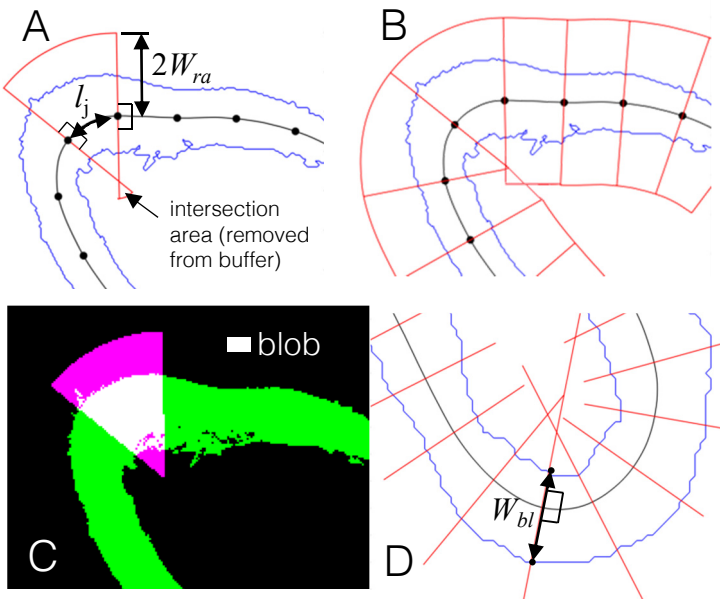

Figure 4.8: The procedures for computing width are illustrated. Average width (W_{avg}) for a segment of river is computed by first drawing buffer boundaries (A). The smooth centerline is shown in black, and the buffer spacings (shown here as 30 pixels) are shown by black dots. In (B), buffer polygons are shown for each spacing. A buffer is overlain on the channel mask in (C). The white area is the blob created by the intersection of the buffer and mask images. The average channel width of the section is the number of blob pixels divided by l_j. A diagram illustrating the computation of channel width from banklines is shown in (D). Channel banks are in blue and the smoothed centerline in black. Perpendicular vectors are shown for every tenth pixel in red.

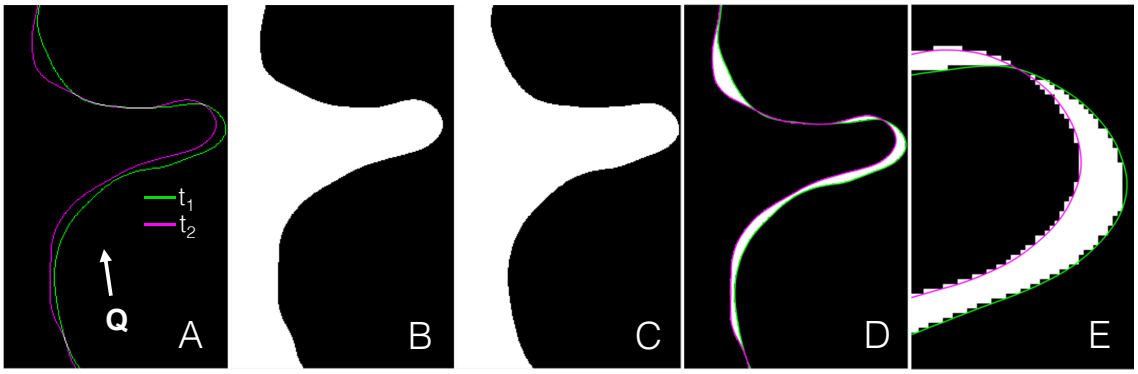

Figure 4.9: The procedure for computing migrated areas from center- or banklines is illustrated for a reach from R5, 1986-1987. In (A), the centerlines at both times are shown. White pixels correspond to their overlap. The filled image halves are shown for t_1 (B) and t_2 (C), and the migrated area found by the union of their differences is shown by the white pixels in (D). A closer look at the migrated area (E) confirms that the t_1 centerline does not contribute to migrated area, while the centerline at t_2 does. The migrated area reflects the modes of bend migration; the bend has translated downstream, rotated slightly, and shortened.

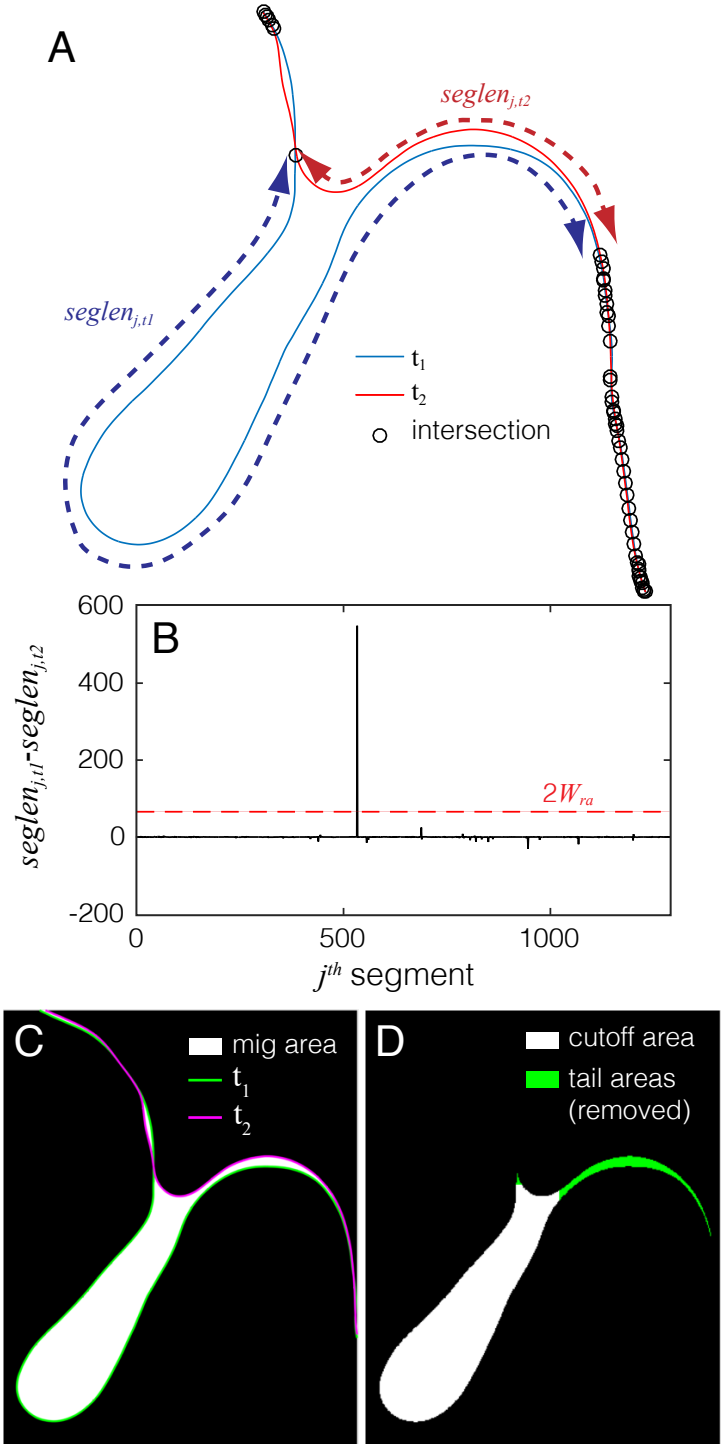

Figure 4.10: (Caption next page.)

Figure 4.10: (Figure previous page.) Procedures for identifying and trimming cutoffs are illustrated. The centerlines of a cutoff bend from R5, 1987 and 1988 are shown with their intersections marked by circles in (A). The segment lengths for the cutoff portion are defined. The difference $seglen_{t_1} - seglen_{t_2}$ for each j^{th} segment is plotted for the entire R5 reach in (B), with the threshold for identifying cutoffs denoted by a dashed line. The peak in this plot at j=533 corresponds to the cutoff bend in (A). The problem of tails is illustrated in (C), where the cutoff area is joined to migrated area. The cutoff area after tail removal is shown in (D).

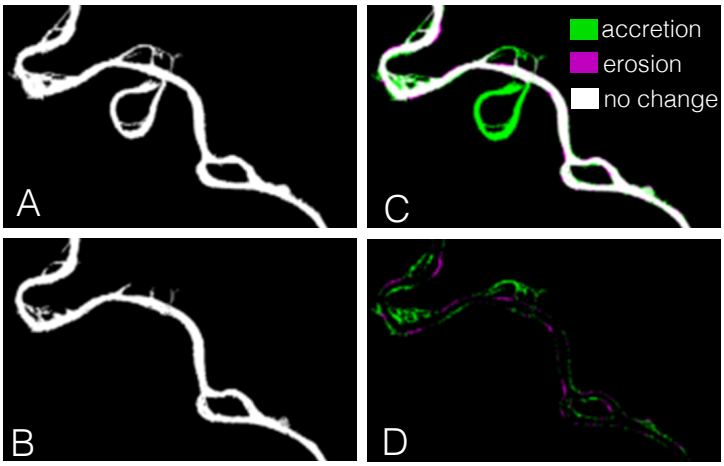

Figure 4.11: Migrated areas are obtained from differencing the hydraulically-connected channel masks for a reach in R4. The masks for 2001 and 2002 are shown in (A) and (B) respectively. Erosion, accretion, and no change areas after mask differencing are shown in (C). Erosion and accretion areas after removing the detected cutoff are shown in (D).

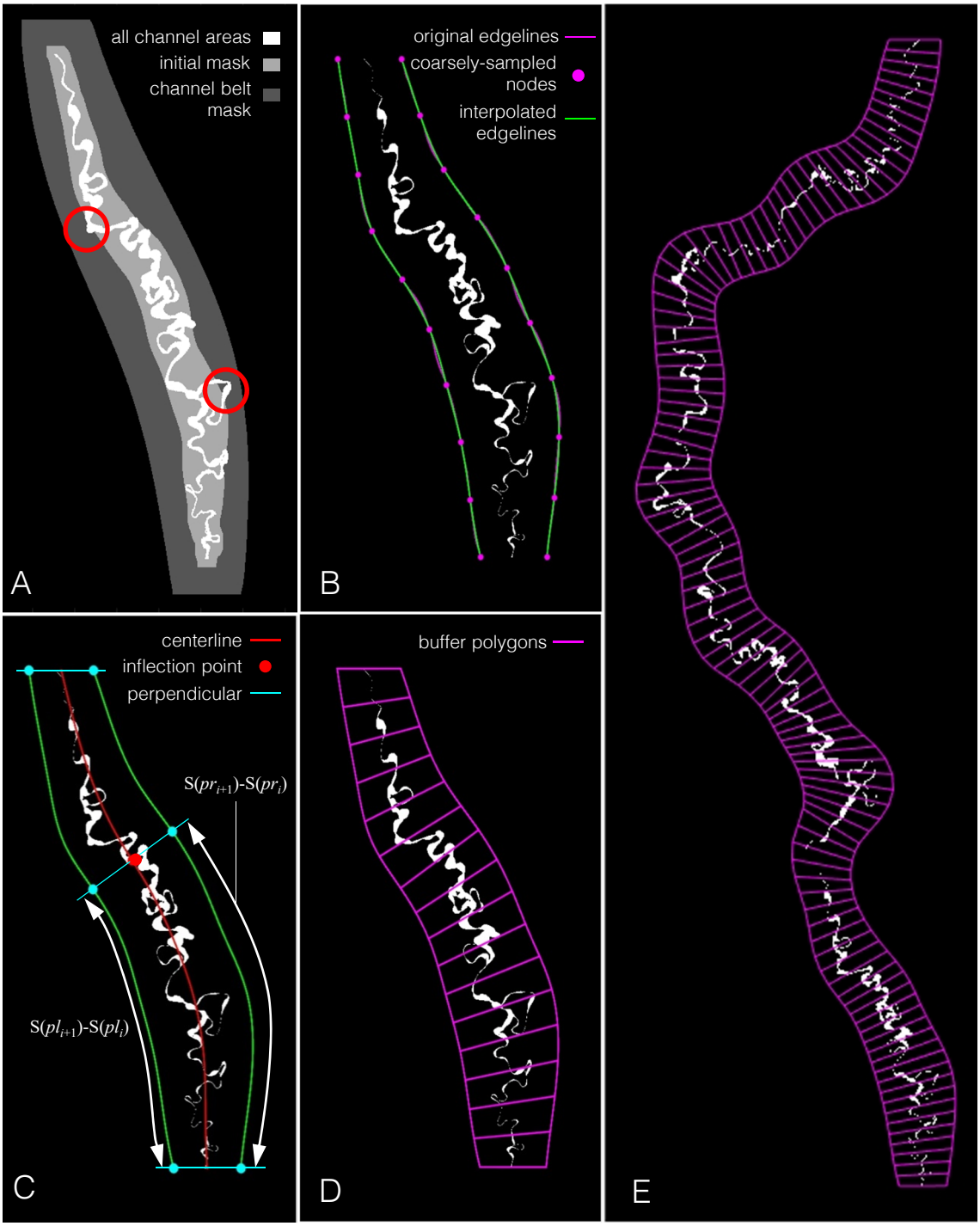

Figure 4.12: (Caption next page.)

Figure 4.12: (Figure previous page.) The procedure for defining a channel belt and creating buffer polygons to quantify changes spatially is illustrated. In (A), all channel positions from R6 are shown from 1985-2015 in white. The initial channel belt mask delineated by oversmoothing the edgelines of the dilated channel mask image is in light gray. The two circles show regions where the initial mask does not capture all the channel positions. Dark gray shows the final channel belt mask that captures all migrated areas. The original and coarsely sampled edgelines are shown in (B). The channel belt centerline and its inflection point are shown in (C) along with the definitions of the lengths used to resample each edgeline. The final buffer polygons are displayed in (D) for R6 with a spacing of $3W_n$ and for the entire reach in (E). Spacing in (E) is $6W_n$ for visualization purposes but can be reliably reduced nearly as far as the resolution of the input image.

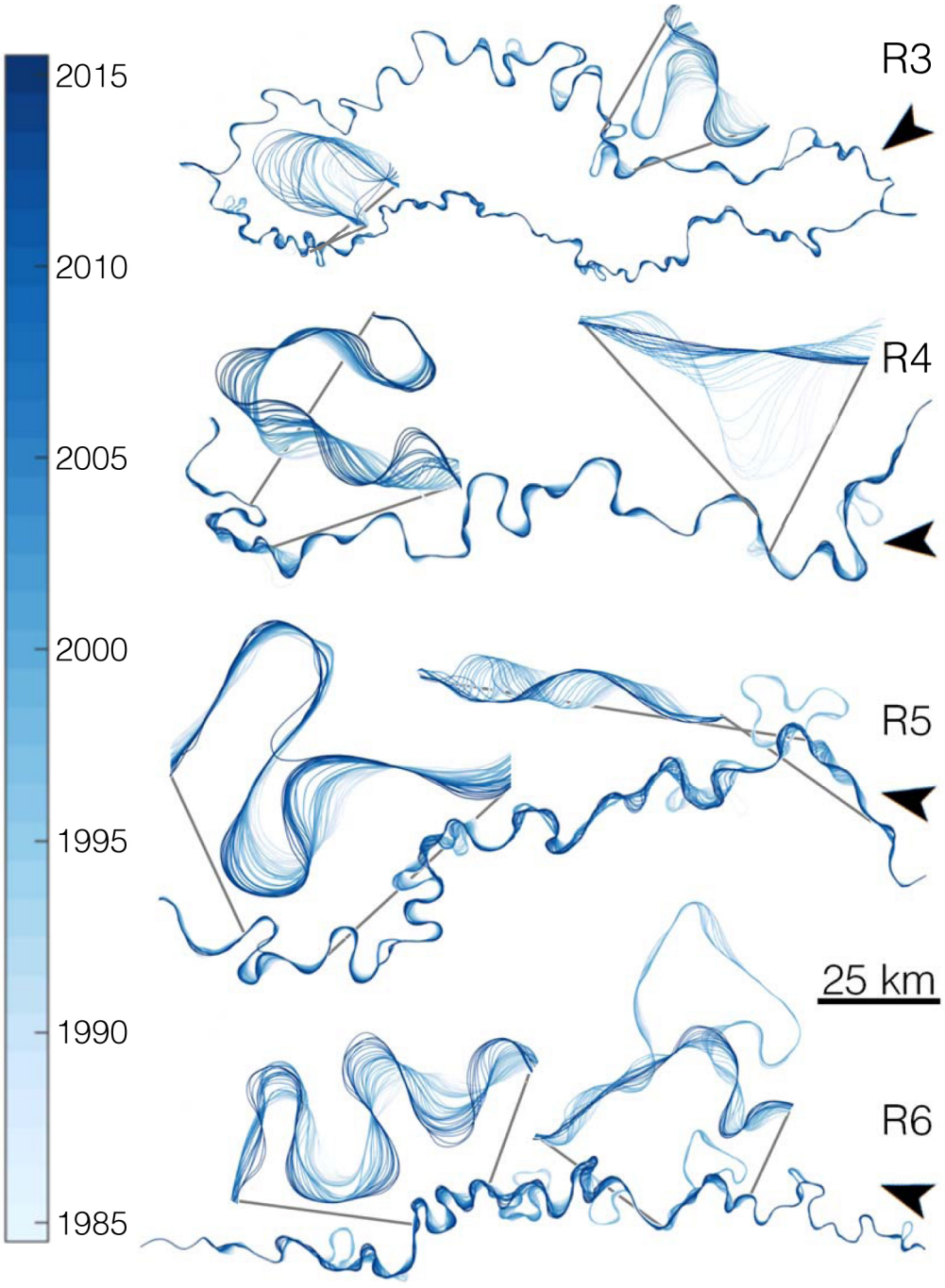

Figure 4.13: (Caption next page.)

Figure 4.13: (Figure previous page.) Centerlines obtained from Landsat-derived single-thread channel masks using RivMAP are shown for the study regions of the Ucayali. North arrows also indicate the direction of flow which travels from R6 to R3. Zoom views highlight some of the complex migration patterns and cutoffs along the Ucayali River. The total centerline length each year is approximately 1,300 km including only the southeastern branch of the avulsion in R3.

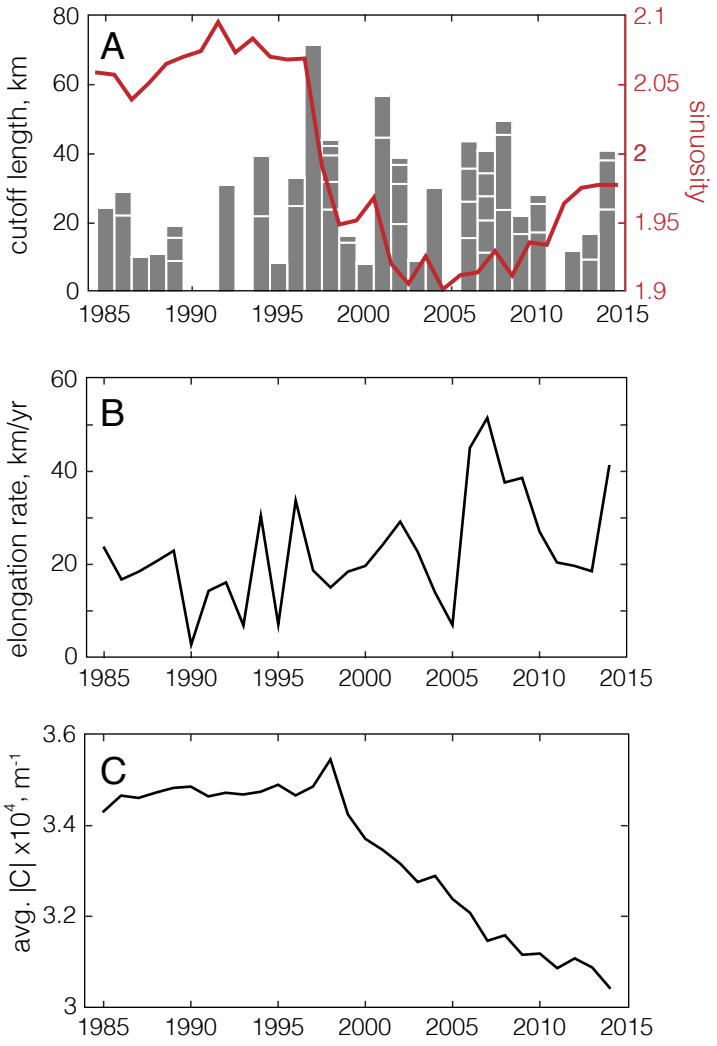

Figure 4.14: Changes in the Ucayali River's centerline length across the 30-year period are illustrated by the sinuosity (A, red line) and cutoff lengths (A, bars). Breaks in the bars (white line) for a given year indicates individual cutoffs which are arranged shortest to longest (bottom to top). The rate of channel elongation for each year is shown in (B), and the evolution of the average absolute curvature for the reach in R4-R6 is shown in (C). The avulsion in R3 was not included in (C).

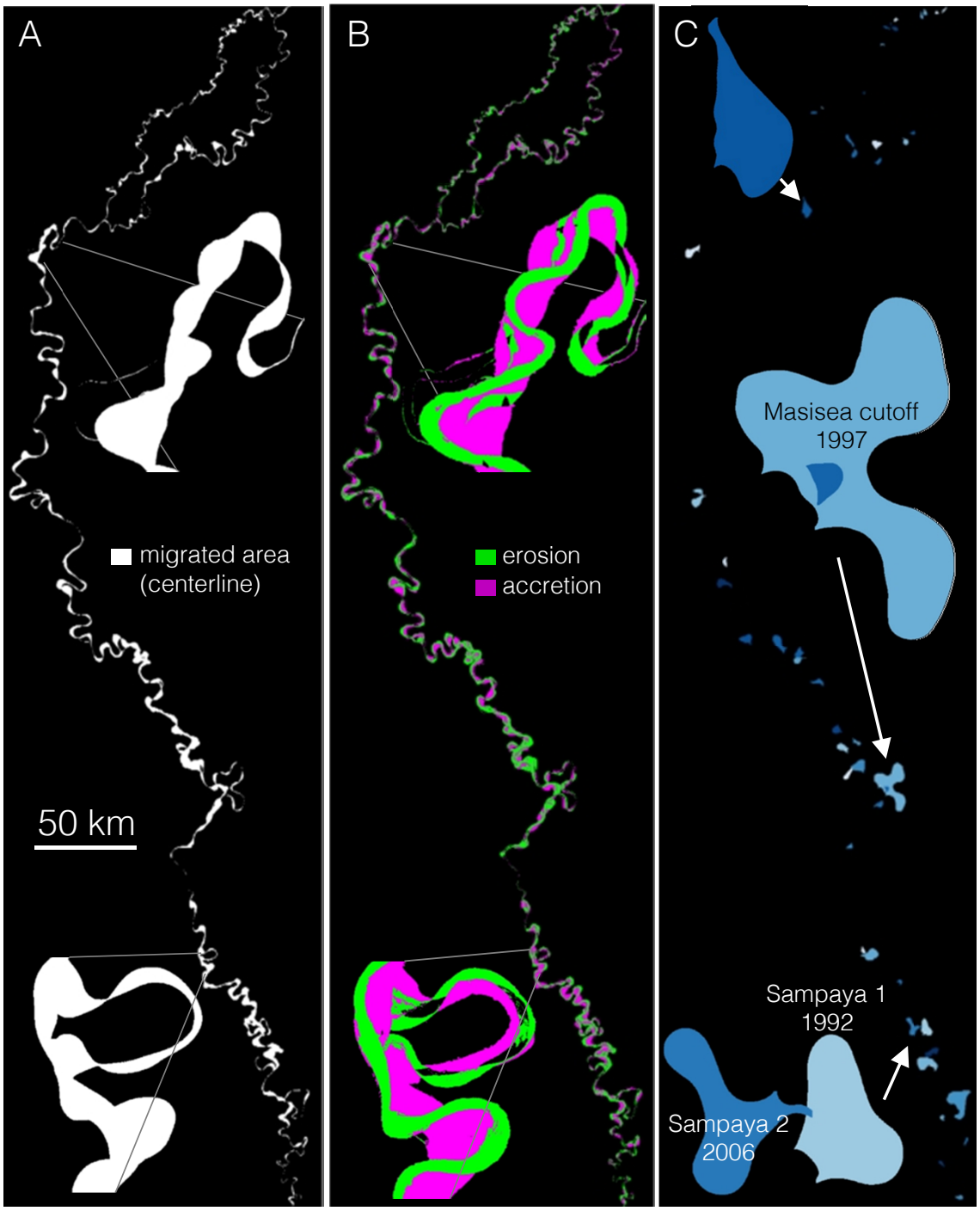

Figure 4.15: (Caption next page.)

Figure 4.15: (Figure previous page.) Migrated area and cutoff maps for the full study reach from 1985-2015 were computed using RivMAP. Centerline migrated areas (A_{cl}) are shown in (A) with two zoom views. Erosion and accretion maps are shown in (B) along with the same zoom views. A pixel may undergo multiple instances of erosion and/or accretion; only the latest occurrence is shown. The 57 cutoffs that occurred from 1985-2015 are shown in (C). Lighter cutoff areas occurred nearer 1985, while darker occurred nearer 2015. The largest cutoff within the study reach (Masisea) is shown in a zoom view, as well as the third and fourth largest (Sampaya 1 and 2).

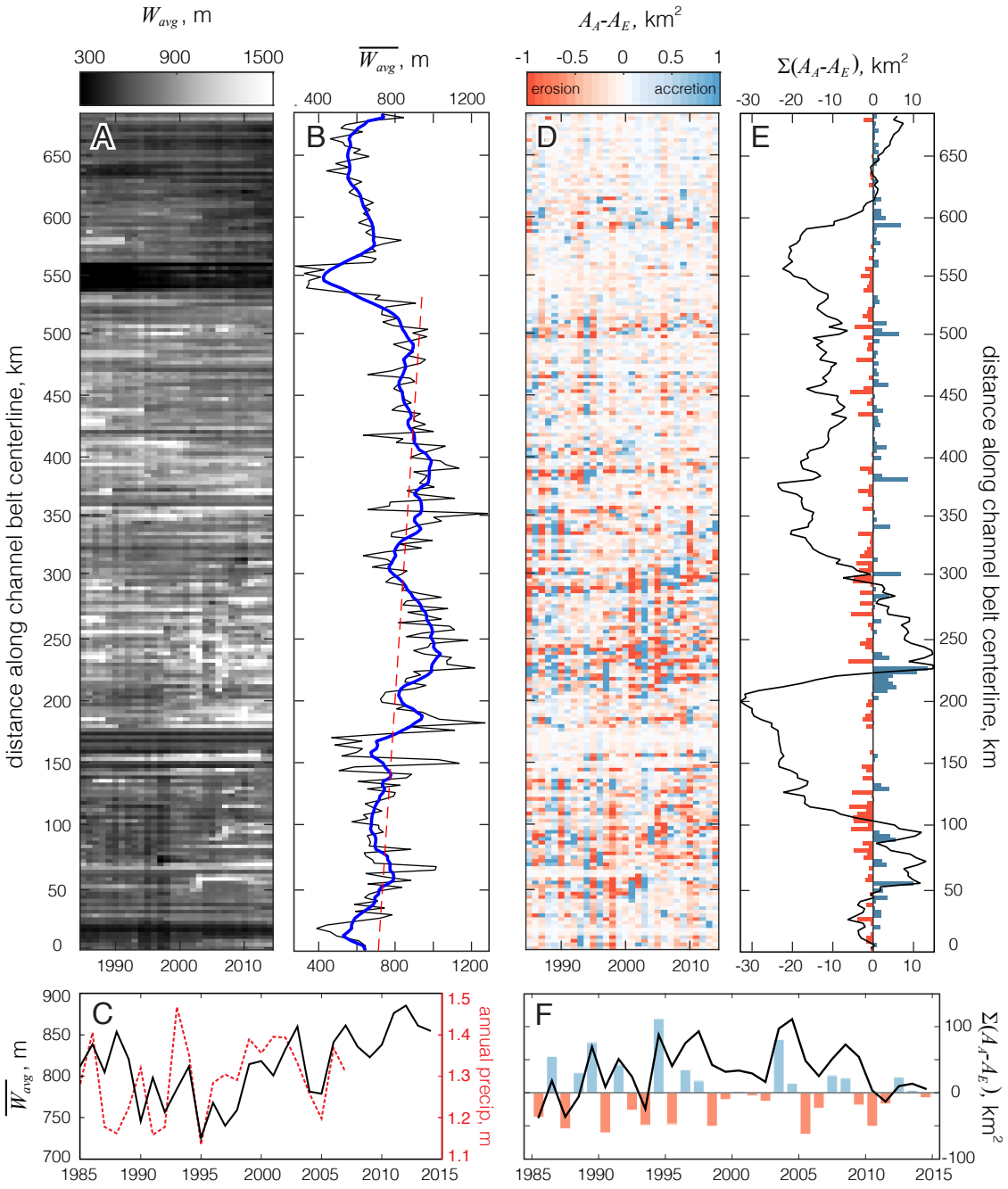

Figure 4.16: (Caption next page.)

Figure 4.16: (Figure previous page.) In (A), the spacetime map of width shows spatial and temporal width variability. Averaging across all 30 years results in the spatial series of average widths (B). The blue line shows a smooth version, and the red dashed line shows the reachwide trend. The time series of average widths is shown in (C) with the regional annual precipitation depths overlaid (dashed red line). The spacetime map of areas of accretion and erosion is shown in (D). Summing areas across all times results in the bars in (E). The black line shows the cumulative reworked area. The time series of annual net erosion/accretion is shown in (F), with the cumulative area overlaid by the black line.

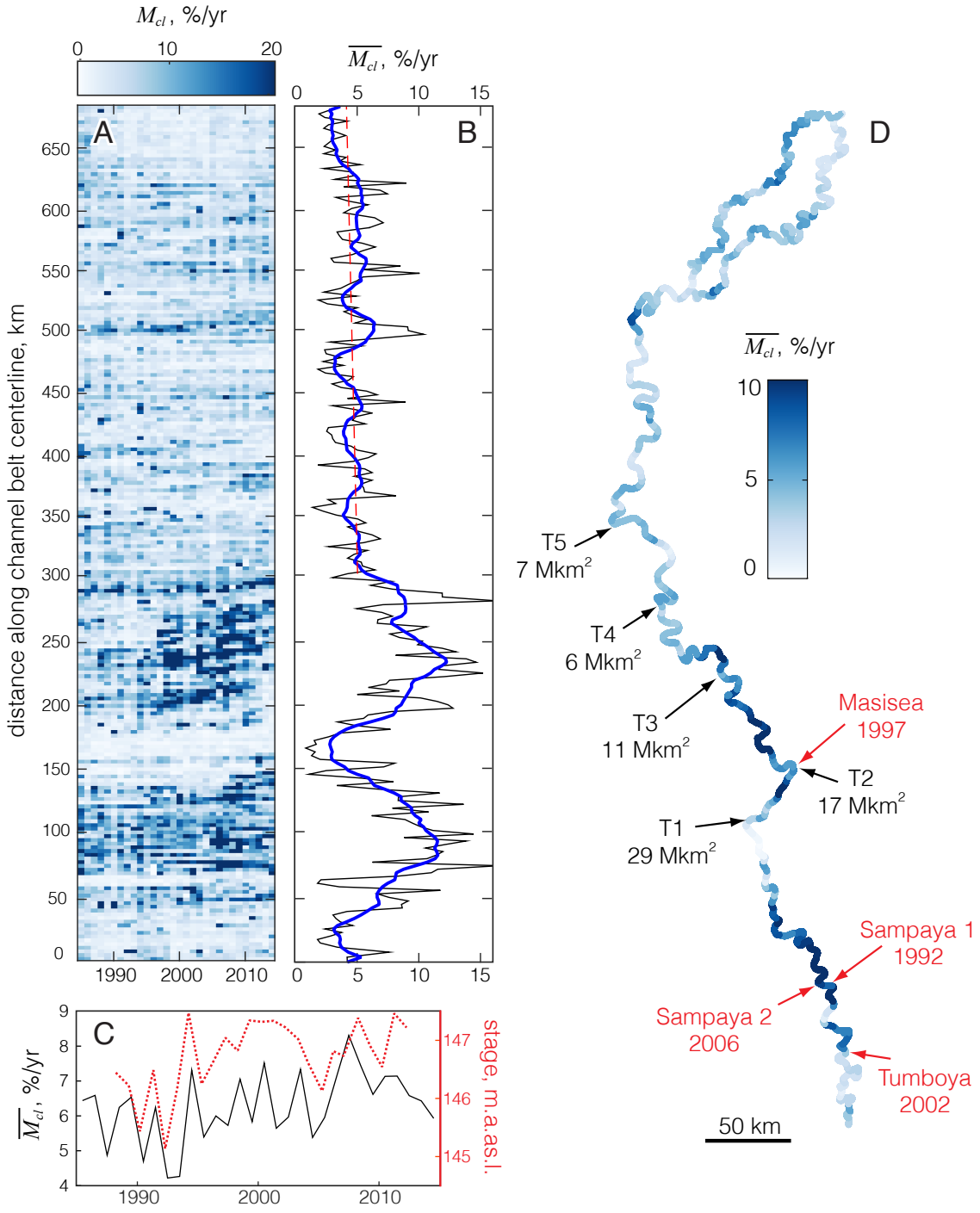

Figure 4.17: (Caption next page.)

Figure 4.17: (Figure previous page.) In (A), the spacetime map of width shows spatial and temporal width variability. Averaging across all 30 years results in the spatial series of average widths (B). The blue line shows a smooth version, and the red dashed line shows the reachwide trend. The time series of average widths is shown in (C) with the regional annual precipitation depths overlaid (dashed red line). The spacetime map of areas of accretion and erosion is shown in (D). Summing areas across all times results in the bars in (E). The black line shows the cumulative reworked area. The time series of annual net erosion/accretion is shown in (F), with the cumulative area overlaid by the black line.

Chapter 5

Cutoffs accelerate nonlocal morphodynamic change

Detailed studies of hydro- and sediment dynamics within and near cutoffs have demonstrated their role as effective agents of local geomorphic change. In this study, we investigate planform morphodynamic changes evidently instigated by cutoffs and show that in addition to local morphologic impacts, cutoffs can act as perturbations that nonlocally accelerate river migration and drive channel widening both up- and downstream of the cutoff event. Annual migration rates and average widths were measured for meander bends adjacent to 12 independent cutoff events along the Ucayali River in Peru to assess the upstream and downstream extents of cutoff influence. For the largest cutoff, migration accelerated after the cutoff as far as 115 channel widths downstream. Regressions show that the downstream distance of cutoff influence scales linearly with the length of the removed reach. The downstream extent of channel widening also scales linearly with the area of floodplain excavated during chute channel formation. This study highlights the necessity of high-temporal-resolution (annual) imagery provided by Landsat satellites toward new geomorphic discoveries and insights on channel response to both natural and human-induced perturbations.

5.1 Introduction

Meander cutoffs play a vital role in river morphodynamics by allowing a channel to adjust its slope and length in response to fluctuations in sediment and water discharges. Unlike adjustments in width, depth, and elongation which are typically spatially- and temporally-continuous, cutoffs are uniquely episodic by removing significant reaches from a river over a short time. Cutoffs may occur "accidentally" as demonstrated by neck cutoff caused by a migrating river simply encountering itself [207] or may form via the development of a chute channel initiated during overbank flow [96]. Cutoffs have long been recognized as important agents of geomorphic change [28, 208, 209]. Over longer time scales, cutoffs influence meander migration rates through the creation of oxbow lakes that augment floodplain resistance heterogeneity. Oxbow lakes form "plugs" through the consolidation of silt, clay, and organic matter that increase local resistance to erosion and impede or confine meander migration [21, 210]. On the other hand, oxbow lakes may also promote meander migration rates if the migrating channel revisits the oxbow before plugs have formed [179]. A study of over 90 years of migration observations along the Sacramento River determined that cutoffs themselves accounted for nearly 20% of the total migration [211].

Over shorter timescales, cutoffs act as "shot" perturbations [58] to river morphodynamics by increasing the bed slope and stream power both up- and downstream [212, 164, 213], injecting downstream pulses of sediment excavated from the floodplain during chute channel formation [214, 165], and substantially altering the local channel planform and hydrodynamics [164, 215]. Considerable attention has been given to local cutoff-induced channel response immediately adjacent to and within cutoffs [216, 214, 165, 215] as well as factors controlling their occurrence [217, 218, 219]. However, the spatial and temporal extents to which cutoff perturbations induce nonlocal morphologic change remains unknown, largely due to difficulties observing morphodynamics at spatial and temporal scales sufficient to capture changes. Here we consider migration rate and channel width as indicators of morphodynamic change and tap into over three decades of global satellite imagery to investigate how cutoff perturbations influence up- and downstream morphodynamic change along the active tropical Ucayali River in Peru.

5.2 Methods

5.2.1 Study River

This study investigated morphodynamic response to 13 cutoffs along the Ucayali River in Peru using annual channel masks obtained from 31 years of Landsat imagery. The Ucayali River is within the Amazon Basin, flowing north along the eastern flank of the Andes Mountains, and together with the Marañon River forms the headwaters of the Amazon River. Among major rivers in the Amazon Basin, the Ucayali's migration pace is second only to the Mamoré River with an average rate of 36 m/yr [178]. The Ucayali's floodplain testifies to its impressive action with its oxbow lakes, abandoned channels, scroll bars, and sediment splays. Within the 1985-2015 window of available Landsat imagery of the Ucayali River over 50 cutoffs occurred, removing lengths of river ranging from 5-89 channel widths. Of these cutoffs, 17 were pure neck cutoffs, 17 were chute cutoffs, and 8 were "tip" cutoffs where the primary flow path bypassed only the apex of the meander bend. Chute cutoffs may span multiple years from initial chute formation to complete bend disconnection, and for some cutoffs the meander bends were never completely hydraulically disconnected. Only chute and neck cutoffs that completed within two years were considered. Additionally, cutoffs occurring near others in space and time were not considered so that measured morphodynamic changes were attributable to single cutoff events. Eight chute cutoffs and five neck cutoffs met these criteria; their characteristics are listed in Table 5.1.

5.2.2 Individual Bend Tracking

The influence of cutoffs on morphodynamics was investigated through the migration rates and widths of individual meander bends adjacent to each cutoff. If the bend immediately downstream of a cutoff exhibited accelerated morphodynamic change after the cutoff occurred, its neighboring downstream bend was also analyzed until the first bend with no appreciable changes (defined later) was encountered. Measuring morphodynamic properties of individual meander bends required their consistent delineation through time.

Meander bend endpoints were initialized from centerline inflection points at the time of cutoff. Both bend endpoints were tracked forward (backward) through time by mapping them to the next (previous) year's centerline. A point along the centerline at t_1 was

mapped onto the t_2 centerline by minimizing the error between its position (i.e. x,y coordinate), direction, curvature, and width between both centerlines. Nearby cutoffs typically dramatically altered these local channel properties due to required smoothing. Therefore if a cutoff occurred near a point being mapped, only the point's position was used to map it into the next time, thereby preventing artificial bend endpoint jumps following cutoffs.

5.2.3 Migration Rates and Excavated Areas

Annual binary channel masks capturing the bankfull planform of the Ucayali River were generated by combining classified Landsat images collected from 1985-2015. A detailed description of the process is given in [130]. The RivMAP toolbox [130] was used to compute centerlines, identify cutoffs, and measure migration rates. Bend migration rates were computed annually by

$$M_r = \frac{A_{cl}}{l_{cl}(\Delta t)} \tag{5.1}$$

where A_{cl} is the area traversed by a bend's centerline over period , l_{cl} is the length of the bend at the beginning of the period, and $\triangle t$ is one year.

The quantity of sediment injected into downstream reaches from floodplain incision during chute channel initiation and development was estimated from the binary channel masks. The mask from the first year before the chute cutoff appeared was subtracted from the mask of the year of complete cutoff. Differenced masks were cropped to the region of cutoff leaving only the area excavated by the chute channel (A_{es}).

5.3 Results

The 1997 Masisea cutoff marked the most drastic change in the course of the Ucayali River in over 200 years with the removal a 72 km triple-lobed meander bend. The cutoff's anthropogenic origins are attributed to local ribereños, who in effort to reduce canoe travel time along the river carved a meter deep by two meters wide shortcut channel across the neck of the Masisea bend. Modest efforts in the 1980s to enlarge the channel culminated in using a tractor to widen its entrance, and the Ucayali commandeered the tiny channel during the following 1997 flooding season [191]. The river's morphodynamic response to

the Masisea cutoff is evident from the shift in up- and downstream bend migration rates and widths following the cutoff (Figure 5.3). In the downstream direction, bends D1-D8 migrated faster and D1-D4 widened following the cutoff. Upstream of the Masisea cutoff, three small-amplitude bends experienced accelerated downstream translation and widening after the cutoff. Morphodynamic changes due to the Masisea cutoff spurred the eventual cutoff of bends U1, D1, D4, and D5, while bends downstream of the Masisea cutoff that had not yet themselves cut off (i.e. D6-D9) exhibited elevated migration rates sustained for over a decade following the cutoff. Similarly, the upstream bends U3 and U4 underwent persistent widening following the cutoff.

Changes in climate, floodplain heterogeneity, sediment loads, or land use may drive morphodynamic fluctuations, including those observed near the Masisea cutoff. Results from 12 additional cutoffs from different years and locations along the Ucayali indicate that cutoffs controlled accelerated morphodynamic change. Pre- and post-cutoff migration rates (M_{cl}) and average bend widths (W) were obtained for bends adjacent to each cutoff by averaging their values over the two years preceding cutoff and two years afterward. The year of cutoff itself (red bars in Figure 5.3) was not included in averaging because the channel planform for that year integrates effects of both pre- and post-cutoff dynamics.

Significant difference between pre- and post-cutoff morphodynamics was inferred for M_{cl} and W of a bend only if the following conditions were met:

$$\frac{M_{cl,post} - M_{cl,pre}}{M_{cl,pre}} > 0.25,\ M_{cl,post} - M_{cl,pre} > 2\frac{m}{yr}$$

and

$$\frac{W_{post} - W_{pre}}{W_{pre}} > 0.05,\ W_{post} - W_{pre} > 30m.$$

The former conditions require at least a 25% (5%) increase in migration rate (width), and the latter conditions ensure that the increases exceed uncertainties inherent in quantifying planform changes from Landsat imagery (0.5 m/yr for M_{cl} and 15 m for W, [130]). The distance of downstream influence on migration rates (D_M) and width (D_W) of each cutoff was defined as the centerline distance from the downstream end of the cutoff reach to the downstream end of the farthest bend that met the above criteria.

Downstream meander bends migrated at least 25% more rapidly following cutoffs at 11 of 13 sites (Figure 5.4), and a regression between D_M and the change in river length following cutoff (ΔL) indicates that the downstream extent of accelerated migration due to cutoff along the Ucayali scales with the length of cutoff river. Migration rates for the first downstream bends at the two sites 'Mn' and 'Tr' with no significant downstream influence did increase by 10% and 15%, respectively, but were already relatively inactive prior to cutoff. Seven cutoffs effected increased migration at distances longer than the length of removed river (ΔL). Excavated area (A_{ex}) poorly predicted D_M, indicating that although sediment pulses due to floodplain excavation during cutoff promote morphodynamic change, they do not control the spatial extent of accelerated migration. As expected, neck cutoffs resulted in smaller excavated floodplain areas than chute cutoffs but were nonzero, reflecting local erosion that occurred immediately following the bridging of the cutoff neck as the river straightened the resulting sharply-curved bend.

Significant downstream channel widening after cutoffs occurred at 8 of 13 sites (Figure 5.5). Results suggest that the downstream spatial extent of channel widening is partly controlled by aggradation due to sediment pulses generated via chute channel formation. The change in river length (ΔL) had little explanatory power on D_W. The outlying Éxito (Ex) cutoff was not considered in the regressions. Éxito was immediately downstream of and occurred only five years after the Masisea cutoff (bend D1 in Figure 5.2). Its exceptionally large D_W likely reflects the reach's instability to additional perturbations as it approached a new post-Masisea equilibrium.

5.4 Discussion

The impact of cutoffs on immediate and nonlocal river morphodynamics has been acknowledged [55, 164, 215] yet no previous studies have documented the spatial and temporal morphodynamic influence of specific cutoff perturbations. Extensive downstream planform adjustments following cutoff at all thirteen sites along the Ucayali River reveals the role of cutoffs as nonlocal drivers of accelerated morphodynamics that can influence channel evolution as far as 115 channel widths downstream and 30 channel widths upstream. Channel migration in the Ucayali is driven by its sediment load [178, 130], and enhanced

downstream sediment flux due to cutoff likely accounts for the bulk of accelerated migration and bend widening. Although initial pulses of sediment due to chute formation do not explain the spatial extents of accelerated migration, diffusion of the locally-steep bed elevation following cutoff may result in a more continuous sediment supply over a longer time period [220, 212]. Changes in slope are typically the initially-dominant morphodynamic response to cutoffs in alluvial rivers, and may cause an immediate backwater effect upstream of the cutoff. As the slope perturbation diffuses up- and downstream over a period of years, the upstream bed scours, releasing sediment to the downstream reach which may drive morphodynamic change [221, 218]. The magnitude of the slope perturbation following cutoff is proportional to ΔL, which accounted for 75% of the variation of D_M for 12 cutoffs in the Ucayali River. In addition to sediment released from the upstream bed during reestablishment of an equilibrium slope, the reach immediately downstream may also receive larger water and sediment loads relative to pre-cutoff conditions due to the river's loss of floodplain storage and/or synchronization with local inputs [208]. The magnitude of the loss of storage depends on local floodplain topography, flow conditions, and channel geometry but can be expected to also scale with $\triangle L$.

The Ucayali's response to cutoff perturbations reveals elongation as the preferential mode of self-adjustment. With the exception of the downstream-translating U1-U3 bends at Masisea, accelerated migration indicated bend growth. Morphodynamic response to 12 independent cutoffs shows that the Ucayali River was more likely to lengthen (10/12 bends) than widen (7/12 bends) following cutoff perturbations, and that downstream extent of channel lengthening due to cutoff was often greater than the extent of widening. The Ucayali's preference to self-adjust its length to a greater extent than its width might suggest its return to a dynamic equilibrium is controlled by the diffusing bed slope rather than increased downstream sediment flux.

The nonlocal acceleration of planform change of the Ucayali cutoffs, and in particular the Masisea cutoff, provides perhaps the strongest support yet for considering meandering river planform dynamics as self-organized critical (SOC) systems [125] that maintain critical stable states [55, 126, 164]. The classic SOC system is the rice pile, which builds to a critical state at which point adding a single grain may result in avalanching. The "river rice pile" analogy might consider the incremental migration of the river at a dynamical steady state

as individual grains of rice, and cutoff events clustered in space and time as avalanches. The clustering of cutoff events implies that a single cutoff event is likely to induce further cutoffs nearby, a response requiring 1) available bends to cut off (high local sinuosity) and 2) a physical mechanism through which the cutoff perturbation is nonlocally manifest. Previous studies have found power-law scaling, a feature of SOC systems, in oxbow lake sizes and sinuous clusters from numerical models of long-time meander evolution [55, 126]. Cutoff clusters in real rivers over short time periods have also been observed [164], but until this study no evidence had linked cutoff events to nonlocal morphodynamic change required to initiate and sustain SOC-type avalanching.

5.5 Conclusions

The planform response of the Ucayali River to 12 independent cutoff events establishes cutoffs as morphodynamics perturbations with nonlocal influence and presents a new modeling and theoretical challenge. The physical mechanisms responsible for channel widening and accelerated migration following cutoffs are not immediately discernable from planform dynamics alone, although the spatial extent of cutoff influence on migration (D_M) and width (D_W) provide hints. Both quantities scaled with the length of reach removed ($\triangle L$), which is directly proportional to the bed slope perturbation and roughly proportional to the loss of floodplain storage area. The downstream extent of channel widening was also dependent on the initial sediment pulse released during the initial chute channel incision. Repeated bathymetry surveys and sediment sampling before and after cutoff at high temporal resolution may be required to fully understand the physical mechanisms driving accelerated planform changes. The Ucayali River "authored its own geometry" following cutoff by preferentially adjusting its length moreso than its width. Channel response to cutoff perturbations are likely to vary based on sediment, floodplain, and morphology characteristics, and in some cases planform changes may not occur, but these results show that cutoffs can play a vital and controlling role on the long-term morphodynamics of migrating rivers.

Figure 5.1: Thirteen cutoff events along the Ucayali River are shown midway through the cutoff process and at low flow. Cutoff channels and flow directions are denoted by white arrows. The north arrow and scale bar apply to all images.

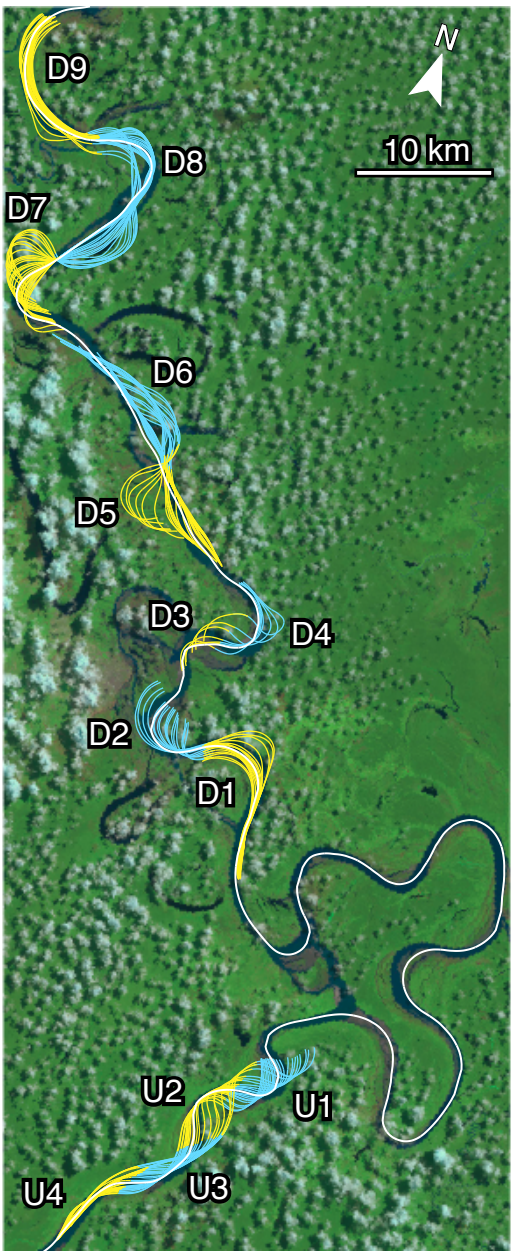

Figure 5.2: Individual bends up- and downstream of Masisea are shown. The bend labels correspond to those shown in Figure 5.3. The 1997 centerline (the year of cutoff) is shown in white.

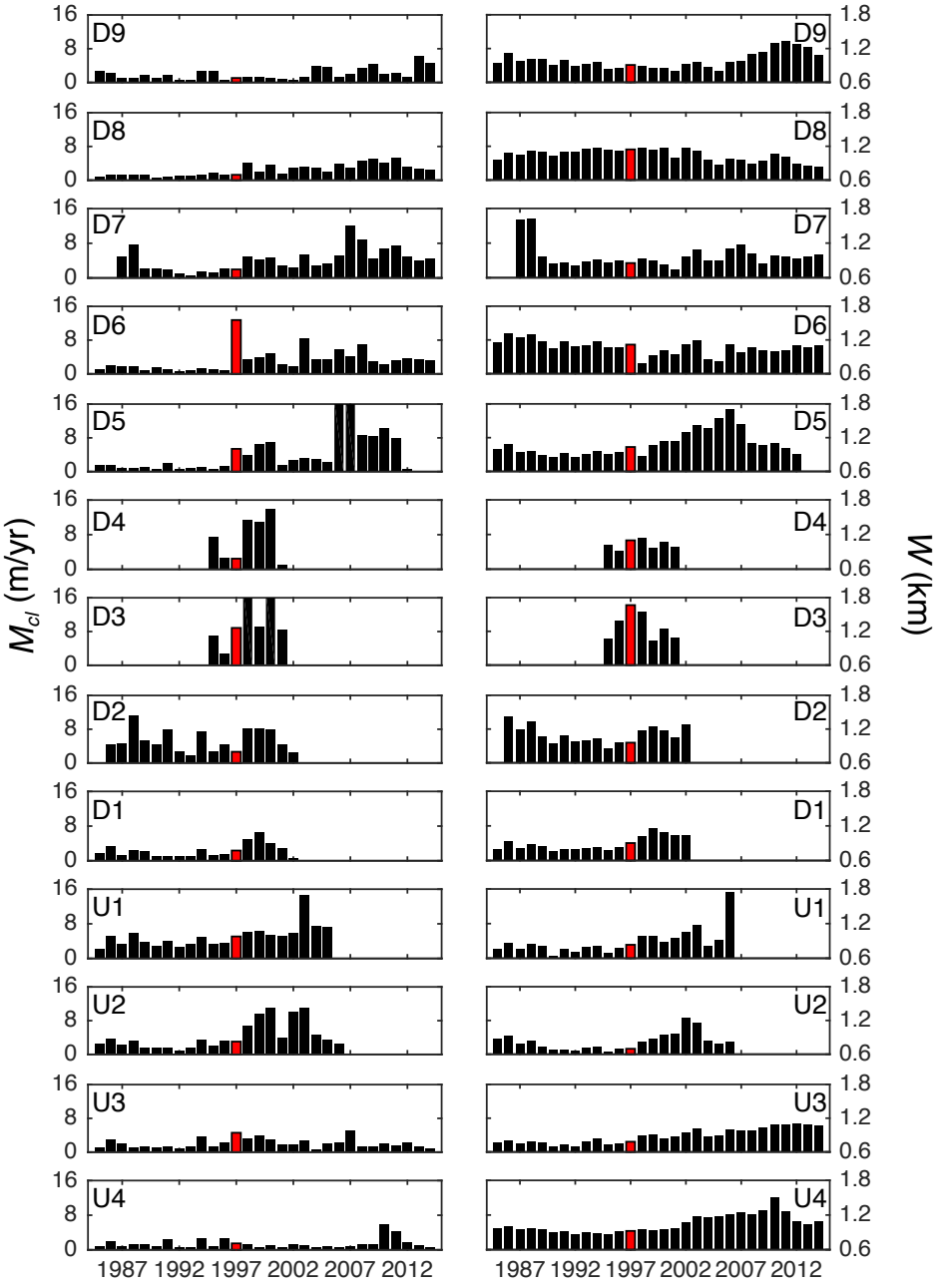

Figure 5.3: Migration rates (M_{cl}, left panel) and widths (W, right panel) for the individual bends shown in Figure 5.2 are plotted through time. The red bars highlight the year of the Masisea cutoff.

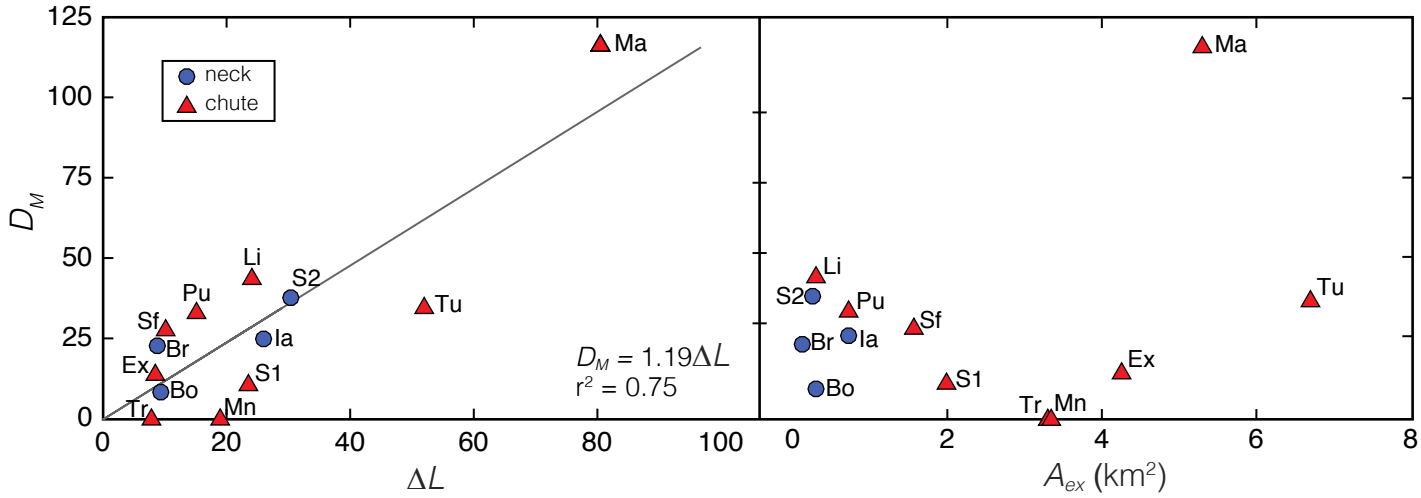

Figure 5.4: The distance downstream from each cutoff to the limit of accelerated migration (D_M) is plotted against the change in river length due to cutoff (ΔL) and the area of excavated floodplain (A_{ex}).

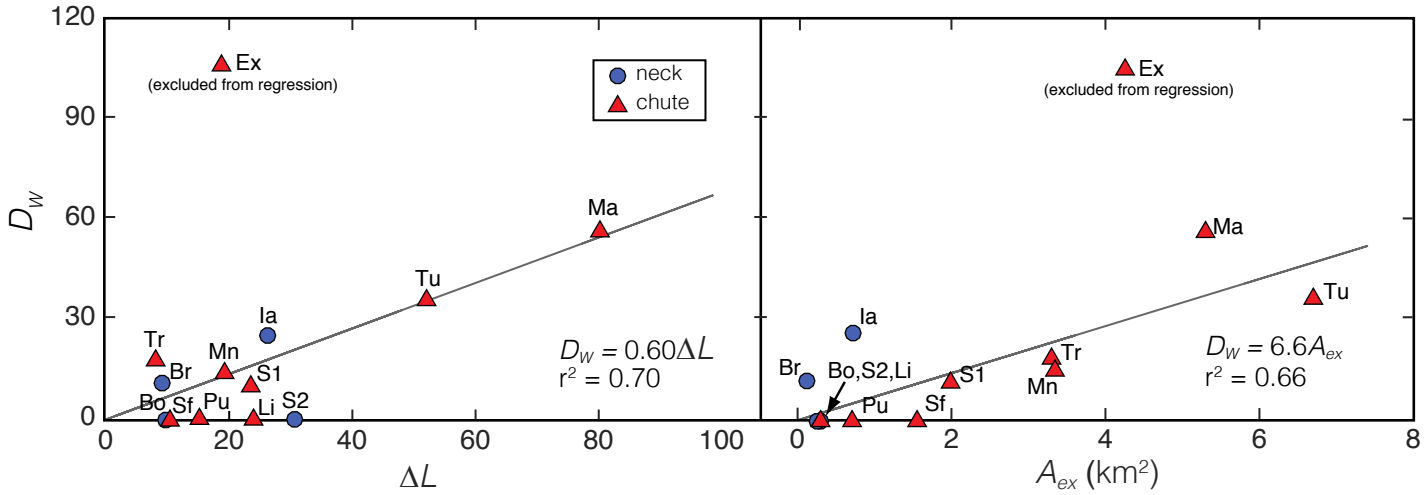

Figure 5.5: The distance downstream from each cutoff to the limit of channel widening (D_W) is plotted against the change in river length due to cutoff ($\triangle$L) and the area of excavated floodplain.

Cutoff	Label	Latitude °	Longitude °	Year	Length (km)	Type	Chute Length km	Width m	Excavated Area km^2
Masisea	Ma	-8.511	-74.316	1997	72	chute	7.0	837	5.3
Tumboya	Tu	-9.883	-74.012	2001	51	chute	8.9	767	6.7
Sampaya 2	S2	-9.550	-74.185	2004	28	neck	2.9	791	0.25
Libertad	Li	-7.240	-75.118	1994	27	neck	7.8	949	0.22
Manchari	Mn	-9.706	-74.127	1998	24	chute	8.6	697	3.3
Iaparia	Ia	-9.242	-74.434	1998	23	neck	1.4	623	0.72
Sampaya 1	S1	-9.566	-74.168	1992	22	chute	2.7	568	2.0
Pucallpa	Pu	-8.348	-74.508	1994	15	chute	2.4	915	0.73
Éxito	Ex	-8.458	-74.434	2002	15	chute	8.1	1020	4.3
San Francisco	Sf	-7.935	-74.935	1999	12	chute	3.2	915	1.6
Tre Unidas	Tr	-8.258	-74.535	2012	11	chute	4.3	769	3.3
Bolognesi	Bo	-10.046	-73.977	2006	9.6	neck	1.5	675	0.29
Bretaña	Br	-5.125	-74.321	2010	8.3	neck	0.67	470	0.13

Table 5.1: Characteristics of the 13 cutoffs analyzed herein. Chute length is measured as the distance along the post-cutoff centerline between the intersection of the pre- and post-cutoff centerlines. Width is reported as the average cutoff bend bankfull width during the year immediately preceding its removal. Excavated area is explained in the text.

Chapter 6

Conclusions and Future Perspectives

While the basic underlying physical theory of meander migration has been well-established (e.g. [2, 41, 60], predicting channel locations over intermediate time scales (decades) via meander migration models has remained inadequate. Lack of predictive power may stem from a number of sources; first, meander migration may be sensitive to initial conditions. Second, the multiscale heterogeneities in natural rivers from tiny scales of turbulence to large cutoffs coupled with unsteady autogenic forcings through climate shifts and sediment production, along with variability in floodplain resistance, are impossible to fully account for in models of long-time meander migration. And finally, there may be yet-undiscovered processes at play.

This research contributed a deeper understanding of how and why rivers move about their floodplains and made progress toward each of the factors that diminish our predictive capabilities. In Chapter 2, the eventual dynamic lives of individual meander bends were shown to be somewhat dependent on the planform configuration at the time of their inception. Chapter 4 demonstrated the spatial and temporal scales of variability in planform adjustments and showed that changes may be driven by floodplain resistance, tributaries, cutoffs, climate, or proximity to sediment production zones. Responses to each of these controls may be local (spanning a single bend), nonlocal (multiple bends), or reachwide, and attributing causative factors to observed changes requires resolving channel positions

at a frequency equal to or less than that of the shortest driver of change. In Chapter 5, the annually-resolved planform positions of the Ucayali River revealed a previously-unreported role of cutoffs as agents of nonlocal morphodynamic change. The main results of this thesis are summarized in detail below.

Conclusions

1. Physically-based numerical modeling of long-time meander evolution showed that the autogenic processes of meander bend formation and evolution, i.e. curvature-driven dynamics and cutoffs, are imprinted in their geometries such that bends with similar cutoff geometries share similar dynamic histories. In other words, in the absence of unsteady allogenic forcings and heterogeneous floodplain resistance, there is hope that historic dynamics may be reconstructed from oxbow planforms alone. Following individual bends (called atoms) from their inception until cutoff revealed that, in the absence of external perturbations, the dynamic trajectory of an atom is set by conditions early in its life. The most revealing metrics of meander bend geometry are maximum curvature and efficiency ratio (bend area/ bend length); cutoff atoms with higher maximum curvatures and lower efficiency ratios were found to migrate fastest. The work also revealed an archetypal atom geometry embedded in the model dynamics; without the effect of cutoff perturbations meander bend geometry would be remarkably homogeneous.

2. Previous research had identified many process-based nonlinearites governing the in-channel dynamics of meander evolution, yet the imprint of these nonlinearities was curiously absent in the spatial structure of longer meander trains. Using a robust metric of nonlinearity, the curvature series of natural meandering rivers were demonstrated to contain nonlinear structure. Even the simplest physically-based model of meander migration was shown to embed nonlinearity in simulated planforms. The degree of nonlinearity (DNL) for the simulated river attained a maximum prior to cutoffs, and reached a steady-state a short time after cutoffs were active, implicating cutoffs as destroyers of nonlinear structure through the removal of older and fully-developed bends that have had sufficient time to manifest the driving dynamic nonlinearities. A wavelet-based analysis identified the scales contributing to nonlinearity and showed

that prior to cutoff, the fully-developed bends were the primary contributors. After cutoffs had occurred, the range of scales in the centerline grew as "birth" scales were introduced following cutoffs and "superdeveloped" scales formed as the centerline developed low-frequency modulations (also made possible by cutoffs). Both the birth and superdeveloped scales contributed to nonlinearity, suggesting that while cutoffs overall role was to reduce nonlinear structure, they also promote nonlinearity within the centerline. The magnitude of change of DNL in an evolving natural river showed that the decrease in DNL was not simply proportional to cutoff size; DNL was also sensitive to the location of the cutoff bend relative to other bends in the meander train.

3. Landsat imagery contains the potential to reveal the lives of not just meander bends, but entire rivers. Studies of meander migration have long-suffered from a lack of observations of intermediate planform adjustments. While only 32 years of worldwide Landsat data are currently available, imagery of the large, active rivers in the tropical Amazon reveals the previously-hidden lives of rivers' migrations and provide a new source of insight for understanding spatial and temporal controls on migration rates. As a proof-of-concept, the Ucayali River was shown to contain multiple scales of variability driven by climate, nearby sediment production zones, tributaries, cutoffs, and at the smallest scale, local bend morphology and bank resistance.

4. A new geomorphic phenomenon was observed and quantified, made possible only through the annual planform analysis described in Chapter 4. Eleven of thirteen cutoffs were shown to effect morphodynamic change non-locally, i.e. accelerating migration up to 115 channel widths downstream and 30 channel widths upstream. The spatial extent of cutoff-induced accelerated migration scaled with the change in river length due to cutoff, and had little correlation with the excavated area. Downstream channel widening following cutoff events was observed in 8/13 cutoffs, and the downstream extent of widening was generally shorter than that of accelerated migration. Results suggest that the Ucayali preferentially adjusts its length (elongation) over widening following perturbations due to cutoffs, and provide insight into channel self-adjustment modes and mechanisms.

5. Two software packages were released to the community as a result of this research: the long-time model of meander migration and a function to track individual meander bends (atoms) from numerical models were made available as Matlab codes, and the RivMAP tools described in Chapter 4 for mapping and measuring planform changes over short time intervals and long time periods. Both packages are freely available: the atom tracking method was included as supplementary information in [146] and RivMAP may be downloaded at `https://www.mathworks.com/matlabcentral/fileexchange/58264-rivmap-river-morphodynamics-from-analysis-of-planforms`. Additional unreleased tools were developed for analyzing morphodynamics of individual meander bends obtained from natural rivers and may be included into RivMAP eventually.

Future research

Research often generates more questions than answers, and the work represented in this thesis was no exception. Listed here are open research questions encountered while developing this dissertation.

1. The degree of nonlinearity (DNL) was established as a reachwide metric that measures, to some degree, the manifestation of dynamic nonlinearities through channel planform morphology. Currently, DNL has no intuitive interpretation as compared to other reachwide metrics, e.g. sinuosity which measures the "wiggliness" of a river. However, a foundation toward building such intuition was laid in Chapter 3, where the simplest, physically-based long-time model of meander migration revealed the inherent, autogenic nonlinearities associated with meandering, providing a baseline for future comparisons. Incrementally increasing model complexity by including, for example, explicit bank erosion models (e.g. [106]) or allowing banks to evolve independently (e.g. [64]) would allow changes in the resulting planforms' DNL to be mapped to particular dynamic processes. The DNL may then serve as a powerful metric for interpreting process from form.

2. The Transportation Distance (TD) metric provided a robust and effective measurement of the difference in phase space between a meandering river planform and its linear surrogate. However, TD does not measure the trajectories within the phase space, and therefore has no predictive power. Although the attractor structure of both real and simulated rivers was demonstrated to reflect the underlying dynamic nonlinearities, the next step is to model the trajectories themselves within phase space. Modeled and natural rivers have been reported to be non-chaotic [53], but other phase-space models may capture the downstream evolution of meandering rivers. Such models would offer theoretical insight, such as sensitivity to perturbations, into the driving dynamics of river meandering.

3. Planform curvature is perhaps the most commonly-used characterization of downstream meander planform geometry, yet as a second-derivative measure curvature signals are often very noisy and require filtering. Smoothing and filtering alter the statistics of the curvature signal (i.e. first- and second-order moments) and, depending on the bandpass frequencies of the filter can substantially alter the signal itself. Curvature signals obtained from different sources (e.g. satellite imagery or hand-traced from aerial photography) are therefore difficult to compare meaningfully. Curvatures computed for rivers at different scales require disparate filters due to their different wavelengths, and the comparison of curvature statistics between rivers becomes questionable. Given the ubiquity of curvature-driven models (including the one presented in Chapter 2) and curvature-based empirical analyses (like that in Chapter 3), a standardized technique for obtaining smooth planform curvatures (or a similar metric) should be developed.

4. The dataset of annual Ucayali River bankfull planforms compiled from Landsat imagery presented in Chapter 4 contains yet-unrealized potential to shed light on many questions. Specifically, the relationship between migration rates and geometry established in Chapter 2 has not been examined in the Ucayali River. The relationship between centerline curvature and migration rate reported for some alluvial rivers [115, 222] may not be valid in large, sand-bedded rivers and should be evaluated. The dataset may also be used to characterize floodplain visitation probabilities and timescales for use in, for example, parameterizing valley evolution models. Annual

realizations of channel positions over 31 years also provides a basis for quantifying a Sadler-type effect in meandering rivers, where migration rates are underestimated as the elapsed time between realizations grows due to channel revisitation following cutoffs or atypical migration patterns. Finally, analysis of individual Landsat images (not composites) combined with the in-channel sediment that was resolved through the classification and compositing procedures described in Chapter 4 may shed light on the bank-pull/bar-push mechanisms of meander migration [223, 64].

5. Meandering rivers are notoriously difficult to create in experimental settings, but the Landsat archive is a treasure trove of "natural experiments" of meandering river planform adjustments. This research focused only on one of the many major, active rivers in South America, but over a dozen other major tributaries to the Amazon River like the Ucayali offer enormous potential for a deeper understanding of the processes and controls on meander migration. The Mamoré River in Bolivia, for example, is a highly-active meandering river that has seen large sediment loads in its upstream reaches due to gold mining in the Amazon Rainforest. The floodplains of many large South American rivers are undergoing extensive settlement, agriculture, and/or deforestation. Such prolonged anthropogenic perturbations offer further opportunities to understand how rivers dynamically self-adjust. The tributaries to many major rivers are also highly mobile meandering rivers, expanding the varieties of environments and controls.

6. The pixel classification and composting processes employed to generate annual images of the Ucayali River were simple, but initial efforts at more sophisticated classifiers and compositing indicated that reliability of the final composite images could be significantly improved. Land cover in the Amazon Basin is comparatively homogeneous and thus offers the potential for the development of robust unsupervised classifiers. Improved classification in turn permits fully automated and more robust composite image creation, and further research to determine optimal compositing procedures is critical for expanding the work presented in Chapters 4 and 5 to other rivers and regions.

7. Cutoffs were empirically shown in Chapter 5 to accelerate morphodynamics up- and downstream of their occurrence, but the physical mechanisms through which the change manifests (i.e. theory) remain unknown. Cutoff abundance along the Ucayali River suggests that they play a major role in planform development, and long-time models of floodplain and valley evolution may miss key dynamics without appropriately accounting for cutoff effects. Cutoff theory should be developed, informed by the results in Chapter 5, some successful laboratory experiments [224], and monitoring of reaches before and after cutoff using advanced remote sensing techniques that resolve bathymetry ([225]) and sediment flux ([226]).

References

[1] Clive Granger, John William, and Allan Paul Andersen. *An introduction to bilinear time series models*. 1978, Vandenhoeck & Ruprecht.

[2] Syunsuke Ikeda, Gary Parker, and Kenji Sawai. Bend theory of river meanders. Part 1. Linear development. *Journal of Fluid Mechanics*, 1981, 112:363–377.

[3] Giovanni Seminara. Meanders. *Journal of Fluid Mechanics*, 2006, 554:271–297.

[4] Jasim Imran, Gary Parker, and Carlos Pirmez. A nonlinear model of flow in meandering submarine and subaerial channels. *Journal of Fluid Mechanics*, 1999, 400:295–331.

[5] Eli D. Lazarus and José Antonio Constantine. Generic theory for channel sinuosity. *Proceedings of the National Academy of Sciences of the United States of America*, 2013, 110(21):8447–52.

[6] JG Weihaupt. Possible origin and probable discharges of meandering channels on the planet Mars. *Journal of Geophysical Research*, 1974, 79(14).

[7] Rossman P. Irwin, Robert A. Craddock, and Alan D. Howard. Interior channels in Martian valley networks: Discharge and runoff production. *Geology*, 2005, 33(6):489.

[8] Ralph D. Lorenz, Rosaly M. Lopes, Flora Paganelli, Jonathan I. Lunine, Randolph L. Kirk, Karl L. Mitchell, Lawrence A. Soderblom, Ellen R. Stofan, Gian Ori, Melissa Myers, Hideyaki Miyamoto, Jani Radebaugh, Bryan Stiles, Stephen D. Wall, and C.A. Wood. Fluvial channels on Titan: Initial Cassini RADAR observations. *Planetary and Space Science*, 2008, 56(8):1132–1144.

[9] GG Ori, F Cannarsa, F Salese, I Dell'Arciprete, and G Komatsu. Why Braided Streams are Apparently Absent but There are Meander and Low-Sinuosity Single-Channels River Systems on Mars. In *44th Lunar and Planetary Science Conference*, 2013, pages 3–4.

[10] GM Kondolf. River restoration and meanders. *Ecology and Society*, 2006, 11(2).

[11] Peter Lagasse, L W Zevenbergen, W J Spitz, and Colin R. Thorne. *Methodology for Predicting Channel Migration.* Transportation Research Board, National Research Council, 2004, Fort Collins, CO.

[12] Nicholas E. Graf. *50 years of channel change on a reach of the Big Blue River, northeast Kansas.* PhD thesis, 2008, University of Wyoming.

[13] Wietse I. van de Lageweg, Wout M. van Dijk, and Maarten G. Kleinhans. Channel belt architecture formed by a meandering river. *Sedimentology*, 2013, 60(3):840–859.

[14] Adolfo Henriquez, Kelly Tyler, and Andrew Hurst. Characterization of Fluvial Sedimentology for Reservoir Simulation Modeling. *SPE Formation Evaluation*, 1990, 5(3).

[15] Donald Swanson. The Importance of Fluvial Processes and Related Reservoir Deposits. *Journal of Petroleum Technology*, 1993, 45(4):368–377.

[16] Richard Rhoda and Tony Burton. *Geo-Mexico: the geography and dynamics of modern Mexico.* 2010, Sombrero Books.

[17] Robert L. Beschta and William J. Ripple. The role of large predators in maintaining riparian plant communities and river morphology. *Geomorphology*, 2012, 157:88–98.

[18] Janet M. Hooke. *An analysis of changes in river channel patterns.* PhD thesis, 1977, University of Exeter.

[19] Luna Bergere Leopold and M. Gordon Wolman. River meanders. *Geological Society of America Bulletin*, 1960, 71(3):769–794.

[20] Janet M. Hooke. An analysis of the processes of river bank erosion. *Journal of Hydrology*, 1979, 42:39–62.

[21] H. N. Fisk, P. R. Mabrey, Jr. W. B. Steinriede, A. Osanik, and W. J. Turnbull. Geological Investigation of Mississippi River Acitivity: Memphis, Tennessee, to Mouth of Arkansas River. Technical report, U.S. Army Corps of Engineers, 1949, Vickburg, MS.

[22] Janet M. Hooke. River meander behaviour and instability: a framework for analysis. *Transactions of the Institute of British Geographers*, 2003, pages 238–253.

[23] Janet M. Hooke and L. Yorke. Rates, distributions and mechanisms of change in meander morphology over decadal timescales, River Dane, UK. *Earth Surface Processes and Landforms*, 2010, 35(13):1601–1614.

[24] M Jefferson. Limiting width of meander belts. 1902, *National Geographic*.

[25] GH Dury. Bed-width and Wave-length in Meandering Valleys. *Nature*, 1955, 176(31-32).

[26] Luna Bergere Leopold and M. Gordon Wolman. River channel patterns: braided, meandering, and straight. Technical report, United States Geological Survey, 1957, Washington, D.C.

[27] MS Quraishy. The origin of curves in rivers. *Current Science*, 1944, 13:36–39.

[28] JF Friedkin. A laboratory study of the meandering of alluvial rivers. Technical Report May 1945, U.S. Army Corps Engineers Waterways Expt. Sta., 1945, Vickburg, MS.

[29] Janet M. Hooke and CE Redmond. Use of Cartographic Sources for Analysing River Channel Change with Examples from Britain. In G.E. Petts, H. Moller, and A.L. Roux, editors, *Historical Change in Large Alluvial Rivers*, chapter 5, pages 79–93. J. Wiley, 1989, Chichester, UK.

[30] Zhengyi Yao, Jianhua Xiao, Wanquan Ta, and Xiaopeng Jia. Planform channel dynamics along the Ningxia-Inner Mongolia reaches of the Yellow River from 1958 to 2008: analysis using Landsat images and topographic maps. *Environmental Earth Sciences*, 2012, 70(1):97–106.

[31] T. Nagata, Y. Watanabe, H. Yasuda, and A. Ito. Development of a meandering channel caused by the planform shape of the river bank. *Earth Surface Dynamics*, 2014, 2(1):255–270.

[32] Carl J. Legleiter. Downstream effects of recent reservoir development on the morphodynamics of a meandering channel: Savery Creek, Wyoming, USA. 2014, *River Research and Applications*.

[33] Dong Xu, Yuchuan Bai, Jianmin Ma, and Yan Tan. Numerical investigation of long-term planform dynamics and stability of river meandering on fluvial floodplains. *Geomorphology*, 2011, 132(3-4):195–207.

[34] Nathan D Jackson and Christopher C Austin. Testing the Role of Meander Cutoff in Promoting Gene Flow across a Riverine Barrier in Ground Skinks (Scincella lateralis). *PloS one*, 2013, 8(5):e62812.

[35] Alessandra Crosato. Physical explanations of variations in river meander migration rates from model comparison. *Earth Surface Processes and Landforms*, 2009, 34(15):2078–2086.

[36] Alessandro Frascati and Stefano Lanzoni. Morphodynamic regime and long-term evolution of meandering rivers. *Journal of Geophysical Research*, 2009, 114(F2).

[37] Carlo Camporeale, P Perona, A Porporato, and L Ridolfi. On the long-term behavior of meandering rivers. *Water Resources Research*, 2005, 41(12).

[38] Alan D. Howard and Allen T. Hemberger. Multivariate characterization of meandering. *Geomorphology*, 1991, 4(3-4):161–186.

[39] F. D. Shields, Jr., Scott S. Knight, and John M. Stofleth. Alternatives for Riverine Backwater Restoration by Manipulation of Severed Meander Bend. *Impacts of Global Climate Change*, 2005, pages 1–12.

[40] Ryan P Rossell and Francis C K Ting. Hydraulic and Contraction Scour Analysis of a Meandering Channel: James River Bridges near Mitchell, South Dakota. *Journal of Hydraulic Engineering*, 2013, 139(Dec):1286–1296.

[41] Guido Zolezzi and Giovanni Seminara. Downstream and upstream influence in river meandering. Part 1. General theory and application to overdeepening. *Journal of Fluid Mechanics*, 2001, 438:183–211.

[42] John Leighly. Meandering Arroyos of the Dry Southwest. *Geographical Review*, 1936, 62:338–344.

[43] F. A. Melton. An Empirical Classification of Flood-Plain Streams. *Geographical Review*, 1936, 26(4):593.

[44] SA Schumm. Patterns of alluvial rivers. *Annual Review of Earth and Planetary Sciences*, 1985, 13:5–27.

[45] Janet M. Hooke. Changes in river meanders: a review of techniques and results of analyses. *Progress in Physical Geography*, 1984, 8(4):473–508.

[46] Peter Lagasse, William Spitz, and Lyle Zevenbergen. A Methodology and ArcView Tools for Predicting Channel Migration. In *ESRI, User Conference Proceedings*, 2003, San Diego, CA.

[47] Victor R. Baker, R. Craig Kochel, and Peter C Patton. *Flood geomorphology*. John Wiley, 1987, New York.

[48] Robert I. Ferguson. Meander irregularity and wavelength estimation. *Journal of Hydrology*, 1975, 26(3-4):315–333.

[49] Inci Güneralp, Jorge D. Abad, Guido Zolezzi, and Janet M. Hooke. Advances and challenges in meandering channels research. *Geomorphology*, 2012, 163:1–9.

[50] Giovanni Seminara and Michele Bolla Pittaluga. Reductionist versus holistic approaches to the study of river meandering: An ideal dialogue. *Geomorphology*, 2012, 163-164:110–117.

[51] Keith Montgomery. Non-linear dynamics and river meandering. *Area*, 1993, 25(2):97–108.

[52] Eliana Perucca, Carlo Camporeale, and Luca Ridolfi. Nonlinear analysis of the geometry of meandering rivers. *Geophysical Research Letters*, 2005, 32(3):5–8.

[53] Alessandro Frascati and Stefano Lanzoni. Long-term river meandering as a part of chaotic dynamics? A contribution from mathematical modelling. *Earth Surface Processes and Landforms*, 2010, 35:791–802.

[54] Hans-Henrik Stolum. Planform geometry and dynamics of meandering rivers. *Geological Society of America Bulletin*, 1998, 110(11):1485–1498.

[55] Hans-Henrik Stolum. River Meandering as a Self-Organization Process. *Science*, 1996, 271(5256):1710–1713.

[56] R. Scott Snow. Fractal sinuosity of stream channels. *Pure and Applied Geophysics*, 1989, 131(1-2):99–109.

[57] Keith Montgomery. Sinuosity and fractal dimension of meandering rivers. *Area*, 1996, 28(4):491–500.

[58] Carlo Camporeale, Eliana Perucca, and L Ridolfi. Significance of cutoff in meandering river dynamics. *Journal of Geophysical Research*, 2008, 113(F1):1–11.

[59] Kazuyoshi Hasegawa. Computer simulation of the gradual migration of meandering channels. In *Proceedings of the Hokkaido Branch, Japan Society of Civil Engineering*, 1977, pages 197–202.

[60] Gary Parker, Y. Shimizu, G. V. Wilkerson, Esther C Eke, Jorge D. Abad, J. W. Lauer, Chris Paola, William E. Dietrich, and V. R. Voller. A new framework for modeling the migration of meandering rivers. *Earth Surface Processes and Landforms*, 2011, 36(1):70–86.

[61] Davide Motta, Jorge D. Abad, E. J. Langendoen, and Marcelo H. Garcia. The effects of floodplain soil heterogeneity on meander planform shape. *Water Resources Research*, 2012, 48(9).

[62] M. Bolla Pittaluga, G. Nobile, and Giovanni Seminara. A nonlinear model for river meandering. *Water Resources Research*, 2009, 45(4).

[63] Alessandro Frascati and Stefano Lanzoni. A mathematical model for meandering rivers with varying width. *Journal of Geophysical Research: Earth Surface*, 2013, 118(3):1641–1657.

[64] Esther C Eke, Gary Parker, and Yasuyuki Shimizu. Numerical modeling of erosional and depositional bank processes in migrating river bends with self-formed width: morphodynamics of bar push and bank pull. *Journal of Geophysical Research: Earth Surface*, 2014, 119(7):1455–1483.

[65] AJ Odgaard. Streambank erosion along two rivers in Iowa. *Water Resources Research*, 1987, 23(7):1225–1236.

[66] J. E. Pizzuto and T. S. Meckelnburg. Evaluation of a linear bank erosion equation. *Water Resources Research*, 1989, 25(5):1005–1013.

[67] Jennifer Rose Wallick, Stephen T. Lancaster, and John P. Bolte. Determination of bank erodibility for natural and anthropogenic bank materials using a model of lateral migration and observed erosion along the Willamette River, Oregon, USA. *River Research and Applications*, 2006, 22(6):631–649.

[68] Candice R. Constantine, Thomas Dunne, and Gregory J. Hanson. Examining the physical meaning of the bank erosion coefficient used in meander migration modeling. *Geomorphology*, 2009, 106(3):242–252.

[69] Erik Mosselman. Morphological modelling of rivers with erodible banks. *Hydrological Processes*, 1998, 12.8:1357–1370.

[70] Eric W Larsen and Emily Anderson. The controls on and evolution of channel morphology of the Sacramento River: A case study of River Miles 201-185. Technical report, University of California, 2002, Davis, CA.

[71] E. R. Micheli and J. W. Kirchner. Effects of wet meadow riparian vegetation on streambank erosion. 1. Remote sensing measurements of streambank migration and erodibility. *Earth Surface Processes and Landforms*, 2002, 27(6):627–639.

[72] Tao Sun, Paul Meakin, Torstein Jøssang, and Klaus Schwarz. A Simulation Model for Meandering Rivers. *Water Resources Research*, 1996, 32(9):2937–2954.

[73] Inci Güneralp and Bruce L. Rhoads. Influence of floodplain erosional heterogeneity on planform complexity of meandering rivers. *Geophysical Research Letters*, 2011, 38(14).

[74] Eliana Perucca, Carlo Camporeale, and L. Ridolfi. Significance of the riparian vegetation dynamics on meandering river morphodynamics. *Water Resources Research*, 2007, 43(3).

[75] Helgi Johannesson and Gary Parker. Computer simulated migration of meandering rivers in Minnesota. Technical report, University of Minnesota, 1985, Minneapolis, Minnesota.

[76] Gary Parker and Edmund D. Andrews. On the time development of meander bends. *Journal of Fluid Mechanics*, 1986, 162:139–156.

[77] N Struiksma, K. W. Olesen, C Flokstra, and H. J. De Vriend. Bed deformation in curved alluvial channels. *Journal of Hydraulic Research*, 1985, 23(1):57–79.

[78] P. Blondeaux and Giovanni Seminara. A unified bar-bend theory of river meanders. *Journal of Fluid Mechanics*, 1985, 157:449–470.

[79] Stefano Lanzoni and Giovanni Seminara. On the nature of meander instability. *Journal of Geophysical Research*, 2006, 111(F4).

[80] Helgi Johannesson and Gary Parker. Velocity Redistribution in Meandering Rivers. *Journal of Hydraulic Engineering*, 1989, 115(8):1019–1039.

[81] Koen Blanckaert and H. J. de Vriend. Meander dynamics: A nonlinear model without curvature restrictions for flow in open-channel bends. *Journal of Geophysical Research*, 2010, 115(F4).

[82] Rossella Luchi, Guido Zolezzi, and Marco Tubino. Bend theory of river meanders with spatial width variations. *Journal of Fluid Mechanics*, 2011, 681:311–339.

[83] Philip Hall. Alternating bar instabilities in unsteady channel flows over erodible beds. *Journal of Fluid Mechanics*, 2004, 499:49–73.

[84] Kazutake Asahi, Yasuyuki Shimizu, Jonathan M. Nelson, and Gary Parker. Numerical simulation of river meandering with self-evolving banks. *Journal of Geophysical Research: Earth Surface*, 2013, 118(4):2208–2229.

[85] N. Rüther and N.R.B. Olsen. Modelling free-forming meander evolution in a laboratory channel using three-dimensional computational fluid dynamics. *Geomorphology*, 2007, 89(3-4):308–319.

[86] Tom J. Coulthard and Marco J. Van De Wiel. A cellular model of river meandering. *Earth Surface Processes and Landforms*, 2006, 31(1):123–132.

[87] Carlo Camporeale, P Perona, A Porporato, and L Ridolfi. Hierarchy of models for meandering rivers and related morphodynamic processes. *Reviews of Geophysics*, 2007, 45(1):RG1001.

[88] Alessandra Crosato. Effects of smoothing and regridding in numerical meander migration models. *Water Resources Research*, 2007, 43(1).

[89] CS Duris. Discrete interpolating and smoothing spline functions. *SIAM Journal on Numerical Analysis*, 1977, 14(4):686–698.

[90] Carl de Boor. *A Practical Guide to Splines*. Springer Verlag, 2001, New York.

[91] Alessandra Crosato. Simulation of meandering river processes. *Commun. Hydraul. Geotech. Eng.*, 1990, 90-3.

[92] M Worring and AWM Smeulders. Digital curvature estimation. *CVGIP: Image Understanding*, 1993, 58(3):366–382.

[93] JRL Allen. A review of the origin and characteristics of recent alluvial sediments. 1965, *Sedimentology*.

[94] G. Lewis and John Lewin. Alluvial cutoffs in Wales and the borderlands. *Spec. Publs int. Ass. Sediment*, 1983, 6:145–154.

[95] Glenn R. Gay, Hubert H. Gay, William H. Gay, Holly A. Martinson, Robert H. Meade, and John A. Moody. Evolution of cutoffs across meander necks in Powder River, Montana, USA. *Earth Surface Processes and Landforms*, 1998, 23(7):651–662.

[96] José Antonio Constantine, Stephen R McLean, and T Dunne. A mechanism of chute cutoff along large meandering rivers with uniform floodplain topography. *Geological Society of America Bulletin*, 2009, 122(5-6):855–869.

[97] Alan D. Howard. Modelling Channel Evolution and Floodplain Morphology. In *Floodplain Processes*, chapter 2, pages 15–62. Wiley, 1996, Chichester.

[98] S J Orfanidis. *Introduction to Signal Processing*. Prentice-Hall, 1996, Englewood Cliffs, NJ.

[99] Sven Utcke. Error-bounds on curvature estimation. In *Scale Space Methods in Computer Vision*, pages 657–666. Springer Berlin Heidelberg, 2003, Berlin.

[100] Inci Güneralp and Bruce L. Rhoads. Continuous Characterization of the Planform Geometry and Curvature of Meandering Rivers. *Geographical Analysis*, 2007, 40(1):1–25.

[101] M. A. Carson and M. F. Lapointe. The inherent asymmetry of river meander planform. *The Journal of Geology*, 1983, 91:41–55.

[102] Inci Güneralp and Bruce L. Rhoads. Spatial autoregressive structure of meander evolution revisited. *Geomorphology*, 2010, 120(3-4):91–106.

[103] Carl J. Legleiter and Phaedon C. Kyriakidis. Forward and Inverse Transformations between Cartesian and Channel-fitted Coordinate Systems for Meandering Rivers. *Mathematical Geology*, 2007, 38(8):927–958.

[104] Jennifer G. Duan and Pierre Y. Julien. Numerical simulation of meandering evolution. *Journal of Hydrology*, 2010, 391(1-2):34–46.

[105] Ari J. Posner. River meander modeling and confronting uncertainty. Technical Report SAND2011-3521, Sandia National Laboratories, 2011, Albuquerque, NM.

[106] Davide Motta, Jorge D. Abad, Eddy J. Langendoen, and Marcelo H. Garcia. A simplified 2D model for meander migration with physically-based bank evolution. *Geomorphology*, 2012, 163-164:10–25.

[107] Tao Sun, Paul Meakin, and Torstein Jøssang. A computer model for meandering rivers with multiple bed load sediment sizes: 1. Theory. *Water Resources Research*, 2001, 37(8):2227–2241.

[108] J.C. Brice and James C. Brice. Evolution of meander loops. *Geological Society of America Bulletin*, 1974, 85(4):581–586.

[109] R Kinoshita. An investigation of channel deformation of the Ishikari River. Technical report, Natural Resources Division, Ministry of Science and Technology of Japan, 1961, Tokyo.

[110] James F. Daniel. Channel movement of meandering Indiana streams. 1971, pages USGS Professional Paper 732–A.

[111] Gerald C. Nanson and Edward J. Hickin. Channel migration and incision on the Beatton River. *Journal of Hydraulic Engineering*, 1983, 109(3):327–337.

[112] Giovanni Seminara, Guido Zolezzi, M. Tubino, D. Zardi, Via Montallegro, Ingegneria Ambientale, Via Mesiano, and Ingegneria Civile. Downstream and upstream influence in river meandering. Part 2. Planimetric development. *Journal of Fluid Mechanics*, 2001, 438:213–230.

[113] Walter Basil Langbein and Luna Bergere Leopold. River meanders–Theory of minimum variance. 1966, Technical report.

[114] Edward J. Hickin. The development of meanders in natural river-channels. *American Journal of Science*, 1974, 274(4):414–442.

[115] Edward J. Hickin and Gerald C. Nanson. The Character of Channel Migration on the Beatton River, Northeast British Columbia, Canada. *Geological Society of America Bulletin*, 1975, 86(4):487.

[116] Janet M. Hooke. Changes in meander morphology. In V. Gardiner, editor, *International Geomorphology, 1986: Proceedings of the First International Conference on Geomorphology*, pages 591–609. John Wiley & Sons, 1987, Chichester, UK.

[117] Janet M. Hooke. Complexity, self-organisation and variation in behaviour in meandering rivers. *Geomorphology*, 2007, 91(3-4):236–258.

[118] David Jon Furbish. River-bend curvature and migration: How are they related? *Geology*, 1988, 16(8):752.

[119] Michele Bolla Pittaluga and Giovanni Seminara. Nonlinearity and unsteadiness in river meandering: A review of progress in theory and modelling. *Earth Surface Processes and Landforms*, 2011, 36(1):20–38.

[120] Douglas J. Jerolmack and Chris Paola. Shredding of environmental signals by sediment transport. *Geophysical Research Letters*, 2010, 37(19):1–5.

[121] Gary Parker, Kenji Sawai, and Syunsuke Ikeda. Bend theory of river meanders. Part 2. Nonlinear deformation of finite-amplitude bends. *Journal of Fluid Mechanics*, 1982, 115:303–314.

[122] R. A. Callander. Instability and river channels. *Journal of Fluid Mechanics*, 1969, 36(03):465–480.

[123] J. Dungan Smith and Stephen R McLean. A Model for Flow in Meandering Streams. 1984, 20(9):1301–1315.

[124] Seokkoo Kang and Fotis Sotiropoulos. Assessing the predictive capabilities of isotropic, eddy viscosity Reynolds-averaged turbulence models in a natural-like meandering channel. *Water Resources Research*, 2012, 48(6):1–12.

[125] Per Bak, Chao Tang, and Kurt Wiesenfeld. Self-organized criticality: An explanation of the 1/f noise. *Physical Review Letters*, 1987, 59(4):381–384.

[126] Hans-Henrik Stolum. Fluctuations at the self-organized critical state. *Physical Review E*, 1997, 56(6):6710–6718.

[127] James Theiler, S Eubank, A Longtin, and B Galdrikian. Testing for nonlinearity in time series: the method of surrogate data. *Physica D: Nonlinear*, 1992, 58:77–94.

[128] Thomas Schreiber and Andreas Schmitz. Surrogate time series. *Physica D: Nonlinear Phenomena*, 2000, 142(3-4):346–382.

[129] Martin Bevis. *Sediment budgets indicate Pleistocene base level fall drives erosion in Minnesota's greater Blue Earth River basin.* PhD thesis, 2015, University of Minnesota, Duluth.

[130] Jon Schwenk, Ankush Khandelwal, Mulu Fratkin, Vipin Kumar, and Efi Foufoula-Georgiou. RivMAP: A toolbox for resolving river planform dynamics and application to Landsat imagery of the Ucayali River. *Earth and Space Science*, 2016, In Review.

[131] Ronald R. Gutierrez and Jorge D. Abad. On the analysis of the medium term planform dynamics of meandering rivers. *Water Resources Research*, 2014, 50(5):3714–3733.

[132] Holger Kantz and Thomas Schreiber. *Nonlinear time series analysis.* 2004, Cambridge University Press.

[133] Thomas Schreiber and Andreas Schmitz. Improved surrogate data for nonlinearity tests. *Physical Review Letters*, 1996, 635:1–4, 9909041v1.

[134] Christopher J Keylock. A wavelet-based method for surrogate data generation. *Physica D: Nonlinear Phenomena*, 2007, 225(2):219–228.

[135] Christopher J Keylock. Improved preservation of autocorrelative structure in surrogate data using an initial wavelet step. *Nonlinear Processes in Geophysics*, 2008, pages 435–444.

[136] V. Venema, F. Ament, and C. Simmer. A Stochastic Iterative Amplitude Adjusted Fourier Transform algorithm with improved accuracy. *Nonlinear Processes in Geophysics*, 2006, 13(3):321–328.

[137] Floris Takens. Detecting strange attractors in turbulence. In *Dynamical Systems and Turbulence, Warwick 1980*, volume 898, pages 366–381. 1981, Springer Berlin Heidelberg.

[138] Matthew B. Kennel, Reggie Brown, and Henry D. I. Abarbanel. Determining embedding dimension for phase-space reconstruction using a geometrical construction. *Physical Review A*, 1992, 45(6):3403–3411.

[139] Richard Moeckel and Brad Murray. Measuring the distance between time series. *Physica D: Nonlinear Phenomena*, 1997, 102:187–194.

[140] S. Basu and Efi Foufoula-Georgiou. Detection of nonlinearity and chaoticity in time series using the transportation distance function. *Physics Letters A*, 2002, 301(5-6):413–423.

[141] Yossi Rubner, Carlo Tomasi, and Leonidas J. Guibas. The Earth Mover's Distance as a Metric for Image Retrieval. *International Journal of Computer Vision*, 2000, 40(2):99–121.

[142] Leonid V. Kantorovich. On the transfer of masses. *Dokl. Akad. Nauk. SSSR*, 1942, 37(7-8).

[143] Lipeng Ning, Tryphon T Georgiou, and Allen Tannenbaum. On Matrix-Valued Monge-Kantorovich Optimal Mass Transport. *IEEE Transactions on Automatic Control*, 2015, 60(2):373–382.

[144] Christopher J Keylock, Arvind Singh, and Efi Foufoula-Georgiou. The complexity of gravel bed river topography examined with gradual wavelet reconstruction. *Journal of Geophysical Research: Earth Surface*, 2014, 119(3):682–700.

[145] Efi Foufoula-Georgiou, Zeinab Takbiri, Jonathan A. Czuba, and Jon Schwenk. The change of nature and the nature of change in agricultural landscapes: Hydrologic regime shifts modulate ecological transitions. *Water Resources Research*, 2015, 51(8):6649–6671, 2014WR016527.

[146] Jon Schwenk, Stefano Lanzoni, and Efi Foufoula-Georgiou. The life of a meander bend: Connecting shape and dynamics via analysis of a numerical model. *Journal of Geophysical Research: Earth Surface*, 2015, 120(4):690–710.

[147] Jon Schwenk and Efi Foufoula-Georgiou. Accelerated migration rates downstream of a human-induced cutoff in the Ucayali River, Peru. In *River, Coastal and Estuarine Morphodynamics*, 2015, Iquitos, Peru.

[148] Christopher J Keylock. Characterizing the structure of nonlinear systems using gradual wavelet reconstruction. *Nonlinear Processes in Geophysics*, 2010, 17(6):615–632.

[149] Donald B. Percival and Andrew T. Walden. *Wavelet methods for time series analysis*. 2006, Cambridge University Press.

[150] Stuart N. Lane and KS Richards. Linking river channel form and process: time, space and causality revisited. *Earth Surface Processes and Landforms*, 1997, 22:249–260.

[151] Inci Güneralp and R. A. Marston. Process-form linkages in meander morphodynamics: Bridging theoretical modeling and real world complexity. *Progress in Physical Geography*, 2012, 36(6):718–746.

[152] Carl J. Legleiter. A geostatistical framework for quantifying the reach-scale spatial structure of river morphology: 1. Variogram models, related metrics, and relation to channel form. *Geomorphology*, 2014, 205:65–84.

[153] Robert Andrle. The angle measure technique: A new method for characterizing the complexity of geomorphic lines. *Mathematical Geology*, 1994, 26(1):83–97.

[154] Robert Andrle. Measuring channel planform of meandering rivers. *Physical Geography*, 1996, 17:270–281.

[155] Stephen T. Lancaster and Rafael L. Bras. A simple model of river meandering and its comparison to natural channels. *Hydrological Processes*, 2002, 16(1):1–26.

[156] B. Vermeulen, A.J.F. Hoitink, Guido Zolezzi, Jorge D. Abad, and Rolf Aalto. Multiscale structure of meanders. 2016, *Geophysical Research Letters*.

[157] Guido Zolezzi and Inci Güneralp. Continuous wavelet characterization of the wavelengths and regularity of meandering rivers. *Geomorphology*, 2016, 252:98–111.

[158] Tao Sun, Paul Meakin, and Torstein Jøssang. A computer model for meandering rivers with multiple bed load sediment sizes: 2. Computer simulations. *Water Resources Research*, 2001, 37(8):2243–2258.

[159] G. Erkens, T. Hoffmann, R. Gerlach, and J. Klostermann. Complex fluvial response to Lateglacial and Holocene allogenic forcing in the Lower Rhine Valley (Germany). *Quaternary Science Reviews*, 2011, 30(5-6):611–627.

[160] Oliver P. Harmar and Nicholas J. Clifford. Planform dynamics of the Lower Mississippi River. *Earth Surface Processes and Landforms*, 2006, 31(7):825–843.

[161] Cheryl Bradley and Derald G. Smith. Meandering channel response to altered flow regime: Milk River, Alberta and Montana. *Water Resources Research*, 1984, 20(12):1913–1920.

[162] Tímea Kiss and Viktória Blanka. River channel response to climate- and human-induced hydrological changes: Case study on the meandering Hernád River, Hungary. *Geomorphology*, 2012, 175-176:115–125.

[163] Edward J. Hickin and Henry M. Sichingabula. The geomorphic impact of the catastrophic October 1984 flood on the planform of Squamish River, southwestern British Columbia. *Canadian Journal of Earth Sciences*, 1989, 26(2):337–337.

[164] Janet M. Hooke. Cutoffs galore!: occurrence and causes of multiple cutoffs on a meandering river. *Geomorphology*, 2004, 61:225–238.

[165] Jessica A. Zinger, Bruce L. Rhoads, and James L. Best. Extreme sediment pulses generated by bend cutoffs along a large meandering river. *Nature Geoscience*, 2011, 4(10):675–678.

[166] Tapas R. Martha, Anita Sharma, and K. Vinod Kumar. Development of meander cutoffs-a multi-temporal satellite-based observation in parts of Sindh River, Madhya Pradesh, India. 2014, *Arabian Journal of Geosciences*.

[167] G. P. Asner, W. Llactayo, R. Tupayachi, and E. R. Luna. Elevated rates of gold mining in the Amazon revealed through high-resolution monitoring. *Proceedings of the National Academy of Sciences*, 2013, 110(46):18454–18459.

[168] Neha Midha and Pradeep K Mathur. Channel characteristics and planform dynamics in the Indian Terai, Sharda River. *Environmental management*, 2014, 53(1):120–34.

[169] Marcin Słowik. Is history of rivers important in restoration projects? The example of human impact on a lowland river valley (the Obra River, Poland). *Geomorphology*, 2015, 251:50–63.

[170] W. Bertoldi, L. Zanoni, and M. Tubino. Assessment of morphological changes induced by flow and flood pulses in a gravel bed braided river: The Tagliamento River (Italy). *Geomorphology*, 2010, 114(3):348–360.

[171] H. Rodnight, G.a.T. Duller, S. Tooth, and A.G. Wintle. Optical dating of a scroll-bar sequence on the Klip River, South Africa, to derive the lateral migration rate of a meander bend. *The Holocene*, 2005, 15(6):802–811.

[172] RL Handy. Alluvial cutoff dating from subsequent growth of a meander. *Geological Society of America Bulletin*, 1972, 83(2):475–480.

[173] Eliana Perucca, Carlo Camporeale, and L. Ridolfi. Influence of river meandering dynamics on riparian vegetation pattern formation. *Journal of Geophysical Research*, 2006, 111(G1):1–9.

[174] Xiaojun Yang, Michiel C.J Damen, and Robert a van Zuidam. Satellite remote sensing and GIS for the analysis of channel migration changes in the active Yellow River Delta, China. *International Journal of Applied Earth Observation and Geoinformation*, 1999, 1(2):146–157.

[175] Abul Basar M Baki and Thian Yew Gan. Riverbank migration and island dynamics of the braided Jamuna River of the Ganges-Brahmaputra basin using multi-temporal Landsat images. *Quaternary International*, 2012, 263:148–161.

[176] Niladri Gupta, Peter M Atkinson, and Paul A Carling. Decadal length changes in the fluvial planform of the River Ganga: bringing a mega-river to life with Landsat archives. *Remote Sensing Letters*, 2013, 4(1):1–9.

[177] R Kalliola, J Salo, M Puhakka, and M Rajasilta. Upper Amazon channel migration. *Naturwissenschaften*, 1992, 79:75–79.

[178] José Antonio Constantine, Thomas Dunne, Joshua Ahmed, Carl J. Legleiter, and Eli D. Lazarus. Sediment supply as a driver of river meandering and floodplain evolution in the Amazon Basin. *Nature Geoscience*, 2014, 7(12):899–903.

[179] Arved C. Schwendel, Andrew P. Nicholas, Rolf Aalto, Greg H. Sambrook Smith, and Simon Buckley. Interaction between meander dynamics and floodplain heterogeneity

in a large tropical sand-bed river: the Rio Beni, Bolivian Amazon. *Earth Surface Processes and Landforms*, 2015, 40(15):2026–2040.

[180] C. E. Frias, Jorge D. Abad, A. Mendoza, J. Paredes, C. Ortals, and H. Montoro. Planform evolution of two anabranching structures in the Upper Peruvian Amazon River. *Water Resources Research*, 2015, 51(4):2742–2759, 2014WR016527.

[181] E. Gautier, D Brunstein, P Vauchel, M Roulet, O Fuertes, JL Guyot, J Darozzes, and L Bourrel. Temporal relations between meander deformation, water discharge and sediment fluxes in the floodplain of the Rio Beni (Bolivian Amazonia). *Earth Surface Processes and Landforms*, 2007, 248(July):230–248.

[182] Tamlin M. Pavelsky and Laurence C. Smith. RivWidth: A software tool for the calculation of river widths from remotely sensed imagery. *IEEE Geoscience and Remote Sensing Letters*, 2008, 5(1):70–73.

[183] G. Burch Fisher, Bodo Bookhagen, and Colin B. Amos. Channel planform geometry and slopes from freely available high-spatial resolution imagery and DEM fusion: Implications for channel width scalings, erosion proxies, and fluvial signatures in tectonically active landscapes. *Geomorphology*, 2013, 194:46–56.

[184] Kristin R. Dauer. *Dynamic and Static Characterization of the Planimetry of the Ucayali River, Peru.* PhD thesis, 2015, University of Pittsburgh.

[185] Jorge D. Abad and Marcelo H. Garcia. RVR Meander: A toolbox for re-meandering of channelized streams. *Computers & Geosciences*, 2006, 32(1):92–101.

[186] J. Wesley Lauer. 2006, Channel Planform Statistics Tool (NCED Stream Restoration Toolbox).

[187] Bernd Ettmer and Cesar Adolfo Alvarado-Ancieta. Morphological development of the Ucayali River, Peru without human impacts. *Waldökologie, Landschaftsforschung und Naturschutz*, 2010, 10:77–84.

[188] Ronald J. Gibbs. The geochemistry of the Amazon River system: Part I. The factors that control the salinity and the composition and concentration of the suspended solids. *Bulletin of the Geological Society of America*, 1967, 78(10):1203–1232.

[189] Jhan Carlo Espinoza Villar, Jean Loup Guyot, Josyane Ronchail, Gérard Cochonneau, Naziano Filizola, Pascal Fraizy, David Labat, Eurides de Oliveira, Juan Julio Ordoñez, and Philippe Vauchel. Contrasting regional discharge evolutions in the Amazon basin (1974-2004). *Journal of Hydrology*, 2009, 375(3-4):297–311.

[190] Waldo Sven Lavado Casimiro, David Labat, Josyane Ronchail, Jhan Carlo Espinoza, and Jean Loup Guyot. Trends in rainfall and temperature in the Peruvian Amazon-Andes basin over the last 40 years (1965-2007). *Hydrological Processes*, 2012, 27(20):2944–2957.

[191] Christian Abizaid. An Anthropogenic Meander Cutoff Along the Ucayali River, Peruvian Amazon. *The Geographical Review*, 2005, 95(1):122–135.

[192] OT Coomes, Christian Abizaid, and M Lapointe. Human modification of a large meandering Amazonian river: genesis, ecological and economic consequences of the Masisea cutoff on the central Ucayali, Peru. *Ambio*, 2009, 38(3):130–134.

[193] K. Webster, J.P. Arroyo-Mora, O.T. Coomes, Y. Takasaki, and C. Abizaid. A cost path and network analysis methodology to calculate distances along a complex river network in the Peruvian Amazon. *Applied Geography*, 2016, 73:13–25.

[194] M Pal and P M Mather. Support vector machines for classification in remote sensing. *International Journal of Remote Sensing*, 2005, 26(5):1007–1011.

[195] Y Bazi and F Melgani. Toward an Optimal SVM Classification System for Hyperspectral Remote Sensing Images. *IEEE Transactions on Geoscience and Remote Sensing*, 2006, 44(11):3374–3385.

[196] Giles M. Foody and Ajay Mathur. The use of small training sets containing mixed pixels for accurate hard image classification: Training on mixed spectral responses for classification by a SVM. *Remote Sensing of Environment*, 2006, 103(2):179–189.

[197] Garnett P. Williams. Bank-full discharge of rivers. *Water Resources Research*, 1978, 14(6):1141–1154.

[198] M. Gordon Wolman and John P Miller. Magnitude and Frequency of Forces in Geomorphic Processes. *The Journal of Geology*, 1960, 68(1):54–74.

[199] Edmund D. Andrews. Effective and bankfull discharges of streams in the Yampa River basin, Colorado and Wyoming. *Journal of Hydrology*, 1980, 46(3-4):311–330.

[200] K.D. Woodyer. Bankfull frequency in rivers. *Journal of Hydrology*, 1968, 6(2):114–142.

[201] C Harrelson, C L Rawlins, and J Potyondy. Stream channel reference sites: an illustrated guide to field technique. *USDA Forest Service General Technical Report RM-245*, 1994, page 61.

[202] E. M. Latrubesse, J. C. Stevaux, and R. Sinha. Tropical rivers. *Geomorphology*, 2005, 70:187–206.

[203] Abraham. Savitzky and M. J. E. Golay. Smoothing and Differentiation of Data by Simplified Least Squares Procedures. *Analytical Chemistry*, 1964, 36(8):1627–1639.

[204] Edward J. Hickin and Gerald C. Nanson. Lateral migration rates of river bends. *Journal of Hydraulic Engineering*, 1984, 110:1557–1567.

[205] Luna B. Leopold and Thomas. Maddock. The Hydraulic Geomtry of Stream Channels and Some Physiographic Implications. *Geological Survey Professional Paper 252*, 1953, page 57.

[206] William Santini, J.-M. Martinez, R. Espinoza-Villar, Gerard Cochonneau, Philippe Vauchel, J.-S. Moquet, Patrice Baby, J.-C. Espinoza, Waldo Lavado, Jorge Carranza, and J.-L. Guyot. Sediment budget in the Ucayali River basin, an Andean tributary of the Amazon River. *Proceedings of the International Association of Hydrological Sciences*, 2015, 367(December):320–325.

[207] Chas. R. Dryer. The Meanders of the Muscatatuck at Vernon, Indiana. *Proceedings of the Indiana Academy of Science*, 1898, 8:270–273.

[208] E. W. Lane. The effect of cutting off bends in rivers. In *University of Iowa Studies in Engineering. Proceedings of the Third Hydraulics Conference*, pages 230–240, 1947, Iowa City, Iowa.

[209] Luna Bergere Leopold, M. Gordon Wolman, and John P. Miller. *Fluvial processes in geomorphology*. W. H. Freeman and Company, 1964, San Francisco.

[210] Paul F. Hudson and Richard H. Kesel. Channel migration and meander-bend curvature in the lower Mississippi River prior to major human modification. *Geology*, 2000, 28(6):531–534.

[211] E. R. Micheli and Eric W Larsen. River channel cutoff dynamics, Sacramento river, California, USA. *River Research and Applications*, 2011, 344(27):328–344.

[212] David S Biedenharn, Colin R Thorne, and Chester C Watson. Recent morphological evolution of the Lower Mississippi River. *Geomorphology*, 2000, 34:227–249.

[213] Laura Jugaru Tiron, Jérôme Le Coz, Mireille Provansal, Nicolae Panin, Guillaume Raccasi, Guillaume Dramais, and Philippe Dussouillez. Flow and sediment processes in a cutoff meander of the Danube Delta during episodic flooding. *Geomorphology*, 2009, 106:186–197.

[214] Ian C. Fuller, A. R G Large, and David J. Milan. Quantifying channel development and sediment transfer following chute cutoff in a wandering gravel-bed river. *Geomorphology*, 2003, 54:307–323.

[215] Jessica A. Zinger, Bruce L. Rhoads, James L. Best, and Kevin K. Johnson. Flow structure and channel morphodynamics of meander bend chute cutoffs: A case study of the Wabash River, USA. *Journal of Geophysical Research: Earth Surface*, 2013, 118(4):2468–2487.

[216] Janet M. Hooke. River channel adjustment to meander cutoffs on the River Bollin and River Dane, northwest England. *Geomorphology*, 1995, 14(3):235–253.

[217] M.C. Grenfell, Andrew P. Nicholas, and Rolf Aalto. Mediative adjustment of river dynamics: The role of chute channels in tropical sand-bed meandering rivers. *Sedimentary Geology*, 2014, 301:93–106.

[218] J. P. C. Eekhout and A. J. F. Hoitink. Chute cutoff as a morphological response to stream reconstruction: The possible role of backwater. *Water Resources Research*, 2015, 51(5):3339–3352, 2014WR016527.

[219] Marcin Słowik. The influence of meander bend evolution on the formation of multiple cutoffs: findings inferred from floodplain architecture and bend geometry. *Earth Surface Processes and Landforms*, 2016, 41(5):626–641.

[220] Brien R. Winkley. Man-Made cutoffs on the Lower Mississippi River, Conception, Construction, and River Response. *Potamology Investigations*, 1977, pages 1–219.

[221] Emory Wilson Lane. A Study of the shape of channels formed by natural streams flowing in erodible material. 1957, Technical report.

[222] Janet M. Hooke. River Meandering. *Treatise on Geomorphology*, 2013, 9:260–288.

[223] W. I. van de Lageweg, W. M. van Dijk, a. W. Baar, J. Rutten, and Maarten G. Kleinhans. Bank pull or bar push: What drives scroll-bar formation in meandering rivers? *Geology*, 2014, 42(4):319–322.

[224] Christian A. Braudrick, William E. Dietrich, Glen T. Leverich, and Leonard S. Sklar. Experimental evidence for the conditions necessary to sustain meandering in coarse-bedded rivers. *Proceedings of the National Academy of Sciences of the United States of America*, 2009, 106(40):16936–41.

[225] Carl J. Legleiter, Dar A. Roberts, and Rick L. Lawrence. Spectrally based remote sensing of river bathymetry. *Earth Surface Processes and Landforms*, 2009, 34(8):1039–1059.

[226] Leif G. Olmanson, Patrick L. Brezonik, and Marvin E. Bauer. Airborne hyperspectral remote sensing to assess spatial distribution of water quality characteristics in large rivers: The Mississippi River and its tributaries in Minnesota. *Remote Sensing of Environment*, 2013, 130:254–265.